University of Massachusetts Dartmouth

Department of Electrical and Computer Engineering

HIGHER ORDER HEXAHEDRAL FINITE ELEMENTS FOR

ELECTROMAGNETIC MODELING

A Dissertation in

Electrical Engineering

by

Milan M. Ilić

Submitted in Partial fulfillment of the
Requirements for the Degree of
Doctor of Philosophy

September, 2003

I grant the University of Massachusetts Dartmouth the non-exclusive right to use the work for the purpose of making single copies of the work available to the public on a not-for-profit basis if the University's circulating copy is lost or destroyed.
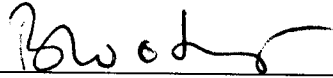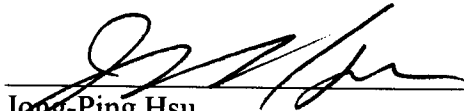

Milan Ilić

Date: 07/30/2003

We approve the thesis of Milan Ilić

Date of Signature

_____   7/7/03

Branislav M. Notaros
Assistant Professor of Electrical and Computer Engineering
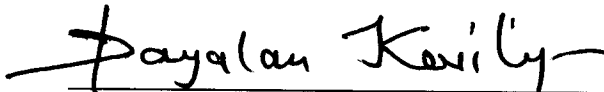Thesis Advisor

_____   7/7/03

Jong-Ping Hsu
Professor of Physics
Graduate Committee
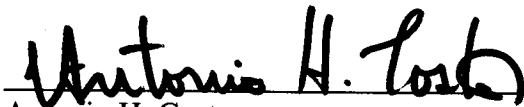
_____   7/11/03

David A. Brown
Professor of Electrical and Computer Engineering
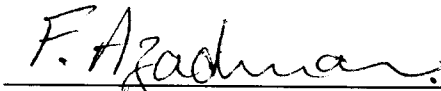Graduate Committee

_____   7/14/03

Dayalan P. Kasilingam
Associate Professor and Graduate Program Director, ECE
Graduate Committee

_____   7/11/03
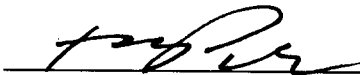
Antonio H. Costa
Professor and Chairperson, Electrical and Computer Engineering

_____   7/14/03

Farhad Azadivar
Dean, College of Engineering

_____   7/28/03

Richard J. Panofsky
Associate Vice Chancellor for
Academic Affairs and Graduate Studies

ABSTRACT

HIGHER ORDER HEXAHEDRAL FINITE ELEMENTS FOR ELECTROMAGNETIC MODELING

By Milan M. Ilić

Higher order hierarchical curved hexahedral finite elements are proposed for computational modeling in electromagnetics. The proposed volume elements for modeling of geometry are generalized curvilinear interpolatory hexahedra of higher (theoretically arbitrary) geometrical orders. The proposed basis functions for modeling of fields within the elements are hierarchical curl-conforming polynomial vector basis functions of higher (theoretically arbitrary) approximation orders. The new elements are implemented for geometrical orders from 1 to 4 and field-approximation orders from 1 to 10 in the same Galerkin-type finite element method and applied to analysis of both closed- and open-region electromagnetic problems. The elements can be as large as about $2\lambda \times 2\lambda \times 2\lambda$ (λ being the wavelength in the medium occupying the element under consideration), which is 20 times the traditional low-order modeling discretization limit of $\lambda/10$ in each dimension. The examples in analysis of electromagnetic cavities show excellent flexibility and efficiency of the new elements at modeling of both field variation and geometrical curvature, and their excellent properties in the context of *p*-refinement of solutions, for models with both flat and curved surfaces. The proposed higher-order (more precisely, low-to-high order) method offers considerably improved accuracy over the existing techniques, as well as significantly faster convergence as the number of unknowns increases. The reduction in the number of unknowns is by an order of magnitude when compared to low-order solutions.

To Andjelija

   whose love sustains me every day

   and

to Miodrag, Mirjana and Nevena
   my first teachers.

TABLE OF CONTENTS

LIST OF FIGURES

LIST OF TABLES

1. INTRODUCTION

Modern technological trends in telecommunications, wireless applications and computer engineering demand a constant development and improvement of reliable tools that can handle extremely complex electromagnetic (EM) problems arising in these applications, and that can enable efficient Computer Aided Design (CAD) of supporting EM structures, circuits, and devices. Typical examples of applications closely relying on CAD in radio-frequency (RF) and microwave/millimeter-wave engineering, recently developing at an extremely fast rate, are the radio-based (wireless) local-area networks or LANs (e.g., IEEE 802.11 standard), local multipoint distribution systems (LMDS), global positioning systems (GPS), microwave video distribution systems (MVDS), Bluetooth systems, third generation (3G) cellular phone systems including the global system for mobile communications (GSM) and personal communications service (PCS), high-speed digital electronics systems (as clock frequencies move well into the gigahertz range), etc. All of these, relatively newer, applications join the other, already well-established, applications in the RF and microwave engineering, such as radio astronomy, satellite communications, radar, heating, etc [1].

The successful realization of high-frequency (HF) components and devices crucial for these applications is heavily dependent on CAD and, the general tendency of all emerging designs and standards being to push the operating frequencies towards the higher end of the spectrum, the need for powerful computational tools that will allow fast and accurate EM analysis of metallic and/or dielectric/magnetic structures (antennas, RF and microwave circuits, high-speed digital circuits and interconnects, etc.) is now greater than ever.

Class of EM problems that can be effectively analyzed using analytical and/or asymptotical methods [e.g., Geometrical Theory of Diffraction (GTD) and Physical Optics (PO)] is relatively narrow since it includes only the structures possessing high levels of symmetry and/or structures that are, electrically, either very large or very small. Practical limitations of analytical and asymptotical methods compel the development of rigorous numerical techniques, able to cope with robust real-world EM problems, and their implementation in specialized CAD tools. In order to accelerate the design process and eliminate the (otherwise necessary and extremely costly) cut-and-try procedures, utilization of such CAD tools represents an absolute necessity.

Rigorous numerical methods developed during the past four decades can be roughly classified in three basic groups:

- frequency-domain integral equation methods, often synonymically referred to as Methods of Moments (MoM) [2-8], which are then subdivided into Surface Integral Equation (SIE)-based and Volume Integral Equation (VIE)-based methods,

- frequency-domain differential equation method or Finite Element Method (FEM) [9-60], and

- time-domain differential equation method, i.e., Finite-Difference Time-Domain method (FD-TD).

Although being rigorous and generally very robust, none of the methods is capable of handling all varieties of EM problems and no two methods are equally effective at dealing with specific classes of problems. For instance, SIE formulation in conjunction with MoM is, in the opinion of the author, the "best" choice for modeling of three-dimensional (3D) open-region antenna and scattering problems that predominantly consist of metallic surfaces and wires, and include some homogeneous

dielectric parts. On the other hand, finite-element (FE) techniques, are extremely efficient at modeling of 3D structures that predominantly consist of arbitrary shaped heterogeneous (isotropic or anisotropic) nonmetallic material sections. To fully benefit from different approaches and to further extend the applicability of the particular computational technique, two (or more) methods can be combined together to form a variety of hybrid methods such as Finite Element – Boundary Integral (FE-BI) method [61-64], Finite Element Method – Method of Moments (FEM-MoM) [65-69], and others.

1.1.   Fundamental concepts of FEM modeling and thesis goal

FEM is a numerical technique for obtaining approximate solutions to boundary-value problems of mathematical physics [9]. The method was first proposed in 1940s and was firstly used for aircraft design and in Civil Engineering. Today FEM has become recognized as a general method of wide applicability to engineering and mathematical problems.

FE techniques (with hybrid variations) represent, one of the most important subsets of numerical methods, widely used in the modern analysis of EM problems. FEM incorporates two very important qualities: flexibility of geometrical modeling and ability to efficiently model inhomogeneous media; the latter extremely important in electromagnetics, since the majority of applications require field simulations in inhomogeneous media [12]. Further more, it is very important to note that hybridization of FE techniques with integral equation techniques leads to theoretically exact approaches, which combine the best qualities of volume and surface formulations.

The main idea in FEM is to replace the original problem domain with the finite number of subdomains (domain or spatial discretization), within which the unknown function is then approximated by a sum of the simple, known, functions (interpolation

or basis functions) multiplied by the unknown weighting coefficients (e.g., polynomials). Applying the appropriate procedure (e.g., Galerkin testing procedure), a system of linear algebraic equations, with the weighting coefficients as unknowns, is formed (equation discretization). Solving for the unknown coefficients and substituting them back in the original expansion sum, an approximate solution of the original problem is obtained.

Problems under consideration in this thesis are the vector-type EM problems, whose analysis has been, at first, performed using simple, node based, finite elements (where each Cartesian component of the vector field is treated as a scalar function). This approach has difficulties in handling the boundary conditions (BCs) at material interfaces, in modeling the fields at sharp edges, and solutions are polluted with nonphysical (spurious) modes. Newly developed, vector finite elements [14-19], have been recently proposed as a modern foundation for FEM modeling of vector electromagnetic problems. It has been demonstrated that they overcome all of these major problems in EM applications. However, most of the existing FEM electromagnetic tools are small-domain low-order h-adaptive techniques – the electromagnetic structure is modeled by many electrically small geometrical elements, the fields within the elements are approximated by low-order basis functions and the increase of accuracy is obtained by (computationally costly) refinement of the geometrical mesh. This results in a very large number of unknowns necessary to achieve satisfactory accuracy and considerably limits the practicality of the method. Contrary to this, the author proposes a large-domain higher order p-adaptive capable approach – the domain is divided into "small" number of (electrically) large subdomains, higher order (arbitrary-order) basis functions are used to approximate the fields within the elements, and the increase in accuracy of the solution can be obtained by increasing the order of the field approximation whereas the possibility of mesh refinement remains unaffected.

Higher order FEM modeling has been rather neglected in the past decade (mostly due to denser resulting matrices and poorer orthogonality properties especially when hierarchical schemes are used) and has only recently become more investigated [37-42,46-49]. In the most recent publications the generally accepted postulate that interpolatory higher order vector finite elements lead to better conditioned matrices than hierarchical vector finite elements has been questioned [47], and orthogonalization procedures and iterative solvers suitable for hierarchical higher order FEM modeling have been proposed [48,49]. Nevertheless, most authors still use triangular, tetrahedral or triangular prism elements, which perform poorly in satisfying the boundary conditions and are incapable of having large dimensions. Such techniques still require very fine meshes regardless of the higher order field approximation, hence the reduction of the number of unknowns is not fully pronounced. More precisely, the elements are generally on the order of $\lambda/10$ in each dimension, λ being the wavelength in the medium, in both closed-region (e.g., electromagnetic cavity) and open-region (e.g., antenna and scattering) problems. This results in a very large number of unknowns (unknown field-distribution coefficients) needed to obtain results of satisfactory accuracy, with all the associated problems and enormous requirements in computational resources. An alternative which can effectively deal with the stated problems and can greatly reduce the number of unknowns, as well as enhance further the accuracy and efficiency of the FEM analysis in all classes of applications is the higher order large-domain modeling using hexahedral elements [20-25].

The goal of this thesis is the development of novel higher order elements in FEM, which would result in faster, more accurate and less demanding computational techniques in terms of hardware. The growing need for rapid, accurate and flexible EM modeling tools (which would not require supercomputers, but could be run on much simpler and less expensive machines such as PCs), justifies the efforts pointed in this direction and strongly encourages the development of such tools.

2. DIFFERENTIAL EQUATIONS FOR TIME-HARMONIC ELECTROMAGNETIC FIELDS AND DISCRETIZATION BY MEANS OF THE FINITE ELEMENT METHOD

2.1. Introduction

Basic theoretical aspects of 3-D modeling in electromagnetics are presented in this Section. Differential equation and boundary conditions governing the behavior of the time-harmonic EM fields in the "strong" sense are presented first. Inhomogeneous electric and magnetic vector wave equations are then derived and the usual "weak" finite element discretization of thus obtained boundary value problem is briefly described.

2.2. Maxwell's equations and the double-curl differential equation; E and H formulations

Consider a source-free region (spatial domain) V bounded by a closed surface S, as shown in Fig. 2.1. The domain is divided into homogeneous, or continuously inhomogeneous, subdomains (elements) V^e $(e = 1,...,N_e)$ such that $V = \bigcup_{e=1}^{N_e} V^e$. This being the case, in any domain V^e, constitutive equations can be written as

$$\boldsymbol{D} = \varepsilon^e \boldsymbol{E} , \qquad \text{and} \tag{1}$$

$$\boldsymbol{B} = \mu^e \boldsymbol{H} , \tag{2}$$

and Maxwell's equations are

$$\nabla \times \boldsymbol{E} = -\mathrm{j}\omega\mu^e \boldsymbol{H} , \tag{3}$$

$$\nabla \times \boldsymbol{H} = \mathrm{j}\omega\varepsilon^e \boldsymbol{E} , \tag{4}$$

$$\nabla \cdot (\varepsilon^e \boldsymbol{E}) = 0 , \qquad \text{and} \tag{5}$$

$$\nabla \cdot (\mu^e \boldsymbol{H}) = 0 , \tag{6}$$

where $\boldsymbol{E}$ and $\boldsymbol{H}$ represent complex electric and magnetic field vectors, respectively, μ^e is the complex permeability, ε^e is the complex permittivity of the medium in the e-th subdomain and ω is the angular frequency of the implied time-harmonic variation. Medium parameters, ε and μ, can also be described as $\varepsilon = \varepsilon' - \mathrm{j}\sigma/\omega = \varepsilon_0\varepsilon_\mathrm{r}$ and $\mu = \mu_0\mu_\mathrm{r}$, where ε_0 and μ_0 are, respectively, permittivity and permeability of the vacuum, ε_r and μ_r are the corresponding relative complex permittivity and permeability[1], and σ is the specific conductivity of the medium. Finally, $\boldsymbol{D}$ and $\boldsymbol{B}$ are the electric and magnetic flux density vectors, respectively.

Maxwell's equations are subject to boundary conditions, which govern the natural behavior of the fields at the interfaces between two adjacent domains. Consider, for instance, the interface between the i-th and j-th domain, S_{ij}, which is shown in Fig. 2.2. Natural boundary conditions can be mathematically expressed as

---

[1] Additionally, ε_r and μ_r can be tensors, but this case is not particularly addressed in the thesis.

$$n\times(E_i - E_j) = 0, \tag{7}$$

$$n\cdot(\varepsilon^i E_i - \varepsilon^j E_j) = 0, \tag{8}$$

$$n\times(H_i - H_j) = 0, \tag{9}$$

$$n\cdot(\mu^i H_i - \mu^j H_j) = 0. \tag{10}$$

n being the unit vector normal to surface S_{ij}. In the special cases, when one of the media becomes a perfect electric conductor (PEC), or perfect magnetic conductor (PMC), as a pure mathematical concept, boundary conditions at such interfaces, S_{pec} and S_{pmc}, reduce to

$$n\times E = 0, \quad \text{on } S_{\text{pec}} \tag{11}$$

$$n\cdot H = 0, \quad \text{on } S_{\text{pec}} \tag{12}$$

$$n\times H = 0, \quad \text{on } S_{\text{pmc}}, \quad \text{and} \tag{13}$$

$$n\cdot E = 0, \quad \text{on } S_{\text{pmc}}. \tag{14}$$

Natural boundary conditions with additional essential boundary conditions, which determine the tangential components of the fields on the domain boundary surface S, ensure the uniqueness of the solution of equations (1)-(6)[2]. Boundary conditions that need to be imposed on S are either those of perfect electric/magnetic walls, in which case the problem belongs to a class of closed-region problems, (e.g., a cavity problem) or those that couple the fields (and equations) already defined in the interior of V with

---

[2] Conditions under which the uniqueness of the solution to the Maxwell's equations is guaranteed can be found in [71].

fields existing to the exterior of *V*, in which case the problem belongs to a class of open-region problems, (e.g., radiation and scattering problems).
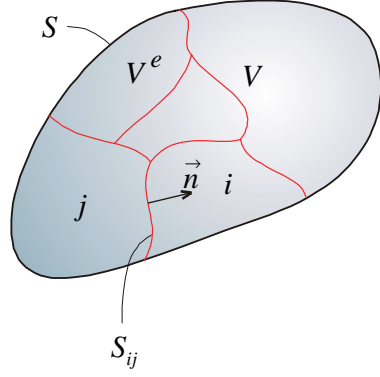
Fig. 2.1. Domain *V* bounded by a closed surface *S*.
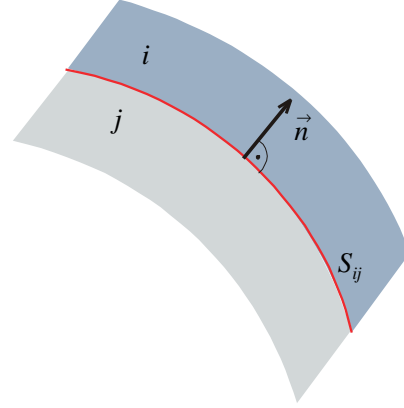
Fig. 2.2. Interface between two domains.

System (3)-(6) can be solved using potentials or, alternatively, directly for *E* and/or *H*. Choosing to solve the system directly reveals more possible choices: elimination of *H* or *E* (which, respectively, leads to electric or magnetic field wave equation), and solving for the other, or solving directly for both. The last approach is usually avoided, especially in numerical approaches since it generates more unknowns.

Electric and magnetic field wave equations (also referred to as *E* and *H* formulations of the double-curl differential equation) for the inhomogeneous medium, obtained from (3) and (4) by eliminating *H*, or *E* in the usual way [70], respectively read

$$\nabla \times \left(\mu_r^{e^{-1}} \nabla \times E \right) - k_0^2 \varepsilon_r^e E = 0 , \qquad \text{and} \tag{15}$$

$$\nabla \times \left(\varepsilon_r^{e^{-1}} \nabla \times H \right) - k_0^2 \mu_r^e H = 0 , \tag{16}$$

k_0 being the free-space wave number defined as

$$k_0 = \omega^2 \varepsilon_0 \mu_0. \tag{17}$$

Both formulations, E and H, theoretically lead to the same results, hence the choice of either formulation is generally based on the ease of implementation of the boundary conditions in particular problem. In numerical (approximate) solutions, however, different formulations experience different convergence properties and will thus lead to results of different accuracies [11][3]. Without reducing generality, we adopt the E formulation of the double-curl differential equation (together with accompanying boundary conditions) as the initial boundary-value problem and present its approximate solution next. All of the following derivations can be carried out for the H formulation in the dual fashion.

When $\omega \neq 0$ Maxwell's equations form a dependent system. Divergence equations (5) and (6) can be derived directly from the curl equations (3) and (4), hence if either of the double-curl differential equations is being solved, they are implicitly satisfied. When $\omega = 0$, however, E and H fields are decoupled and Maxwell's equations (and natural boundary conditions) are no longer dependent. In this case, if a double-curl differential equation is solved alone, without explicit enforcement of the divergence equations (5) and (6), a problem can arise in the eigenvalue analysis (e.g., analysis of cavities) when additional, nonphysical, modes appear as a solution besides the trivial one ($E = 0 / H = 0$). These solutions do not satisfy all of the Maxwell's equations, and they are the most common sources of the so-called *spurious modes*[4].

---

[3] For instance, it is shown that in the FEM analysis of rectangular waveguides, the TE modes are obtained more accurately using the E formulation, while the TM modes are obtained more accurately using the H formulation.

[4] Other types of nonphysical solutions may also spoil the solution in the discretized problem (e.g., a dependent set of basis functions) [43].

The important feature of the presented differential equation approach to EM problems is that the resulting mathematical forms allow efficient modeling of arbitrarily inhomogeneous media. Not only can media parameters ε_r and μ_r be non-constant, but they can also have the form of tensors, thus allowing the modeling of unisotropic media as well. This is one of the most exploited advantages of FEM, making it a preferable choice over the integral equation techniques employing potentials and Green's functions (e.g., MoM), in EM problems involving inhomogeneous and/or unisotropic domains.

2.3.   Approximate solution of the double-curl differential equation

Double-curl differential equation (15), obtained from the system of partial differential equations (3)-(6), with properly defined natural and essential boundary conditions, constitutes a "strong" boundary value problem. The term "strong" is used in a sense that the required solution is strongly regulated by the boundary conditions, i.e., it is required that the continuity of the unknown function and its derivatives be satisfied up to the order of the partial differential equations involved. In the absence of the analytical solution, approximate (numerical) solutions are sought. Generally, numerical procedures avoid solving the original, "strong", boundary-value problem and seek alternative, "weak", representations more suitable for discretization. To achieve this, the boundary conditions are weakened and thus the set of possible approximate solutions is broadened. Two of the most commonly used methods that yield the "weak" representations for the FEM modeling are the *variational principle* and the *weighted residual* method. The two methods are closely related and in many cases final expressions obtained using one or the other will coincide. However, while the formulation through a weighted residual method can always be applied, "weak" formulation obtained from a variational principle may be obtained only when the corresponding functional exists [11]. We adopt the weighted residual method as the

tool for obtaining the "weak" formulation of (15), suitable for discretization by our FEM method.

To briefly illustrate the application of the weighted residual method in general, consider equation (15) written in an operator form

$$\mathcal{L}\,E = g \,, \tag{18}$$

$\mathcal{L}$ being the linear operator, and E and g being the unknown field function and the known excitation function, respectively. In this case $g = 0$, however, in order to maintain the generality of the method this identity is not yet imposed. Residual of (18) over the domain is

$$R = \mathcal{L}\,E - g \,, \tag{19}$$

the weighted residual of (18) is formed as

$$WR = \int_V w \cdot \mathcal{L}\,E \,\mathrm{d}V - \int_V w \cdot g \,\mathrm{d}V \,, \tag{20}$$

and it is required that $WR = 0$, namely

$$WR = \int_V w \cdot \mathcal{L}\,E \,\mathrm{d}V - \int_V w \cdot g \,\mathrm{d}V = 0, \tag{21}$$

where w belongs to a set of chosen weighting functions. It is clear that any solution that satisfies (18) will also satisfy (21), however, while the solution E to equation (18) is strongly driven by the boundary conditions, equation (21) allows a broader choice of solutions, since it only requires that finite integrals are obtained. In other words, "strong" continuity conditions implied in (18) can be relaxed.

2.4.   Discretization of the continuous problem

The discretization procedure transforms the continuous problem into a discrete one having a finite number of degrees of freedom. The discrete problem is then solved and its solution gives the approximation of the original, continuous, problem.

The discretization starts with the selection of the finite set of functions, *basis functions*, whose linear combination will give the approximation of the unknown function. For the unknown vector function E we can construct the approximation in two essentially different forms

$$\tilde{E} = \sum_{j=1}^{N_{\mathrm{b}}} \boldsymbol{\beta}_j \, h_j, \qquad \text{or} \tag{22}$$

$$\tilde{E} = \sum_{j=1}^{N_{\mathrm{b}}} \alpha_j \, \boldsymbol{f}_j, \tag{23}$$

where α_j and $\boldsymbol{\beta}_j$ represent the unknown coefficients (or unknown parameters, or degrees of freedom), h_j and $\boldsymbol{f}_j$ stand for the known functions belonging to a set of chosen basis functions, $\tilde{E}$ stands for the approximation of E, and N_{b} is the total number of employed basis functions. From now on, however, we will deal with the approximation function only, hence to keep the expressions more simple the tilde sign will be dropped. Basis functions h_j ($j = 1,..., N_{\mathrm{b}}$) used in the first form of the approximation are scalar, and the finite elements obtained from this form are thus called *scalar* (or *node-based*) finite elements. On the other hand, basis functions $\boldsymbol{f}_j$ ($j = 1,..., N_{\mathrm{b}}$) involved in the second form of the approximation are vector functions and the corresponding finite elements are called *vector* (or *edge-based*) finite elements. The earliest analyses of vector electromagnetic problems have been performed using the node-based finite elements [13,27,28,39] and each Cartesian

component of the vector field had been treated as a scalar function. This approach has difficulties in handling the boundary conditions at material interfaces, in modeling the fields at sharp edges, and solutions are polluted with nonphysical, spurious modes whose origin was briefly discussed in Section 2.2. Vector finite elements [14-19] have been recently proposed as a modern foundation for FEM modeling of vector electromagnetic problems and it has been demonstrated that they overcome all of the major problems in EM applications. Thus in our discretization process, we adopt the second form of the field expansion (approximation) given by (23).

Once the expansion of the unknown function has been done using the set of chosen basis functions, the discretization of the continuous problem is achieved using either one of the previously mentioned methods, i.e., variational principle or the weighted residual method. The discretization of a variational principle is done by the *Ritz method* [11] whereas different methods for discretization of the weighted residual "weak" representations are obtained using different types of weighting (testing) functions. The choice of the testing functions (which are either scalar or vector, depending on the unknown function) is generally arbitrary, provided that they are linearly independent, and that their number is at least the same as the number of the unknown parameters.

If the number of testing functions is the same as the number of unknowns, the resulting algebraic systems are square, and that is the case we adopt. Thus we choose a proper set of functions w_i $(i = 1,...,N_b)$ and construct N_b weighted residual equations of the general form given by (21), where the unknown vector function E has been approximated by the finite series expansion shown in (23), and, taking the advantage of linearity of the operations involved, obtain the following $N \times N$ system of linear algebraic equations

$$\sum_{j=1}^{N_b} \alpha_j \int_V w_i \cdot \mathcal{L} f_j \, dV - \int_V w_i \cdot g \, dV = 0, \qquad i = 1,...,N_b, \tag{24}$$

which can also be written in the matrix form

$$[K]\{\alpha\} = \{g\}, \tag{25}$$

where the elements of the system matrix, $[K]$, and the free-term column vector, $\{g\}$, are given as

$$K_{ij} = \int\limits_V w_i \cdot \mathcal{L} f_j \, dV \qquad \text{and} \tag{26}$$

$$g_i = \int\limits_V w_i \cdot g \, dV, \tag{27}$$

respectively. The system is then solved for the unknown scalar coefficients α_j $(j = 1,..., N_b)$, and the approximate solution of the unknown function E is obtained by substituting the coefficients back into expansion (23).

The better known methods for discretization of the weighted residual integral form used in FEM are *collocation method* or *point-matching* (weighting functions are in the form of the Dirac delta-functions), *piecewise-constant method* (weighting functions are equal to unity in given subdomains and zero in the rest), *Galerkin method* (weighting functions are the same as the basis functions), and *Petrov-Galerkin method* (weighting functions are arbitrary). For the reasons that will be explained in the following Section, we choose the Galerkin method, $w_i = f_i$ $(i = 1,..., N_b)$, as the testing procedure in our FEM technique.

The described discretization concept gives a sound mathematical basis for the discretization by means of the finite elements. The concept is, however, general and not specific of FEM modeling only. The specificity of FEM lies in the way in which the unknown function is approximated (expanded) which will be explained next.

2.5. Formulation of the finite element method

In FEM, the unknown function is not approximated using a single set of basis functions over the entire domain of interest, V. Instead, the domain is first divided into smaller domains, V^e, which are called finite elements (e.g., as in Fig. 2.1), and the unknown function is approximated locally, over each element, as a linear combination of the, also locally, chosen sets of basis functions.

Firstly, the FE concept implies that the global "weak" integral form (21) should actually be applied locally, over each element, whereas the global integral form should coincide with the sum of thus obtained local forms. Hence, substituting (15) into (21) we get the local "weak" integral form for our problem

$$\int_{V^e} \boldsymbol{w} \cdot \nabla \times \left(\mu_r^{e-1} \nabla \times \boldsymbol{E} \right) dV - k_0^2 \int_{V^e} \boldsymbol{w} \cdot \varepsilon_r^e \boldsymbol{E} \, dV = 0 . \tag{28}$$

Invoking the vector analogue to Green's first identity [71]

$$\oint_S (\boldsymbol{A} \times \nabla \times \boldsymbol{B}) \cdot d\boldsymbol{S} = \int_V (\nabla \times \boldsymbol{A}) \cdot (\nabla \times \boldsymbol{B}) \, dV - \int_V \boldsymbol{A} \cdot \nabla \times \nabla \times \boldsymbol{B} \, dV , \tag{29}$$

letting $\boldsymbol{A} = \boldsymbol{w}$, $\nabla \times \boldsymbol{B} = \mu_r^{e-1} \nabla \times \boldsymbol{E}$, and applying it to the first integral in the weighted residual equation (28), after rearranging the terms we get

$$\int_{V^e} \mu_r^{e-1} (\nabla \times \boldsymbol{w}) \cdot (\nabla \times \boldsymbol{E}) \, dV - k_0^2 \int_{V^e} \varepsilon_r^e \boldsymbol{w} \cdot \boldsymbol{E} \, dV - \oint_{S^e} \mu_r^{e-1} \boldsymbol{w} \times (\nabla \times \boldsymbol{E}) \cdot d\boldsymbol{S} = 0 , \tag{30}$$

where V^e and S^e stand for the volume and the bounding surface of the e-th domain (e.g., as in Fig. 2.1) and $d\boldsymbol{S} = \boldsymbol{n}^e dS$, $\boldsymbol{n}^e$ being the unit normal on S^e pointing outward of the e-th domain. In this final integral form, the unknown vector function $\boldsymbol{E}$ no longer appears under the double-curl operator, hence a possible solution $\boldsymbol{E}$ needs to be

only a continuous function (in the sense to keep the $\nabla \times \boldsymbol{E}$ finite) and there are no constraints regarding the continuity of the expression $\mu_r^{-1} \nabla \times \boldsymbol{E}$, which was required to be continuous in the original problem (15) [and this was strongly imposed by the condition (9)].

Secondly, the expansion (23) should be written separately for each element, namely

$$\boldsymbol{E} = \sum_{j=1}^{N_b^e} \alpha_j^e \, \boldsymbol{f}_j^e, \quad e = 1,...,N_e, \tag{31}$$

where α_j^e and $\boldsymbol{f}_j^e$ $(j = 1,...,N_b^e)$ are the unknown scalar coefficients (degrees of freedom) and corresponding basis functions associated with the e-th element, respectively, and N_b^e is the total number of basis function used in the e-th element.

Thirdly, a proper set of testing functions $\boldsymbol{w}_i^e$ $(i = 1,...,N_b^e; e = 1,...,N_e)$ should be chosen for each element. The choice of the same basis and testing functions, $\boldsymbol{w}_i^e = \boldsymbol{f}_i^e$ $(i = 1,...,N_b^e; e = 1,...,N_e)$, i.e., Galerkin method, comes naturally in our problem, since after substituting (31) into (30) it can be concluded that the regulatory conditions for the basis and weighting functions are identical[5]. Besides, this choice will lead to algebraic systems with symmetric matrices[6], which can be extremely advantageous for the optimization of the calculation of the matrix parameters, matrix storage, and the inversion procedure.

---

[5] This is always the case when integration by parts (or equivalent procedure) is applied on the second order problems.

[6] This will always be the case when the operators are of the even order.

Fourthly, a system of linear algebraic equations is formed as shown by (24)-(27) only, again, locally for each element

$$\sum_{j=1}^{N_b^e} \alpha_j^e \left[\int_{V^e} \mu_r^{e^{-1}} (\nabla \times \boldsymbol{w}_i^e) \cdot (\nabla \times \boldsymbol{f}_j^e)\, \mathrm{d}V - k_0^2 \int_{V^e} \varepsilon_r^e \boldsymbol{w}_i^e \cdot \boldsymbol{f}_j^e\, \mathrm{d}V \right] -$$

$$- \oint_{S^e} \mu_r^{e^{-1}} \boldsymbol{w}_i^e \times (\nabla \times \boldsymbol{E}) \cdot \mathrm{d}\boldsymbol{S} = 0,$$

$$i = 1,...,N_b^e, \qquad e = 1,...,N_e, \tag{32}$$

with a total number of equations being

$$N_{\mathrm{eq}} = \sum_{e=1}^{N_e} N_b^e. \tag{33}$$

Expansion (31) was deliberately not applied in the surface-integral term at this point, and this term will be symbolically denoted as G_{s}^e. Sets of equations for each of the elements can be also written in the matrix form as

$$[K^e]\{\alpha^e\} = \{G_{\mathrm{s}}^e\}, \qquad e = 1,...,N_e \tag{34}$$

where the surface-integrals have been moved to the right-hand side of the equation and

$$[K^e] = [A^e] - k_0^2 [B^e], \tag{35}$$

$$A_{ij}^e = \int_{V^e} \mu_r^{e^{-1}} (\nabla \times \boldsymbol{w}_i^e) \cdot (\nabla \times \boldsymbol{f}_j^e)\, \mathrm{d}V, \tag{36}$$

$$B_{ij}^e = \int_{V^e} \varepsilon_r^e \boldsymbol{w}_i^e \cdot \boldsymbol{f}_j^e\, \mathrm{d}V, \qquad \text{and} \tag{37}$$

$$G^e_{s_i} = \oint_{S^e} \mu_r^{e^{-1}} \boldsymbol{w}_i^e \times (\nabla \times \boldsymbol{E}) \cdot \mathrm{d}\boldsymbol{S} , \tag{38}$$

where $i, j = 1,...,N^e_b$. To obtain a final system of equations, global numbering of the degrees of freedom should be introduced, according to which each local unknown α^e_j ($j = 1,...,N^e_b$; $e = 1,...,N_e$) is assigned a unique global number i ($i = 1,...,N_{eq}$). Matrices $[K^e]$, $[A^e]$, $[B^e]$ and vectors $\{\alpha^e\}$ and $\{G^e_s\}$ (originally N^e_b dimensional) can be expanded to become N_{eq} dimensional by introducing zero-valued elements in the rows and columns (for matrices only) for which the global degree of freedom does not belong to the element under consideration. The assembly of the global system

$$[K]\{\alpha\} = \{G_s\} , \tag{39}$$

is then formally achieved[7] by adding the local matrices and vectors, namely

$$[K] = \sum_{e=1}^{N_e} [K^e], \quad [A] = \sum_{e=1}^{N_e} [A^e], \quad [B] = \sum_{e=1}^{N_e} [B^e],$$
$$\{G_s\} = \sum_{e=1}^{N_e} \{G^e_s\}, \quad \{\alpha\} = \sum_{e=1}^{N_e} \{\alpha^e\} . \tag{40}$$

Finally, before the global system can be solved for $\{\alpha\}$, boundary conditions both natural and essential have to be enforced. Depending on the choice of basis functions and the type of boundary condition that needs to be imposed, different techniques are used to approach this problem. Typically, however, some of the conditions are enforced strictly, and some only in a distributional sense.

---

[7] Depending on the type of problem, the actual assembly process involves different programming techniques.

The main characteristic of the final system matrix $[K]$ obtained using FEM discretization is that it is generally sparse, having the non-vanishing entries located only in blocks on the main diagonal. This important feature allows the utilization of economical storage schemes (where only the nonzero coefficients of the matrix are stored) and fast iterative methods (e.g., the conjugate gradient method, having the matrix inversion time proportional to N_{eq}) to be used in the solution process of the global system of equations instead of direct methods (e.g., Gaussian elimination and its variations, having the inversion times proportional to N_{eq}^2 or N_{eq}^3), and it is greatly exploited whenever possible[8]. When the Galerkin testing procedure ($w_i^e = f_i^e$; $\forall i, e$) is used, from (36) and (37) we can conclude that ($\forall i, e$) $A_{ij}^e = A_{ji}^e$ and $B_{ij}^e = B_{ji}^e$, hence the individual element matrices as well as the final system matrix are symmetrical. This fact reduces by half the total number of the, computationally extremely expensive, volume-integrals A_{ij} and B_{ij} that need to be evaluated, and further economizes the matrix storage scheme and overall solution process.

It is interesting to note that irrespective of whether the variational or Galerkin weighted residual formulations are used, the same two volume-integrals of energy-related quantities, shown in (36) and (37) and called the Dirichlet (or stiffness) and metric (or mass) integrals, respectively, will appear as FEM matrix elements [50].

---

[8] Iterative methods are efficient only if the system matrices are well conditioned, since the actual number of operations and the CPU time depend on the number of iterations needed to achieve satisfactory accuracy, hence the choice of a direct or an iterative method will depend on the particular problem.

2.6.   Conclusion

A concise mathematical basis of the FEM modeling in electromagnetics has been given in this Section. Starting from the Maxwell's equations and boundary conditions for the time-harmonic EM fields, a general 3-D EM problem based on the *E*-formulation of the double-curl differential equation is derived and then discretized by means of the finite elements. In the process, the unknown electric field vector function *E* was approximated utilizing a general class of vector basis functions; weighted residual method was chosen as the tool for obtaining the "weak" integral form of the original problem, suitable for numerical solution; the "weak" formulation was discretized using the Galerkin testing procedure; and the assembly of the local and global algebraic systems is briefly described.

Although already having a significant number of choices made, the mathematical concepts described thus far still remain rather general. The main distinguishing feature of a FEM method, which mostly impacts the method's overall quality, efficiency, applicability, accuracy and speed, lays in the geometrical and mathematical characteristics of its basic building block – the finite element, or more specifically, in the type of the geometrical elements used for the spatial discretization (domain tessellation) and the choice of basis functions. Here also lays the most involving part (from both analytical and implementation/programming points of view) of the FEM technique development process and the originality of this particular thesis. Presented in the following two Sections are the higher order curved parametric hexahedral geometrical elements proposed for the spatial discretization and the hierarchical polynomial vector basis functions proposed for the field approximation, respectively.

3.   DOMAIN DISCRETIZATION USING HIGHER ORDER CURVED PARAMETRIC HEXAHEDRAL ELEMENTS

3.1.   Introduction

Brick [30] and tetrahedron [27,30,33,39,41,42], shown in Fig. 3.1(a) and (b), respectively, are very popular elements for the 3-D FEM domain tessellation in the analysis of EM problems. The first is attractive because of its simplicity in constructing volume meshes whereas tetrahedron is considered the simplest, fail-safe, element. It is often the element of choice for 3-D meshing, but requires sophisticated and computationally intensive meshing packages [29]. Also simple and attractive element, but not as often used, is triangular prism [38], shown in Fig. 3.1(c).

In principle, the choice of element-type for geometrical modeling involves a trade-off between the flexibility of the element at modeling different geometries on one side, and its mathematical complexity, on the other. Bricks, tetrahedra and triangular prisms, for instance, are simple to implement and their parameters are fast to compute. On the other hand, geometrical flexibility of these elements is poor and, because of their straight edges and planar sides, modeling of complex curved structures becomes exceedingly cumbersome and requires extremely fine meshes in order to achieve a satisfactory level of geometrical approximation. This, in turn, leads to the necessary reduction of elements' sizes, i.e., to small-domain (subdomain) techniques – the electromagnetic structure is modeled by volume geometrical elements that are electrically very small (typically on the order of $\lambda/10$ in each

dimension, λ being the wavelength in the medium). Ultimately, this results in a very large number of unknowns (unknown field-distribution coefficients) needed to obtain results of satisfactory accuracy, with all the associated problems and enormous requirements in computational resources and computational time.
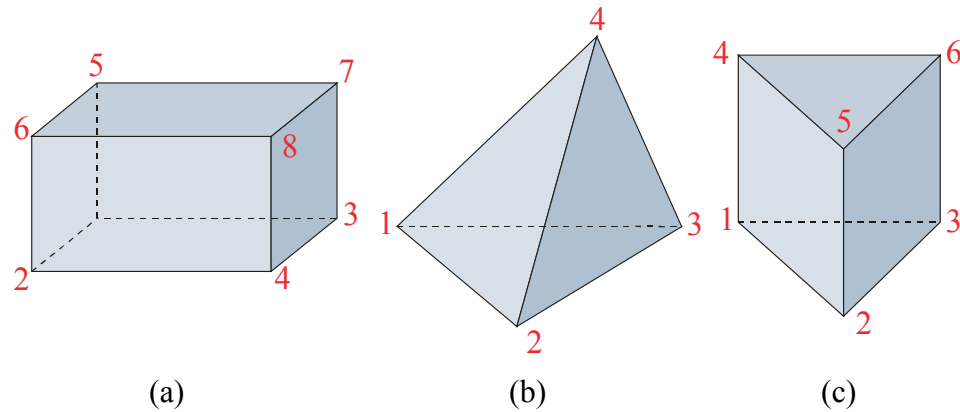
Fig. 3.1. Basic geometrical elements: (a) brick, (b) tetrahedron and (c) triangular prism.

Contrary to, by far the most often used, small-domain techniques, we propose the large domain computational approach [4-7,20-26] which can greatly reduce the number of unknowns for a given problem and enhance further the accuracy and efficiency of the FEM analysis in all classes of applications. This approach utilizes large geometrical elements (e.g., on the order of λ in each dimension) for the spatial discretization. To illustrate the difference between the two approaches, we present two models of an *H*-plane waveguide T-junction in Fig. 3.2: (a) the small-domain model with 2365 tetrahedral elements (660 nodes) generated by automatic segmentation in Femlab[9] and (b) the large-domain model with 4 hexahedral elements (20 nodes) generated manually. Having in mind that $a = \lambda/2$ for the dominant waveguide mode, please note that tetrahedral sides used in the small-domain model are indeed on the order of λ/10, whereas the longer sides of the hexahedral elements used in the large-

---

[9] Courtesy of COMSOL, Inc.

domain model are on the order of λ/2. Due to the flat nature of the waveguide structure shown in this particular example, large-domain modeling was accomplished using simple brick-like hexahedra only. However, in order to keep the elements as large as possible in general problems, which can involve non-planar curved structures, the use of more flexible (and, naturally, more complex) elements is required.

(a)   (b)
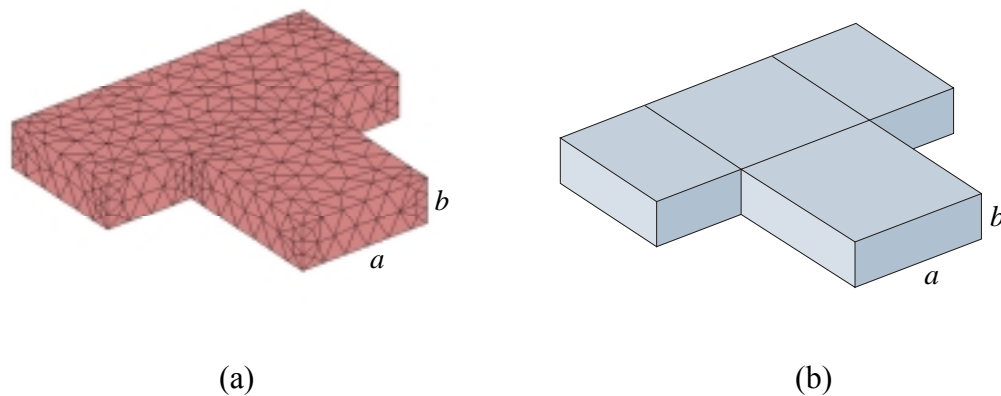
Fig. 3.2. (a) Small-domain and (b) large-domain models of an *H*-plane waveguide T-junction.

An attractive choice of flexible elements, with (possibly) curved sides, are generalized curved parametric hexahedra of higher (theoretically arbitrary) geometrical orders, which are adopted here as basic building blocks for geometrical modeling of 3-D electromagnetic structures of arbitrary shapes and material inhomogeneities. Although a form of general hexahedral elements was introduced as early as in 1988 [35], to the best knowledge of the author, they have never been widely adopted in the numerical modeling of EM problems, and there are very few published results that present actual implementation and use of hexahedral elements [36], especially of the orders higher than one (higher order elements). Apart from the results presented in [4-6] which demonstrate the efficient implementation of the first-order generalized hexahedra (trilinear hexahedra) in MoM VIE modeling, other examples of utilization of the generalized hexahedra were extremely hard to find.

Systematical development of arbitrary order interpolatory curved parametric hexahedra is presented next. Also shown are the derivations of the basic geometrical parameters and mathematical quantities required for the implementation of hexahedral elements in the new higher order FE technique.

3.2. Generalized curved parametric hexahedron

A generalized hexahedron [23-25,52] is determined by $M = (K+1)^3$ points (interpolation nodes) arbitrarily positioned in space, K ($K \geq 1$) being the geometrical order of the element. It can be described analytically as

$$r(u,v,w) = \sum_{i=1}^{M} r_i \hat{L}_i^K(u,v,w) = \sum_{m=0}^{K} \sum_{n=0}^{K} \sum_{l=0}^{K} r_{mnl} \, u^m v^n w^l, \qquad -1 \leq u,v,w \leq 1, \quad (41)$$

where r_1, r_2, …, r_M are the position vectors of the interpolation nodes, $\hat{L}_i^K(u,v,w)$ are Lagrange-type interpolation polynomials satisfying the Kronecker delta relation $\hat{L}_i^K(u_j,v_j,w_j) = \delta_{ij}$, with u_j, v_j and w_j representing the parametric coordinates of the j-th node, and r_{mnl} are constant vector coefficients which can be calculated from r_1, r_2, …, r_M. Both initially defined nodal vectors (interpolation nodes) r_i and calculated constant vectors r_{mnl} are given in the global Cartesian coordinates as $r_i = (x_i, y_i, z_i)$ and $r_{mnl} = (x_{mnl}, y_{mnl}, z_{mnl})$, respectively. Equation (41) defines a mapping from a *parent element*, in this case a reference cube occupying a $-1 \leq u,v,w \leq 1$ domain in the $u-v-w$ space, into a curved generalized hexahedron in $x-y-z$ space, as shown in Fig. 3.3.
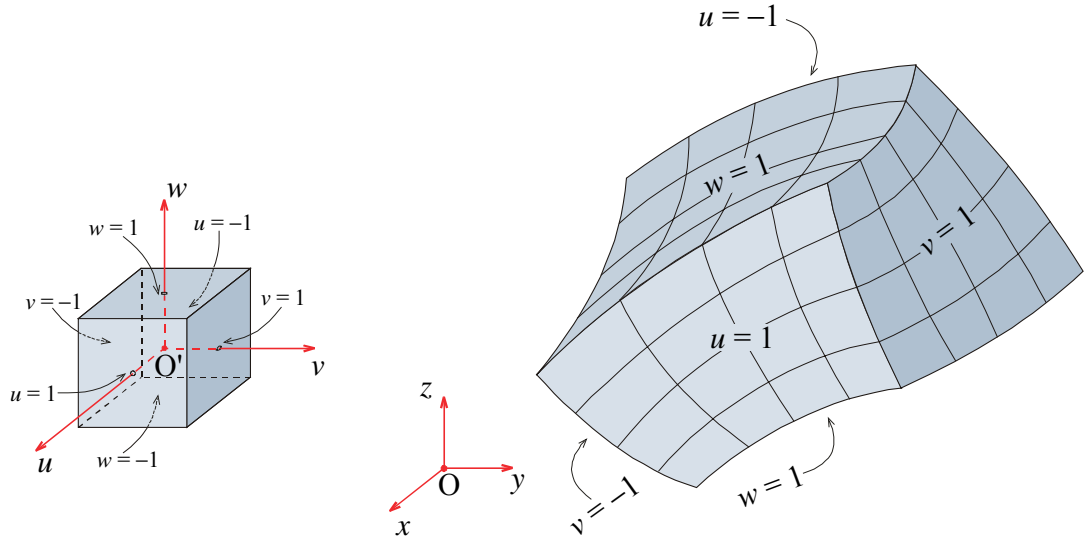
Fig. 3.3. Cube to hexahedron mapping defined by (41).

Shown in Fig. 3.4(a) is the first-order element ($K = 1$), called the trilinear hexahedron [4-7,22], along with the visible coordinate lines. It is determined solely by $M = 8$ interpolation points – its 8 vertices. Its edges and all coordinate lines are straight, whereas its sides, so-called *bilinear quadrilateral surfaces* [3-7], are somewhat curved (inflexed). Note that even these hexahedra provide the same or better flexibility for geometrical modeling of general electromagnetic structures as compared to commonly used elements in the form of bricks, tetrahedra, and triangular prisms. The second order element ($K = 2$), called the triquadratic hexahedron and shown in Fig. 3.4(b), is determined by $M = 27$ interpolation points arbitrarily positioned in space. Its edges and all coordinate lines are second-order polynomial curves. Its sides are curved and flexible and can easily approximate different curvatures. Of course, parametric bodies of higher ($K > 2$) geometrical orders provide even better flexibility and accuracy at modeling complex curved structures.
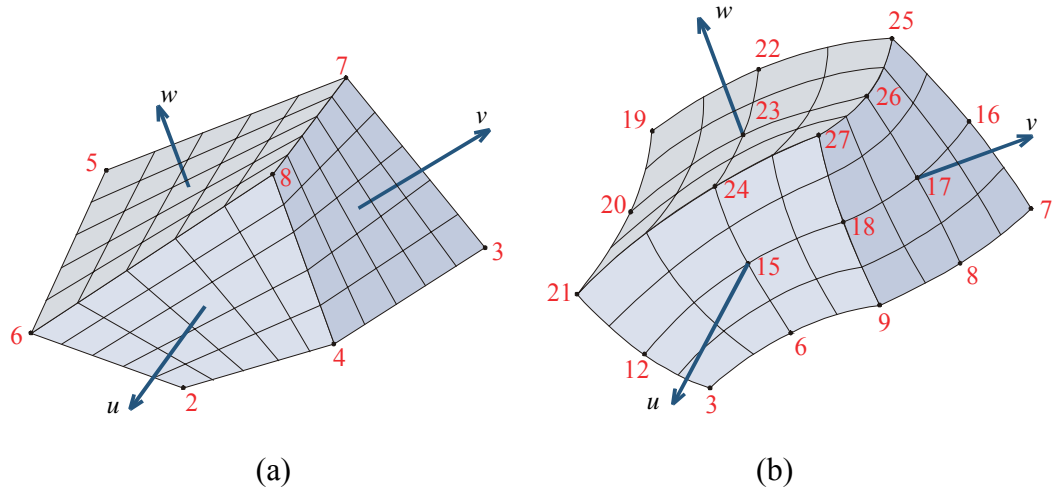
Fig. 3.4. (a) Trilinear hexahedron ($K=1$, $M=8$). (b) Triquadratic hexahedron ($K=2$, $M=27$).

Contrary to elsewhere widely used simple elements (e.g., tetrahedra and bricks), generalized hexahedra adopted here enable a whole range of element shapes (e.g., brick-like, slab-like, and rod-like planar hexahedra, as well as spherically-shaped, cylindrically-shaped, and elliptically-shaped curved hexahedra, and also other "irregular" and/or curved hexahedral shapes) to be used in a final FEM simulation model. To illustrate the potential and flexibility of higher order hexahedral modeling shown in Fig. 3.5(a) and (b) are, respectively, an ellipsoid and an elliptical cylinder (as examples of structures with pronounced curvature) modeled by a single second-order generalized hexahedron. The figures are obtained using piecewise planar approximations of the mathematically exact 3-D representations.
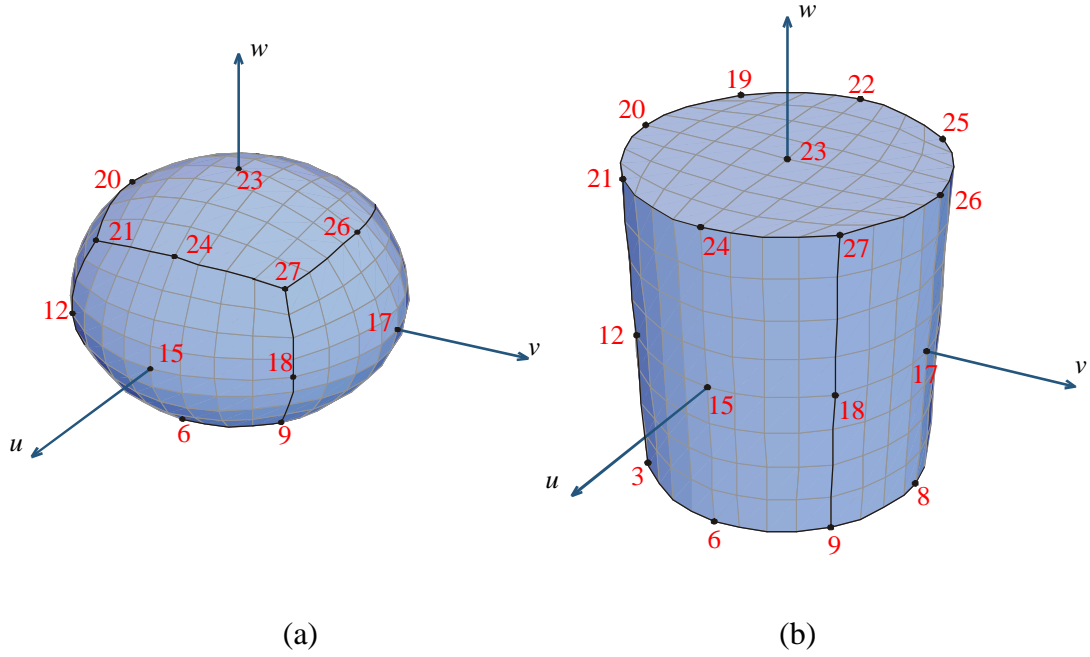
Fig. 3.5. Single-element second-order models of (a) an ellipsoid and (b) an elliptical cylinder.

3.3. Basic geometrical parameters and equations required for the implementation of the generalized hexahedral finite elements

3.3.1. Lagrange-type interpolation polynomials

To construct Lagrange-type interpolation polynomials $\hat{L}_i^K(u,v,w)$, needed for the $\boldsymbol{\rho} = (u,v,w)$ to $\boldsymbol{r} = (x,y,z)$ mapping defined by (41), we first define the Lagrange interpolating polynomials $L_m^K(u)$ on a linear interval $-1 \leq u \leq 1$ uniformly subdivided into K subintervals:

$$L_m^K(u) = \frac{(u-u_0)(u-u_1)...(u-u_{m-1})(u-u_{m+1})...(u-u_K)}{(u_m-u_0)(u_m-u_1)...(u_m-u_{m-1})(u_m-u_{m+1})...(u_m-u_K)} = \prod_{\substack{j=0 \\ j \neq m}}^{K} \frac{u-u_j}{u_m-u_j},$$

$$(42)$$

u_j being the uniformly spaced interpolating nodes defined as

$$u_j = \frac{2j - K}{K}, \qquad j = 0, 1, ..., K. \tag{43}$$

Polynomials $\hat{L}_i^K(u,v,w)$ are then constructed by simple multiplication of separate Lagrange interpolating polynomials, one in each direction of the element coordinates, namely

$$\hat{L}_i^K(u,v,w) = L_m^K(u) L_n^K(v) L_l^K(w), \qquad i = m(K+1)^0 + n(K+1)^1 + l(K+1)^2 + 1,$$
$$0 \le m,n,l \le K, \qquad\qquad 1 \le i \le M = (K+1)^3. \tag{44}$$

For the first order element ($K = 1$, $M = 8$) we thus obtain:

$$\hat{L}_1^1(u,v,w) = -\frac{1}{8}(u-1)(v-1)(w-1), \text{ node at } \boldsymbol{\rho}_1 = (-1,-1,-1);$$

$$\hat{L}_2^1(u,v,w) = \frac{1}{8}(u+1)(v-1)(w-1), \text{ node at } \boldsymbol{\rho}_2 = (1,-1,-1); ...,$$

$$\hat{L}_7^1(u,v,w) = -\frac{1}{8}(u-1)(v+1)(w+1), \text{ node at } \boldsymbol{\rho}_7 = (-1,1,1); \text{ and}$$

$$\hat{L}_8^1(u,v,w) = \frac{1}{8}(u+1)(v+1)(w+1), \text{ node at } \boldsymbol{\rho}_8 = (1,1,1). \tag{45}$$

Similarly, for the second order element ($K = 2$, $M = 27$), we have:

$$\hat{L}_1^2(u,v,w) = -\frac{1}{8}u(1-u)v(1-v)w(1-w), \text{ node at } \boldsymbol{\rho}_1 = (-1,-1,-1);$$

$$\hat{L}_2^2(u,v,w) = \frac{1}{4}(1-u)(1+u)v(1-v)w(1-w), \text{ node at } \boldsymbol{\rho}_2 = (0,-1,-1); ...,$$

$$\hat{L}_{14}^2(u,v,w) = (1+u)(1-u)(1+v)(1-v)(1+w)(1-w), \text{ node at } \boldsymbol{\rho}_{14} = (0,0,0); ...,$$

and

$$\hat{L}^2_{27}(u,v,w) = \frac{1}{8}u(1+u)v(1+v)w(1+w)\,,\ \text{node at}\ \boldsymbol{\rho}_{27} = (1,1,1)\,.\tag{46}$$

Analogous expressions hold for higher order $(K > 2)$ parametric bodies.

3.3.2. Vector algebra and analysis in the generalized curvilinear system (GCS)

Consider the $\boldsymbol{\rho} = (u,v,w)$ to $\boldsymbol{r} = (x,y,z)$ mapping defined by (41). The total differential of a position vector is defined by

$$\mathrm{d}\boldsymbol{r} = \frac{\partial \boldsymbol{r}}{\partial u}\mathrm{d}u + \frac{\partial \boldsymbol{r}}{\partial v}\mathrm{d}v + \frac{\partial \boldsymbol{r}}{\partial w}\mathrm{d}w\ ,\tag{47}$$

Equation (47) implicitly defines so-called *unitary vectors*

$$\boldsymbol{a}_u = \frac{\partial \boldsymbol{r}}{\partial u}\ ,\ \boldsymbol{a}_v = \frac{\partial \boldsymbol{r}}{\partial v},\ \text{and}\ \boldsymbol{a}_w = \frac{\partial \boldsymbol{r}}{\partial w},\tag{48}$$

described in some detail in [70][10]. Geometrically, unitary vectors represent tangents to curves defined in *r*-space when the other two coordinates are kept constant. It is important to stress that, since generalized curved hexahedron is defined by arbitrarily positioned nodes, unitary vectors $\boldsymbol{a}$ are neither mutually perpendicular, nor are they of the unit length[11] (except in the special cases when generalized hexahedron reduces to a brick, or a cube). The three differential vectors $\boldsymbol{a}_u\mathrm{d}u$, $\boldsymbol{a}_v\mathrm{d}v$ and $\boldsymbol{a}_w\mathrm{d}w$ define a differential volume given by

$$\mathrm{d}V = (\boldsymbol{a}_u \times \boldsymbol{a}_v)\cdot\boldsymbol{a}_w\ \mathrm{d}u\mathrm{d}v\mathrm{d}w = J\ \mathrm{d}u\mathrm{d}v\mathrm{d}w\,,\tag{49}$$

---

[10] In [73] the unitary vectors are designated as the *primary vectors*.
[11] Generally, unitary vectors are not even of the dimension of length (e.g., $\partial\boldsymbol{r}/\partial\phi$ and $\partial\boldsymbol{r}/\partial\theta$ in the $r-\theta-\phi$ spherical coordinate system).

where

$$J = (\boldsymbol{a}_u \times \boldsymbol{a}_v) \cdot \boldsymbol{a}_w = (\boldsymbol{a}_v \times \boldsymbol{a}_w) \cdot \boldsymbol{a}_u = (\boldsymbol{a}_w \times \boldsymbol{a}_u) \cdot \boldsymbol{a}_v , \tag{50}$$

represents the Jacobian of the $\boldsymbol{\rho}$ to $\boldsymbol{r}$ transformation.

Next we introduce three *reciprocal unitary vectors* [72,73] defined by

$$\boldsymbol{a}_u^r = \frac{\boldsymbol{a}_v \times \boldsymbol{a}_w}{J} , \; \boldsymbol{a}_v^r = \frac{\boldsymbol{a}_w \times \boldsymbol{a}_u}{J} , \text{ and } \boldsymbol{a}_w^r = \frac{\boldsymbol{a}_u \times \boldsymbol{a}_v}{J} . \tag{51}$$

Geometrically, reciprocal unitary vector $\boldsymbol{a}_{q_i}^r$ is perpendicular to the surface defined

when q_i is kept constant, where q_i $(i = 1, 2, 3)$ stands for any of the coordinates u, v

and w, respectively. This implies that for $q_i = \pm 1$, $\boldsymbol{a}_{q_i}^r$ defines the outward/inner

normal to the hexahedron surface. Unitary vectors and reciprocal unitary vectors

satisfy the relation

$$\boldsymbol{a}_{q_i} \cdot \boldsymbol{a}_{q_j}^r = \delta_{ij} , \qquad i, j = 1, 2, 3 \tag{52}$$

and the unitary vectors can be expressed in terms of the reciprocal unitary vectors as

$$\boldsymbol{a}_u = J \, \boldsymbol{a}_v^r \times \boldsymbol{a}_w^r , \; \boldsymbol{a}_v = J \, \boldsymbol{a}_w^r \times \boldsymbol{a}_u^r , \text{ and } \boldsymbol{a}_w = J \, \boldsymbol{a}_u^r \times \boldsymbol{a}_v^r . \tag{53}$$

For the later convenience, we introduce vectors $\boldsymbol{a}''$ defined as

$$\boldsymbol{a}_{q_i}'' = J \boldsymbol{a}_{q_i}^r , \tag{54}$$

or explicitly

$$\boldsymbol{a}_u'' = \boldsymbol{a}_v \times \boldsymbol{a}_w , \; \boldsymbol{a}_v'' = \boldsymbol{a}_w \times \boldsymbol{a}_u , \text{ and } \boldsymbol{a}_w'' = \boldsymbol{a}_u \times \boldsymbol{a}_v , \tag{55}$$

which are also denoted as surface-Jacobians J_{sq_i} for the surfaces defined by $q_i = const$, in other words,

$$a''_{q_i} = J_{sq_i} .$$

(56)

A vector function $\mathbf{F}$ can be expressed in terms of either the reciprocal unitary vectors, or the unitary vectors as

$$\mathbf{F} = f_u \mathbf{a}^r_u + f_v \mathbf{a}^r_v + f_w \mathbf{a}^r_w = g_u \mathbf{a}_u + g_v \mathbf{a}_v + g_w \mathbf{a}_w ,$$

(57)

the first expression being convenient for the representation of fields and the second for the representation of currents. Employing relation (52), we find that

$$f_u = \mathbf{F} \cdot \mathbf{a}_u , \ f_v = \mathbf{F} \cdot \mathbf{a}_v , \ f_w = \mathbf{F} \cdot \mathbf{a}_w , \ \text{and}$$

(58)

$$g_u = \mathbf{F} \cdot \mathbf{a}^r_u , \ g_v = \mathbf{F} \cdot \mathbf{a}^r_v , \ g_w = \mathbf{F} \cdot \mathbf{a}^r_w .$$

(59)

Finally, it can be shown [73] that the gradient of the scalar function f is found as

$$\nabla f = \sum_{i=1}^{3} \mathbf{a}^r_{q_i} \frac{\partial f}{\partial q_i} = \mathbf{a}^r_u \frac{\partial f}{\partial u} + \mathbf{a}^r_v \frac{\partial f}{\partial v} + \mathbf{a}^r_w \frac{\partial f}{\partial w} ,$$

(60)

the divergence of the vector function $\mathbf{F}$ is found as

$$\nabla \cdot \mathbf{F} = \sum_{i=1}^{3} \mathbf{a}^r_{q_i} \cdot \frac{\partial \mathbf{F}}{\partial q_i} = \frac{\partial \mathbf{F}}{\partial u} \cdot \mathbf{a}^r_u + \frac{\partial \mathbf{F}}{\partial v} \cdot \mathbf{a}^r_v + \frac{\partial \mathbf{F}}{\partial w} \cdot \mathbf{a}^r_w = ,$$
$$= \frac{1}{J} \left[\frac{\partial (J \, g_u)}{\partial u} + \frac{\partial (J \, g_v)}{\partial v} + \frac{\partial (J \, g_w)}{\partial w} \right]$$

(61)

and the curl of the vector function $\mathbf{F}$ is found as

$$\nabla \times \mathbf{F} = \sum_{i=1}^{3} \mathbf{a}^r_{q_i} \times \frac{\partial \mathbf{F}}{\partial q_i} = \frac{1}{J} \begin{vmatrix} \mathbf{a}_u & \mathbf{a}_v & \mathbf{a}_w \\ \partial/\partial u & \partial/\partial v & \partial/\partial w \\ f_u & f_v & f_w \end{vmatrix} .$$

(62)

3.3.3. Geometrical parameters of the generalized curvilinear hexahedron

Position vector for a point within any particular K-th order hexahedron with a priori given nodal points r_1, r_2, …, r_M is readily calculated by substituting (44) back into (41). Explicit analytical expressions for the first- and second-order elements become, respectively,

$$r(u,v,w) = \frac{1}{8}[-r_1\,(u-1)(v-1)(w-1) + r_2\,(u+1)(v-1)(w-1) + \ldots$$
$$+ r_8\,(u+1)(v+1)(w+1)], \tag{63}$$

and

$$r(u,v,w) = [-r_1\,u(1-u)v(1-v)w(1-w)/8 + \ldots + r_{27}\,u(1+u)v(1+v)w(1+w)/8]. \tag{64}$$

Analogous expressions are obtained for higher order hexahedra.

Unitary vectors a can be calculated by substituting (41) into (48), which yields

$$a_u = \sum_{i=1}^{M} r_i \frac{\partial \hat{L}_i^K}{\partial u}, \quad a_v = \sum_{i=1}^{M} r_i \frac{\partial \hat{L}_i^K}{\partial v}, \text{ and } a_w = \sum_{i=1}^{M} r_i \frac{\partial \hat{L}_i^K}{\partial w}. \tag{65}$$

Derivative of the Lagrange-type polynomial $\partial \hat{L}_i^K / \partial u$ is found from (44)

$$\frac{\partial \hat{L}_i^K}{\partial u} = \frac{\partial L_m^K(u)}{\partial u} L_n^K(v) L_l^K(w), \tag{66}$$

since L_n^K and L_l^K are independent of u. The derivative of the Lagrange polynomial L_m^K is easily found to be

$$\frac{\partial L_m^K(u)}{\partial u} = (\sum_{\substack{j=0 \\ j \neq m}}^{K} \frac{1}{u - u_j}) L_m^K(u), \tag{67}$$

and finally we obtain

$$\frac{\partial \hat{L}_i^K}{\partial u} = (\sum_{\substack{j=0 \\ j \neq m}}^{K} \frac{1}{u - u_j}) L_m^K(u) L_n^K(v) L_l^K(w), \tag{68}$$

with analogous expressions for the derivatives with respect to v and w.

Jacobian J, reciprocal unitary vectors $\boldsymbol{a}^r$ and vectors $\boldsymbol{a}''$ can readily be calculated from (50), (51) and (55), respectively, by applying the designated vector multiplications.

Finally, we remark that all vectors are internally expressed by their global Cartesian components, i.e., $\boldsymbol{r}_i = (x_i, y_i, z_i)$, $\boldsymbol{a} = (a_x, a_y, a_z)$, and $\boldsymbol{a}^r = (a_x^r, a_y^r, a_z^r)$, etc., and all algebraic vector manipulations (e.g., addition, scalar and vector multiplication) are carried out in the global Cartesian $x - y - z$ coordinate system. For instance, we have

$$\boldsymbol{r}_i + \boldsymbol{r}_j = (x_i + x_j, y_i + y_j, z_i + z_j), \tag{69}$$

$$\boldsymbol{a}_u \cdot \boldsymbol{a}_v = (a_{u_x} a_{v_x} + a_{u_y} a_{v_y} + a_{u_z} a_{v_z}), \text{ and} \tag{70}$$

$$\boldsymbol{a}_u \times \boldsymbol{a}_v = \begin{vmatrix} \boldsymbol{i}_x & \boldsymbol{i}_y & \boldsymbol{i}_z \\ a_{u_x} & a_{u_y} & a_{u_z} \\ a_{v_x} & a_{v_y} & a_{v_z} \end{vmatrix}, \tag{71}$$

$\boldsymbol{i}_x$, $\boldsymbol{i}_y$ and $\boldsymbol{i}_z$ being the unit vectors of the global Cartesian $x - y - z$ coordinate system. Analogous expressions hold for all other vector combinations.

3.4. Special cases of generalized hexahedra

As mentioned in Section 3.2, control points of a generalized hexahedron can be arbitrarily positioned in space. However, when placed in a certain way, they can determine various distorted and/or highly irregular hexahedral shapes, some of which are illustrated in Fig. 3.6. These special cases are addressed in this Section.

The basic idea in adopting the generalized hexahedra for geometrical modeling, instead of simple elements, was to introduce more degrees of freedom (in the geometrical sense) into each element, thus making it more flexible and more convenient for large-domain geometrical approximations. However, the advantage of the newly introduced freedom has to be taken into consideration conservatively and cautiously, since the accuracy of the approximation of the unknown function, within each element, will depend on the element's geometrical properties. Generally speaking, the more regular the hexahedron – the better the approximation.
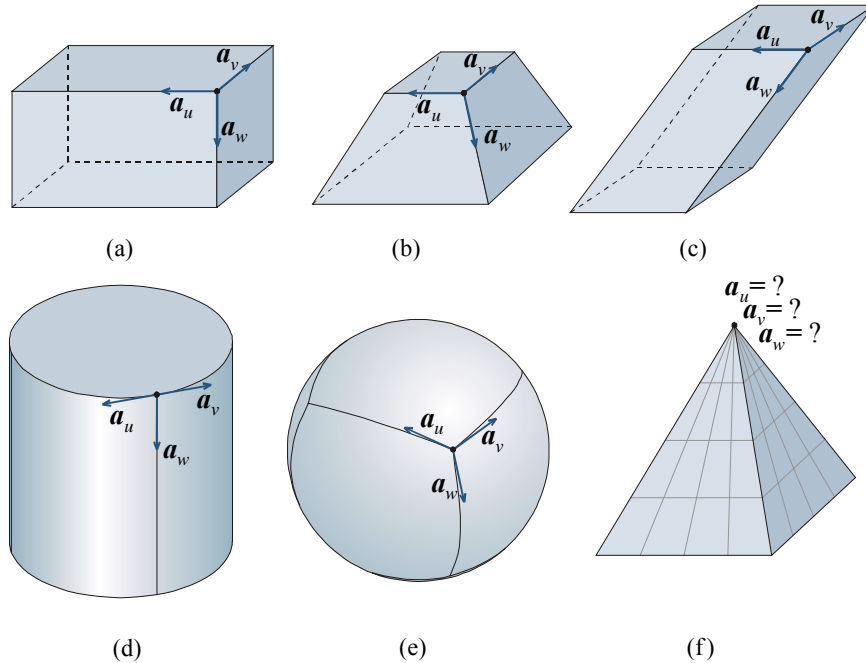
Fig. 3.6. Some special cases of the generalized curvilinear hexahedra;
(a) rectangular parallelepiped, (b) frustum of a pyramid, (c) oblique prism, (d) cylinder, (e) sphere and (f) pyramid.

To better understand this claim, consider the equations (50)-(57). In our problem, the unknown vector function is the electric field E, and its convenient general representation within each element is the one involving the reciprocal unitary vectors [e.g., the first representation shown in (57)], hence we write

$$E = f_u \boldsymbol{a}_u^r + f_v \boldsymbol{a}_v^r + f_w \boldsymbol{a}_w^r, \tag{72}$$

where the scalar functions f_u, f_v and f_w are of no significant importance at the moment and can be considered as linear combinations of specific known functions. Obviously, the accuracy of the given representation will depend on the accuracy of reciprocal unitary vectors $\boldsymbol{a}_{q_i}^r$ $(i = 1, 2, 3)$, and on their ability to span the 3-D space completely, so that all components of the field can be properly taken into account. Mathematically ideal case is when the unitary vectors $\boldsymbol{a}_{q_i}$ $(i = 1, 2, 3)$ are mutually perpendicular, i.e., when generalized hexahedron reduces to a rectangular parallelepiped (a brick), as shown in Fig. 3.6(a). In this case, the reciprocal unitary vectors are also mutually perpendicular, all three possible components of the field can be represented correctly, and the Jacobian can be calculated precisely. As the angles between the unitary vectors shift from $90°$, towards either $0°$ or $180°$, this being the case in all other examples shown in Fig. 3.6(b)-(f), the situation changes and becomes mathematically more and more difficult as this shift is more pronounced.

Particularly inconvenient is the case when the angle between the unitary vectors, say vector $\boldsymbol{a}_u$ and vector $\boldsymbol{a}_v$, comes extremely close to $0°$ or $180°$ [e.g., in Fig. 3.6(d)]. Firstly, field components tangential to the circle, i.e., in the direction of $\boldsymbol{a}_u$ and $\boldsymbol{a}_v$ in Fig. 3.6(d), cannot be correctly modeled since both $\boldsymbol{a}_u''$ and $\boldsymbol{a}_v''$ will point in the radial direction (perpendicular to the circle). Secondly, the cross-product $\boldsymbol{a}_u \times \boldsymbol{a}_v$ will become infinitely small thus vanishing the Jacobian, which will, theoretically, make the reciprocal vectors either singular or indeterminate, and, numerically, extremely inaccurate and hard to compute.

Another important example is the case shown in Fig. 3.6(e), i.e., when the hexahedron is deformed in such a way that unitary vectors become almost coplanar. In this case, all three vectors a''_u, a''_v and a''_w will point in the radial direction (perpendicular to the spherical surface), making it very hard to properly approximate the field components tangential to the spherical surface. The cross-product $a_u \times a_v$ remains finite in this case, however, the Jacobian will still vanish due to its mixed-product nature, again making the reciprocal vectors singular and, computationally cumbersome.

Additional type of severe geometrical distortion, which also leads to numerical problems in the approximation of the fields, occurs if the control points are placed in a way that collapses one (or more) of the hexahedron's edges [e.g., in Fig. 3.6(f)]. In this case the density of the coordinate lines becomes infinitely large, and the field representation shown in (72) cannot be adopted.

It is very hard to predict the actual impact of the degree of element's geometrical deformity on the overall accuracy of the field representation and on the final solution. This will obviously depend on the case under consideration, namely on the particular field distribution within the element and/or on the type and nature of the boundary conditions imposed on element's edges/sides. For instance, it has been shown that the tangential components of the fields are poorly represented in the case of a spherical surface. However, if the boundary condition imposed on the spherical surface is that of a PEC, the tangential components of the field will vanish anyway thus significantly diminishing the influence of the element's geometrical distortion, which itself is the most critical on the element's surface, and generally becomes less pronounced towards its interior. This said, a particularly special care has to be taken when higher order elements are used, since they require the placement of control points throughout their volume as well. These control points guide the coordinate lines in the element's interior and can initiate unnecessary numerical problems if not properly placed. Namely, when modeling a given structure, from the geometrical point of view it is

only required that the elements' faces (sides) conform as close as possible to the surface they are approximating, whereas there are no explicit requirements imposed on the elements' interiors. Hence, the modeling of the element's interior is completely arbitrary and should be done in a way that minimizes the distortion of coordinate lines. Consider, for instance, a sphere approximated by a fourth order hexahedron. Placement of 127 control points, defining the fourth order hexahedron, can be done in an infinite number of ways, two of which are illustrated in Fig. 3.7(a) and (b). In both cases, the explicit placement of control points in the plane designated by $w = 0$ is shown, together with the corresponding piecewise approximation of u and v coordinate lines. In both models the control points on the element's faces are placed in the identical way. The inner points, however, define an inscribed sphere in the first model, shown in Fig. 3.7(a), and an inscribed cube in the second, shown in Fig. 3.7(b). As seen, in the first model the coordinate lines are much more severely distorted (note particularly the angle between the vectors $\boldsymbol{a}_u$ and $\boldsymbol{a}_v$ at the shown node), whereas in the second they are kept almost orthogonal (this being the ideal case) throughout the greater part of the element's interior.

Luckily, if it is assessed that they can endanger the accuracy of the solution, all potentially ill situations can easily be avoided by using multiple-element approximations, instead of single-element ones, some of which are shown in Fig. 3.8(a)-(c). To avoid confusion, instead of a multi-element model of a pyramid, shown in Fig. 3.8(c) is a 2-D multi-element model of a triangle. The corresponding 3-D model of a pyramid can be obtained similarly. Naturally, multiple-element models are not exactly "in-line" with the large-domain modeling philosophy, and should be used only as a compromise in situations that would make such models more optimal.
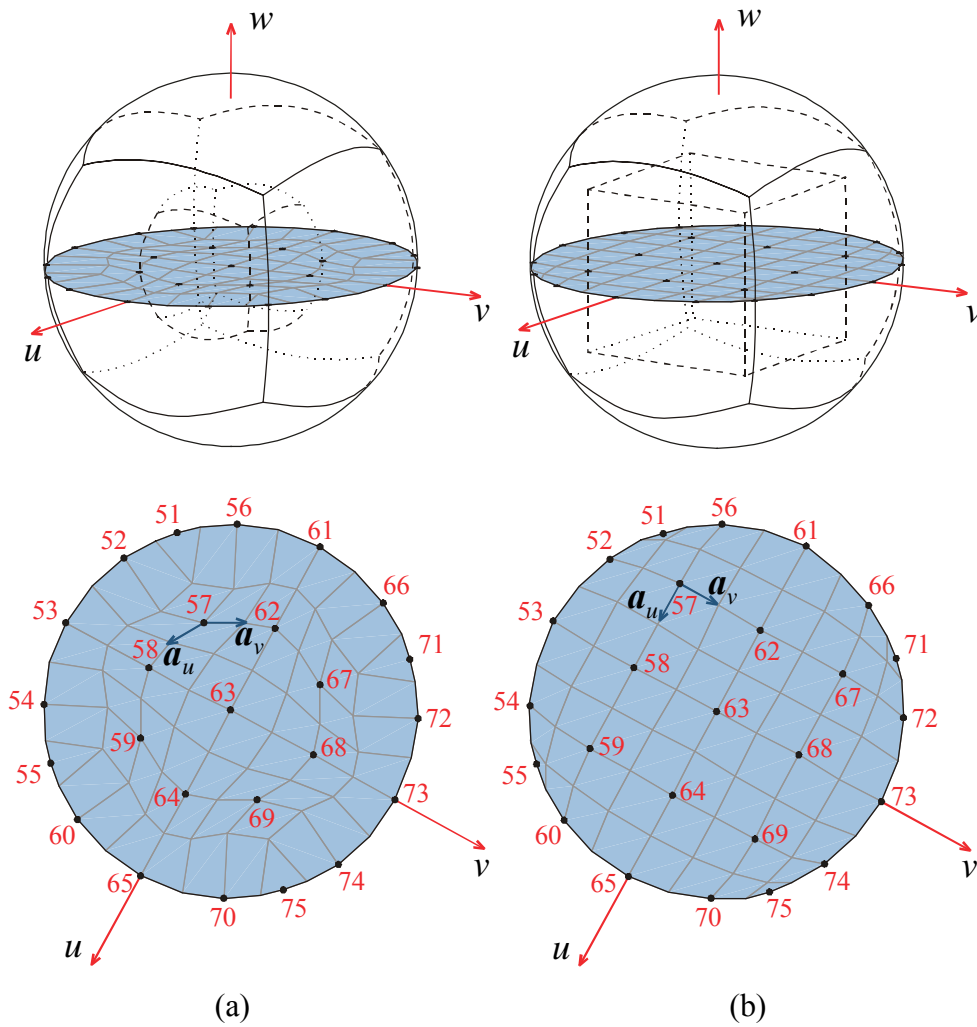
Fig. 3.7. Two examples of the single-hexahedron fourth order model of a sphere with the inner control points belonging to an inscribed (a) sphere and (b) cube.

To conclude, it would be hard to construct an optimal model in all possible situations. It can be intuitively clear, however, that the following three rules could lead to more accurate field approximations within each element, and should thus be followed whenever possible. The control points of a generalized hexahedron should be placed so as

- to keep the coordinate lines mutually as perpendicular as possible,

- to keep the density of the coordinate lines within the element as constant as possible, and

- to guide the coordinate lines in the way that would make one of the reciprocal unitary vectors conformal with the anticipated field distribution (tangential to the electric field force lines).

Additional rules and comments pertaining to the multiple-element geometrical approximations are given in the following Section.

(a)   (b)   (c)
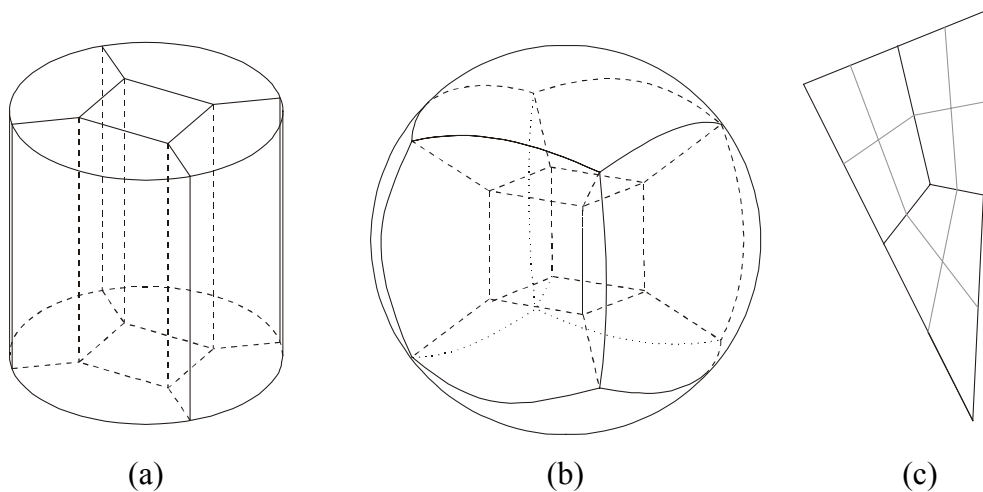
Fig. 3.8. Alternative, multiple-element, models of (a) a cylindrical domain, (b) a spherical domain, and (c) a triangular patch.

3.5.   General rules of spatial discretization using curved parametric hexahedra

The general procedure of spatial discretization in FEM is called *meshing*, and the resulting geometrical models (approximations) are thus called meshes. Meshing includes both, generation of global points (mesh nodes) and association of particular nodes with control points of the corresponding finite elements.

The rules of spatial discretization (meshing rules) set forth in this Section are based on the geometrical properties of the adopted basic element (generalized hexahedron), and on the mathematical properties of the weak-form integral formulation for the chosen boundary-value problem and its FE discretization, while simultaneously having in mind the adopted large-domain modeling philosophy and particular set of basis functions introduced in the following Chapter.

The structure under consideration should be first divided into homogeneous or continuously inhomogeneous domains. Each of thus obtained domains should be then geometrically approximated by the number of generalized curved parametric hexahedra. The control points of each hexahedron should be chosen according to the rules described in the previous Section. The orders of the hexahedra are arbitrary and any two hexahedra can share common points along the edges or faces (regardless of their order), provided the same magnitudes of local parametric representations associated with the shared points are ensured. In other words, if the elements e_m and e_n share common points, and the local coordinates of any of the shared points are denoted by an unordered set $\{u,v,w\}^{e_m}$ on the first element and as $\{u,v,w\}^{e_n}$ on the second, then the identity $\{u,v,w\}^{e_m} = \{\pm u, \pm v, \pm w\}^{e_n}$ has to be valid for all shared points. Typically, however, if hexahedra have common points, it should be either only a vertex, a whole edge, or a whole face. This reduces the possibility of errors and confusion in the modeling. Hexahedra can never share a volume domain. More details about the connection of hexahedra can be found in Chapter 4.

Edges and faces of the hexahedra associated with the outer boundary of the mesh and of the domain being approximated should conform as close as possible to the boundary shape. In order to achieve this, higher order elements should be used when appropriate, i.e., to approximate a curvature, and the first order elements should be used in all other cases, thus keeping the model as optimal as possible. The elements should be electrically as large as possible, provided the corresponding orders of the

field approximation are high enough to accurately approximate the field within the hexahedron, but should not exceed two wavelengths in any particular direction. Finally, all six sides (faces) of each hexahedron in the mesh should be either shared with the adjacent hexahedra in the mesh, or have a proper mesh-terminating boundary condition imposed upon them.

Meshing can be done either automatically, or manually. Automatic meshing procedures for 3-D EM applications have been developed for brick, triangular prism and tetrahedral cells, but no such general codes exist for complex curved hexahedral elements adopted here. A combined, partly manual – partly automatic, technique has been developed for the purpose of this thesis, and used to generate the meshes for the examples shown in Chapter 6. According to this procedure, the structure is initially meshed manually, using large elements that conform to the structure boundaries. This, extremely coarse, mesh is then automatically subdivided into smaller elements using a number of procedures, specifically developed for the segmentation of some typical geometrical shapes, such as bricks, spheres, cylinders, etc. The control points of higher order curved elements are obtained by meshing the appropriate rectangular parallelepiped and then projecting thus obtained points onto the curved surface a priori defined by its parametric equations. For the reasons given in Section 3.4, the inner points of higher order elements are kept on the originally defined parallelepiped.

Development of fully automatic meshing procedure for the generalized curved parametric tetrahedral cells is an extremely involving task and it is beyond the scope of this thesis.

3.6.   Conclusion

A class of highly flexible geometrical elements, generalized curved parametric hexahedra based on Lagrange-type interpolatory polynomials of arbitrary orders, have been described in this Section as basic elements for 3-D FEM domain tessellation.

Important mathematical formulas pertaining to the underlying GCS have been defined and calculation of all geometrical parameters has been carried out explicitly. Finally, some important guidelines regarding the construction of large-domain hexahedral meshes in general EM problems have been given.

Proposed curvilinear elements are much more flexible than the generally used simple elements in the form of bricks, tetrahedra and triangular prisms, and they allow highly efficient and accurate modeling of arbitrarily shaped domains, with or without curvature. Parametric bodies of higher $(K > 2)$ geometrical orders provide yet additional flexibility and accuracy in modeling of complex curved structures. This enables the utilization of large elements throughout the FEM mesh, which reduces the total number of elements comprising the mesh, and can extremely increase the overall efficiency of the FEM method by reducing the number of finally generated unknowns.

Up to this point, neither the construction of finite elements on the adopted geometrical elements, nor the expansion of an unknown function have yet been discussed. It is clearly understood, however, that since the unknown function is expressed in terms of the parameters of the basic geometrical elements, as in (57), computational intensity of function evaluation greatly depends on the mathematical complexity of the underlying geometrical element. The more complex the element − the harder it is to compute the necessary parameters (r, a, J, etc.) and evaluate the function at a given point. This computational burden negatively affects both machine storage capacity and processing time. Additionally, as the element order is increased, the complexity of necessary calculations for the curved parametric hexahedra increases quickly [see, for instance, equations (63) and (64)], and finally the generation of the nodal points becomes more and more complicated and more demanding in terms of storage.

One can easily appreciate that parameters of the simple elements (e.g., bricks and tetrahedra) are, not only fairly easy to compute, but also are they constant throughout the element volume, which is not the case with the generalized curved hexahedra. The

latter fact may seriously jeopardize the effectiveness of the higher order curved elements and limit their applicability in some situations (e.g., employment of the second order ABC). On the other hand, most of the problems associated with the computational intensity could be worked around in the implementation process. As it will be shown in Chapter 4, geometrical parameters need to be computed only at certain, a priori known, points, hence they could be evaluated only once and then conveniently stored for the future easy access by the successive function calls.

To summarize, generalized interpolatory hexahedral parametric elements indeed offer significantly improved flexibility (over the, widely used, simple elements) necessary for the efficient large-domain modeling of complex structures, although they do require a considerable care in the implementation (programming) phase. In order to take full advantage of the higher order elements, it is important that they can be made electrically large. In the modeling of realistic structures, it is also very important that the elements of different shapes, sizes and geometrical orders can be combined together, thus allowing the construction of the fully optimal geometrical meshes. If both of these requirements are to be satisfied, implementation of hierarchical-type higher order polynomial basis functions for the approximation of fields is the right choice, and it will be discussed in the following Chapter.

4. CURL-CONFORMING POLYNOMIAL VECTOR BASIS FUNCTIONS; HIGHER ORDER CURVED HEXAHEDRAL VECTOR FINITE ELEMENTS

4.1. Introduction

The earliest finite elements were scalar (node-based), having the values of the scalar field (e.g., scalar potential) at the element nodes as unknown parameters. In vector problems, scalar elements were also used, only this time each node had three unknowns instead of one (one for each vector component in a 3-D model). Vector elements (edge elements), on the other hand, are finite elements whose degrees of freedom (unknowns) are associated with edges (or more generally surfaces or volume) of the element, rather than with the element nodes. They have several useful properties: they allow the normal component of the vector to be discontinuous from one element to the next; they are better at handling field singularities; they eliminate spurious solutions [18] known to be existing in the FEM solutions based on node-based FEs. Due to described qualities, vector finite elements represent a logical choice in modern FEM modeling of vector problems.

Depending on the problem, divergence-conforming (e.g., in current-based problems) or curl-conforming (e.g., in field-based problems) vector elements (also known as tangential vector finite elements, or TVFEs) are used [37]. Neither divergence-conforming nor curl-conforming elements impose the complete continuity

of the vector variable across interfaces between adjacent cells in the mesh. Instead, they respectively ensure only normal or tangential continuity, hence the corresponding approximation is differentiable only in the sense of the divergence or curl operation. The term conforming is then used to denote the fact that the normal/tangential component of the vector variable is continuous across element faces, which is a condition required to define the divergence/curl of the vector variable. For the purpose of discretizing the electric-field wave equation (double-curl differential equation) by means of the vector finite elements, curl-conforming elements represent the natural choice.

Several different types of basis functions (e.g., exponential, harmonic, spline, as well as wavelet-like basis functions [44,45]) have been used historically in the FEM modeling. However, polynomial functions appear to be the most commonly used type of basis functions, although generally in the form of only piecewise-constant or piecewise-linear functions, and rarely in their higher order forms.

Higher order polynomial vector elements, recently investigated in FEM, are either of interpolatory [37,38] or hierarchical [39,40] form. Interpolatory bases generally have a greater degree of independence then so-called *nodeless bases*; thus they can potentially reduce a cause of ill-conditioning in higher order schemes [37]. On the other hand, the advantage of hierarchical elements is that they allow elements of different orders to be incorporated into the same mesh without any loss of tangential continuity (since each member of the hierarchical set incorporates the basis functions of the lower members, and adds basis functions of higher order) [18]. This quality of hierarchical elements is very important, allowing enhanced accuracy to be applied at certain regions (e.g., where field behavior is expected to be more abrupt) by increasing the order of the corresponding elements only (*p*-refinement), without the necessity to refine the geometrical mesh (*h*-refinement), which is computationally more expensive.

The latter quality being more appealing for the large-domain modeling approach, a set of hierarchical vector basis functions for the electric field function expansion is developed and presented in the following Section.

4.2. Field approximation by means of the new hierarchical higher order polynomial curl-conforming vector basis functions

Electric field inside every hexahedron is initially approximated with the series

$$
\boldsymbol{E} = \sum_{i=0}^{N_u-1} \sum_{j=0}^{N_v} \sum_{k=0}^{N_w} \alpha_{uijk}\, \boldsymbol{f}_{uijk} + \sum_{i=0}^{N_u} \sum_{j=0}^{N_v-1} \sum_{k=0}^{N_w} \alpha_{vijk}\, \boldsymbol{f}_{vijk} +
$$
$$
+ \sum_{i=0}^{N_u} \sum_{j=0}^{N_v} \sum_{k=0}^{N_w-1} \alpha_{wijk}\, \boldsymbol{f}_{wijk} \;,
\tag{73}
$$

where $\boldsymbol{f}$ are curl-conforming hierarchical-type vector basis functions defined as

$$
\begin{aligned}
\boldsymbol{f}_{uijk} &= u^i P_j(v) P_k(w)\, \boldsymbol{a}_u^r = P_{uijk}\, \boldsymbol{a}_u^r \\
\boldsymbol{f}_{vijk} &= P_i(u)\, v^i P_k(w)\, \boldsymbol{a}_v^r = P_{vijk}\, \boldsymbol{a}_v^r \quad, \\
\boldsymbol{f}_{wijk} &= P_i(u) P_j(v)\, w^k \boldsymbol{a}_w^r = P_{wijk}\, \boldsymbol{a}_w^r
\end{aligned}
\tag{74}
$$

P are the polynomial functions defined as

$$
P_i(u) = \begin{cases} 1-u, & i=0 \\ u+1, & i=1 \\ u^i-1, & i\geq 2,\, \text{even} \\ u^i-u, & i\geq 3,\, \text{odd} \end{cases}, \qquad -1\leq u,v,w\leq 1,
\tag{75}
$$

N_u, N_v, and N_w are the adopted degrees of the polynomial approximation, which are entirely independent from the element geometrical order, K, and α_{uijk}, α_{vijk}, and α_{wijk} are unknown field-distribution coefficients. Note that the sum limits in (73) that correspond to the variations of a field component in the direction along that

component are by one smaller than the orders corresponding to the variations in other two parametric coordinates. This mixed-order arrangement is in accordance with the reduced-gradient criterion [14,15], which is a preferable choice for modeling of waveguiding structures and 3-D resonant cavities, where the use of complete functions may lead to spurious solutions and incorrect results. The reciprocal unitary vectors $\boldsymbol{a}^r$ are defined in (51).

Polynomial degrees in the field expansions can be high, so electrically large finite elements can be used. This greatly reduces the overall number of unknowns for a given problem and significantly enhances the accuracy and efficiency of the technique, as compared to traditionally used low-order basis functions. The field expansions automatically satisfy continuity boundary conditions for tangential fields on surfaces shared by adjacent hexahedra in the model leaving the normal field components unconstrained (curl-conforming functions). Note that similar higher order basis functions in the divergence-conforming form are used in conjunction with trilinear ($K = 1$) hexahedra for the large-domain (entire-domain) MoM solution to volume integral equations [4-7]. Special 1-D polynomial functions defined in (74) are shown in Fig. 4.1. for up to the fifth order. As seen from the figure, the first two functions, P_0 and P_1, are the classical roof-top functions, being the only ones capable of modeling the unknown function at the segment boundaries ($u = \pm 1$). The higher order functions (P_i, $i > 1$), all vanishing at the boundaries, can only increase the approximation accuracy within the segment. Appropriate 3-D polynomial functions, P_{uijk}, P_{vijk} and P_{wijk}, are constructed by utilizing the special 1-D polynomial functions in the directions in which the governing of the tangential fields at the element (generalized hexahedron) faces needs to be constrained to the convenient subset of basis functions and corresponding unknown coefficients, as it will be explained in Section 4.5, and a simple exponential function is used in the remaining direction. In order to give a better insight in thus constructed polynomial functions, shown in Fig. 4.2. is one of their 2-D representations, defined by equation

$$P_{uij} = u^i P_j(v), \qquad\qquad\qquad\qquad (76)$$

since the 3-D functions, P_{ijk}, are hard to represent graphically.
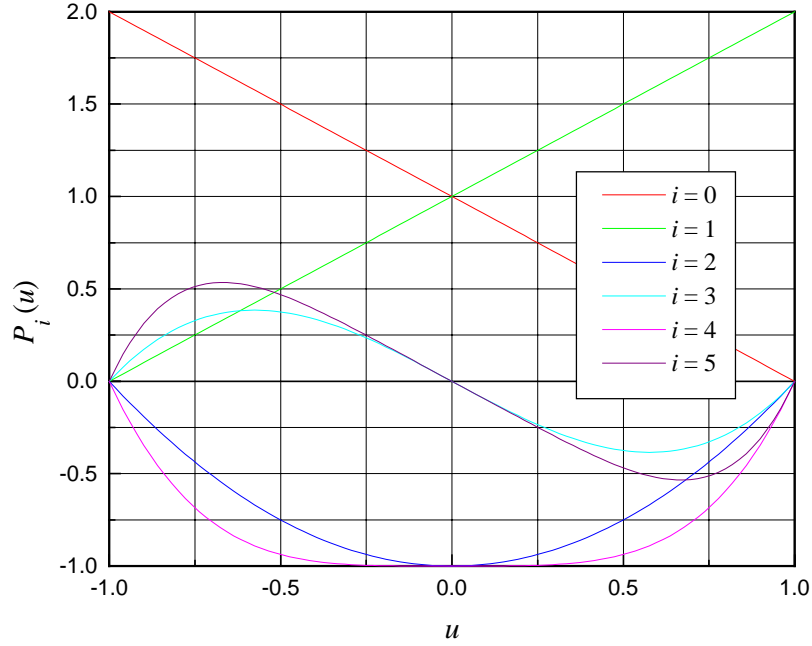
Fig. 4.1. Graphical representation of the 1-D polynomial functions defined by (75).

Polynomial functions P_i, P_{ij} and P_{ijk}, are hierarchical functions – each lower-order set of functions is a subset of all higher order sets. (Outlined in Fig. 4.2. are the first three reduced-gradient sets of orders $N_u = N_v = 1$, $N_u = N_v = 2$ and $N_u = N_v = 3$, respectively.) These functions enable using different orders of field approximation (e.g., from 1 to 10) in different elements, as well as in different directions within each element, which allows for a whole spectrum of element sizes (e.g., from a very small fraction of λ to a couple of λ) and shapes to be used in a simulation model. Hierarchical basis functions, on the other hand, generally have poor orthogonality properties, which results in FEM matrices with large condition numbers. It is known that, if the linear equations associated with the FEM are solved using iterative solvers, the solution procedures perform relatively poorly (require many iterations) when the

FEM matrices are badly conditioned. However, several approaches for improving the orthogonality of hierarchical higher order basis functions and the condition number of matrices in the context of both FEM and MoM have been proposed to cope with this problem [47,48,51-53].
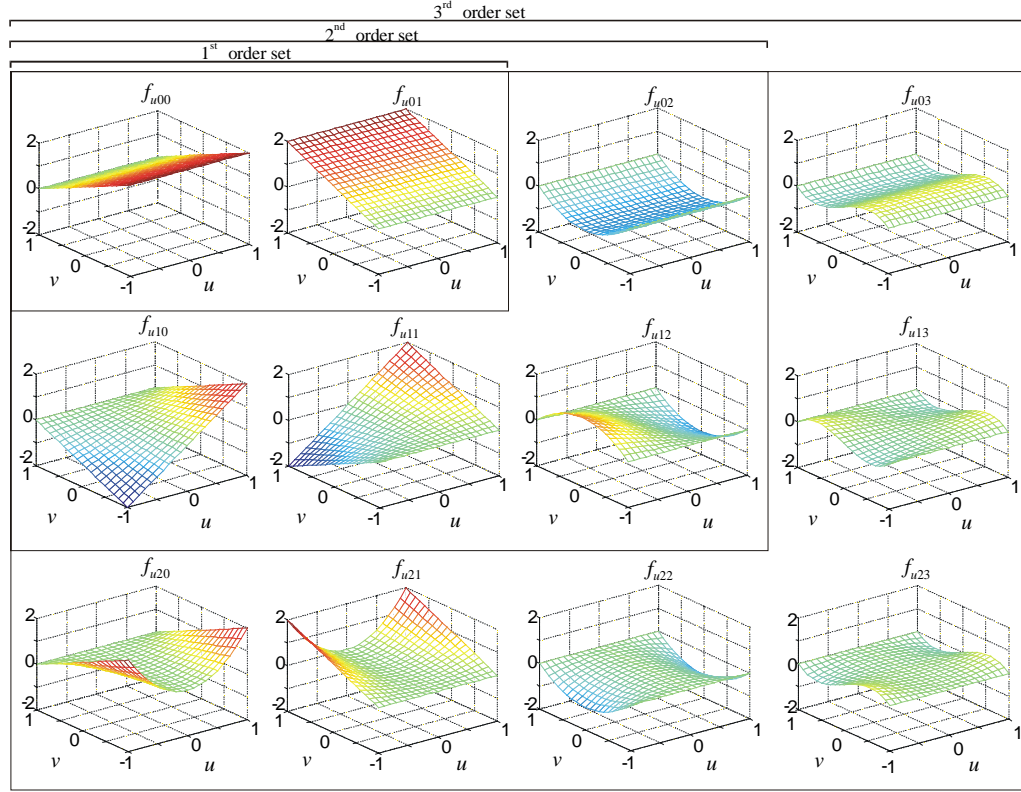
Fig. 4.2. Graphical representation of the 2-D polynomial functions defined by (76).

4.3. Discretization by finite elements

FEM discretization procedure with Galerkin-type testing, described in Section 2.5, can now be repeated using the proposed basis functions defined by (74)-(75). The corresponding weighted residual equations defined by (30) and written separately, for each element, are

$$\int_{V^e} \mu_r^{e^{-1}} (\nabla \times \boldsymbol{f}_{u\hat{i}\hat{j}\hat{k}}^e) \cdot (\nabla \times \boldsymbol{E}) \, dV - k_0^2 \int_{V^e} \varepsilon_r^e \boldsymbol{f}_{u\hat{i}\hat{j}\hat{k}}^e \cdot \boldsymbol{E} \, dV -$$

$$- \oint_{S^e} \mu_r^{e^{-1}} \boldsymbol{f}_{u\hat{i}\hat{j}\hat{k}}^e \times (\nabla \times \boldsymbol{E}) \cdot dS = 0$$

$$\hat{i} = 0,...,N_u^e - 1; \ \hat{j} = 0,...,N_v^e; \ \hat{k} = 0,...,N_w^e$$

$$\int_{V^e} \mu_r^{e^{-1}} (\nabla \times \boldsymbol{f}_{v\hat{i}\hat{j}\hat{k}}^e) \cdot (\nabla \times \boldsymbol{E}) \, dV - k_0^2 \int_{V^e} \varepsilon_r^e \boldsymbol{f}_{v\hat{i}\hat{j}\hat{k}}^e \cdot \boldsymbol{E} \, dV -$$

$$- \oint_{S^e} \mu_r^{e^{-1}} \boldsymbol{f}_{v\hat{i}\hat{j}\hat{k}}^e \times (\nabla \times \boldsymbol{E}) \cdot dS = 0$$

$$\hat{i} = 0,...,N_u^e; \ \hat{j} = 0,...,N_v^e - 1; \ \hat{k} = 0,...,N_w^e$$

$$\int_{V^e} \mu_r^{e^{-1}} (\nabla \times \boldsymbol{f}_{w\hat{i}\hat{j}\hat{k}}^e) \cdot (\nabla \times \boldsymbol{E}) \, dV - k_0^2 \int_{V^e} \varepsilon_r^e \boldsymbol{f}_{w\hat{i}\hat{j}\hat{k}}^e \cdot \boldsymbol{E} \, dV -$$

$$- \oint_{S^e} \mu_r^{e^{-1}} \boldsymbol{f}_{w\hat{i}\hat{j}\hat{k}}^e \times (\nabla \times \boldsymbol{E}) \cdot dS = 0$$

$$\hat{i} = 0,...,N_u^e; \ \hat{j} = 0,...,N_v^e; \ \hat{k} = 0,...,N_w^e - 1 \tag{77}$$

where testing indexes $\hat{i}$, $\hat{j}$ and $\hat{k}$ are introduced in order to be distinguishable from the expansion indexes i, j and k. Invoking Maxwell's first equation, (3), the surface-integrals in (77) can be represented as

$$G_{s\hat{i}\hat{j}\hat{k}}^e = jk_0\eta_0 \oint_{S^e} \boldsymbol{f}_{\hat{i}\hat{j}\hat{k}}^e \cdot (\boldsymbol{n} \times \boldsymbol{H}) \, dS \tag{78}$$

where η_0 is the free-space intrinsic impedance. It will be shown in Section 4.5 that this particular integral form provides a convenient numerical interface between the adjacent elements in the mesh. Substituting the field expansion given by (73) into (77) (volume-integrals only) and moving the surface-integrals to the right-hand side yields the following FEM matrix equation:

$$[K^e]\{\alpha^e\} = \{G_s^e\},\tag{79}$$

where

$$[K^e] = [A^e] - k_0^2[B^e].\tag{80}$$

Matrices $[A^e]$ and $[B^e]$ are given by

$$[A^e] = \begin{bmatrix} [UUA^e] & [UVA^e] & [UWA^e] \\ [VUA^e] & [VVA^e] & [VWA^e] \\ [WUA^e] & [WVA^e] & [WWA^e] \end{bmatrix}, \quad [B^e] = \begin{bmatrix} [UUB^e] & [UVB^e] & [UWB^e] \\ [VUB^e] & [VVB^e] & [VWB^e] \\ [WUB^e] & [WVB^e] & [WWB^e] \end{bmatrix}, \tag{81}$$

where the elements of the corresponding submatrices have the form

$$UUA^e_{\hat{i}\hat{j}\hat{k}ijk} = \int_{V^e} {\mu_r^e}^{-1} (\nabla \times \boldsymbol{f}^e_{u\hat{i}\hat{j}\hat{k}}) \cdot (\nabla \times \boldsymbol{f}^e_{uijk})\, \mathrm{d}V ,$$

$$UVA^e_{\hat{i}\hat{j}\hat{k}ijk} = \int_{V^e} {\mu_r^e}^{-1} (\nabla \times \boldsymbol{f}^e_{u\hat{i}\hat{j}\hat{k}}) \cdot (\nabla \times \boldsymbol{f}^e_{vijk})\, \mathrm{d}V , \tag{82}$$

$$UUB^e_{\hat{i}\hat{j}\hat{k}ijk} = \int_{V^e} \varepsilon_r^e \boldsymbol{f}^e_{u\hat{i}\hat{j}\hat{k}} \cdot \boldsymbol{f}^e_{uijk}\, \mathrm{d}V ,$$

$$UVB^e_{\hat{i}\hat{j}\hat{k}ijk} = \int_{V^e} \varepsilon_r^e \boldsymbol{f}^e_{u\hat{i}\hat{j}\hat{k}} \cdot \boldsymbol{f}^e_{vijk}\, \mathrm{d}V , \tag{83}$$

with analogous expressions for the elements of other submatrices of $[A^e]$ and $[B^e]$. Vector $\{\alpha^e\}$ is the column vector of unknown field-distribution coefficients,

$$\{\alpha^e\} = \begin{bmatrix} \{\alpha^e_{uijk}\} \\ \{\alpha^e_{vijk}\} \\ \{\alpha^e_{wijk}\} \end{bmatrix}. \tag{84}$$

4.4. Evaluation of the volume-integrals

Evaluation of the stiffness elements in (82) primarily requires the evaluation of the curls of basis functions whereas the mass elements in (83) can readily be evaluated in their present form. The curls of basis functions can be evaluated according to (62) which, applied to the expansion functions in (74), yields

$$\nabla \times \boldsymbol{f}_{uijk} = \frac{1}{J}[u^i P_j(v)\dot{P}_k(w)\boldsymbol{a}_v - u^i \dot{P}_j(v)P_k(w)\boldsymbol{a}_w] = \frac{1}{J}[P_{uij\dot{k}}\,\boldsymbol{a}_v - P_{ui\dot{j}k}\,\boldsymbol{a}_w]$$

$$\nabla \times \boldsymbol{f}_{vijk} = \frac{1}{J}[\dot{P}_i(u)\,v^j P_k(w)\boldsymbol{a}_w - P_i(u)\,v^j \dot{P}_k(w)\boldsymbol{a}_u] = \frac{1}{J}[P_{vij\dot{k}}\,\boldsymbol{a}_w - P_{\dot{v}ijk}\,\boldsymbol{a}_u]\ ,$$

$$\nabla \times \boldsymbol{f}_{wijk} = \frac{1}{J}[P_i(u)\dot{P}_j(v)\,w^k\,\boldsymbol{a}_u - \dot{P}_i(u)P_j(v)\,w^k\,\boldsymbol{a}_v] = \frac{1}{J}[P_{wi\dot{j}k}\,\boldsymbol{a}_u - P_{\dot{u}ijk}\,\boldsymbol{a}_v]$$

$$(85)$$

where dots denote the first derivatives. The derivatives of polynomial functions are easily found from (75) to be

$$\dot{P}_i(u) = \frac{\partial P_i}{\partial u} = \begin{cases} -1, & i=0 \\ 1, & i=1 \\ i\,u^{i-1}, & i\geq 2,\,\text{even} \\ i\,u^{i-1}-1, & i\geq 3,\,\text{odd} \end{cases}, \qquad -1\leq u,v,w\leq 1. \qquad (86)$$

and they are also known polynomial functions. Both volume integral types, stiffness and mass, can thus be reduced into the following integral over the generalized hexahedron:

$$\int_V \gamma_{\varepsilon\mu}(u,v,w)\,Pol_1(u,v,w)\,Pol_2(u,v,w)\,\boldsymbol{a}_1(u,v,w)\cdot\boldsymbol{a}_2(u,v,w)\,\mathrm{d}V\ , \qquad (87)$$

where $\gamma_{\varepsilon\mu}$ stands for any of the functions describing the medium within the element, ε_r or μ_r^{-1}, Pol stands for any of the known polynomial functions or its derivatives and $\boldsymbol{a}$ stands for any of the reciprocal or primary unitary vectors appearing in

definitions of the vector basis functions (74) and their curls (85) , respectively. The complete expression appearing under the integral in (87) reduces to a scalar function $f(u,v,w)$, once the dot-product of the unitary/reciprocal unitary vectors is computed, as shown in (70).

All integrals over the volume of a generalized hexahedron are actually integrated over the parent cube element (see Fig. 3.3.), in the $u-v-w$ domain, as

$$\int_V f(u,v,w)\,\mathrm{d}V = \int\int\int_{uvw} f(u,v,w)\,J(u,v,w)\,\mathrm{d}u\mathrm{d}v\mathrm{d}w, \qquad -1 \le u,v,w \le 1, \qquad (88)$$

where J stands for the Jacobian of the mapping defined by (50). If simple elements (e.g., tetrahedra, bricks, or triangular prisms) are used, both unitary/reciprocal unitary vectors and Jacobians are constant, as explained in Section 2.6, hence all volume-integrals could be calculated analytically, provided that the medium descriptor function $\gamma_{\varepsilon\mu}$ is constant or analytically integrable. However, this not being the case for the generalized hexahedra, numerical integration scheme has to be employed. The integration is thus carried out using the Gauss-Legendre threefold integration formula in $N_u^{\mathrm{GL}} \times N_v^{\mathrm{GL}} \times N_w^{\mathrm{GL}}$ points, i.e.,

$$\int_{u=-1}^{1}\int_{v=-1}^{1}\int_{w=-1}^{1} q(u,v,w)\,\mathrm{d}u\mathrm{d}v\mathrm{d}w = \sum_{m=1}^{N_u^{\mathrm{GL}}} W_m^u \sum_{n=1}^{N_v^{\mathrm{GL}}} W_n^v \sum_{l=1}^{N_w^{\mathrm{GL}}} W_l^w\, q(u_m,v_n,w_l) \qquad (89)$$

$q(u,v,w)$ being an arbitrary scalar function, and u_m, v_n and w_l, and W_m^u, W_n^v and W_l^w being, respectively, the integration points and corresponding weighting coefficients defined on a –1 to 1 interval.

Consider, for example, one of the stiffness-matrix elements (e.g., $UVA^e_{\hat{i}\hat{j}\hat{k}ijk}$), and one of the mass-matrix elements (e.g., $UVB^e_{\hat{i}\hat{j}\hat{k}ijk}$), which can be evaluated as:

$$UVA^e_{i\hat{j}\hat{k}ijk} = \int\limits_{V^e} \mu_r^{-1}(\nabla\times\boldsymbol{f}_{ui\hat{j}\hat{k}})\cdot(\nabla\times\boldsymbol{f}_{vijk})\,dV =$$

$$= \int\limits_{u=-1}^{1}\int\limits_{v=-1}^{1}\int\limits_{w=-1}^{1} \mu_r^{-1}\frac{1}{J}\underbrace{[P_{ui\hat{j}\hat{k}}\,\boldsymbol{a}_v - P_{ui\hat{j}\hat{k}}\,\boldsymbol{a}_w]}_{Pol_1\,\boldsymbol{a}_1}\cdot\frac{1}{J}\underbrace{[P_{vijk}\,\boldsymbol{a}_w - P_{vijk}\,\boldsymbol{a}_u]}_{Pol_2\,\boldsymbol{a}_2}\,J\,dudvdw=$$

$$= \sum\limits_{m=1}^{N_u^{GL}} W_m^u \sum\limits_{n=1}^{N_v^{GL}} W_n^v \sum\limits_{l=1}^{N_w^{GL}} W_l^w \left[\mu_r^{-1}\,Pol_1\,Pol_2\,(a_{1_x} a_{2_x} + a_{1_y} a_{2_y} + a_{1_z} a_{2_z})\frac{1}{J} \right]_{u_m,v_n,w_l},$$

$$(90)$$

and

$$UVB^e_{i\hat{j}\hat{k}ijk} = \int\limits_{V^e} \varepsilon_r \boldsymbol{f}_{ui\hat{j}\hat{k}}\cdot\boldsymbol{f}_{vijk}\,dV = \int\limits_{V^e} \varepsilon_r\,P_{ui\hat{j}\hat{k}}\,P_{vijk}\,\boldsymbol{a}_u^r\cdot\boldsymbol{a}_v^r\,dV =$$

$$= \int\limits_{u=-1}^{1}\int\limits_{v=-1}^{1}\int\limits_{w=-1}^{1} \varepsilon_r\,P_{ui\hat{j}\hat{k}}\,P_{vijk}\,\frac{\boldsymbol{a}_u''}{J}\cdot\frac{\boldsymbol{a}_v''}{J}\,J\,dudvdw=$$

$$= \sum\limits_{m=1}^{N_u^{GL}} W_m^u \sum\limits_{n=1}^{N_v^{GL}} W_n^v \sum\limits_{l=1}^{N_w^{GL}} W_l^w \left[\varepsilon_r\,P_{ui\hat{j}\hat{k}}\,P_{vijk}\,(a_{u_x}'' a_{v_x}'' + a_{u_y}'' a_{v_y}'' + a_{u_z}'' a_{v_z}'')\frac{1}{J} \right]_{u_m,v_n,w_l},$$

$$(91)$$

where the superscript e has been dropped in order to simplify the expressions. All other elements of matrices $[A^e]$ and $[B^e]$ are evaluated similarly.

Numbers of points for the Gauss-Legendre integration, N_u^{GL}, N_v^{GL} and N_w^{GL}, can be chosen arbitrarily. They can be small for the low-order polynomial field approximations and should be larger for the higher order approximations in the corresponding directions. A relatively large number of points, i.e., $(10 + N_u) \times (10 + N_v) \times (10 + N_w)$, was used in all of the numerical examples given in Chapter 6 (although integration formulas of lower orders could also have been used).

It is easily understandable that computations of the volume-integrals, involving a significant number of operations and function evaluations due to threefold summation process, can be time-wise extremely expensive, especially for the higher order field expansions. As such, they represent one of the most critical computational bottlenecks (the second being the FEM matrix inversion), and should be encoded with considerable care. Note that, for each element, polynomial functions, medium descriptor function, unitary/reciprocal unitary vectors and Jacobian need be evaluated only at the specific points, u_m, v_n and w_l, ($m = 1,...,N_u^{\mathrm{GL}}$; $n = 1,...,N_v^{\mathrm{GL}}$; $l = 1,...,N_w^{\mathrm{GL}}$) defined by the Gauss-Legendre integration formula. Integration points are a priori known for each element, hence it is convenient to evaluate all these functions, including all orders of the polynomial functions P_{ijk} and their derivatives, before entering the summation loops, and store them in easily accessible lookup tables, thus avoiding the numerous and expensive function calls within the summation loops.

To illustrate the proposed idea, consider the function u^i, which has to be evaluated in all points u_m ($m = 1,...,N_u^{\mathrm{GL}}$), and for all i ($i = 0,...,N_u - 1$). The corresponding lookup table can be generated using the simple algorithm shown in Fig. 4.3, whereas all other functions can be evaluated in the similar fashion. (Geometrical parameters are calculated as explained in Section 3.3.3.) The stored values are then used as needed in the summation process, instead of evaluating them each time by a function call. This procedure, according to author's experience, reduces the FEM matrix filling time by at least 50%, as compared to the non-optimized evaluation of volume-integrals (which involves separate function calls).

```
                    ┌─────────────┐
                    │    START    │
                    └─────────────┘
                           │
        ┌──────────────────▼──────────────────┐
        │              m = 1, N_u^GL           │
        │      ┌───────────────────────┐        │
        └─────►│         (box)          │
```

$$m = 1, N_u^{\mathrm{GL}}$$

$$\mathrm{utoi}_m^0 = 1$$

$$\mathrm{utoi}_m^1 = u_m$$

$$i = 2, N_u$$

$$\mathrm{utoi}_m^i = \mathrm{utoi}_m^{i-1} \cdot u_m$$

STOP
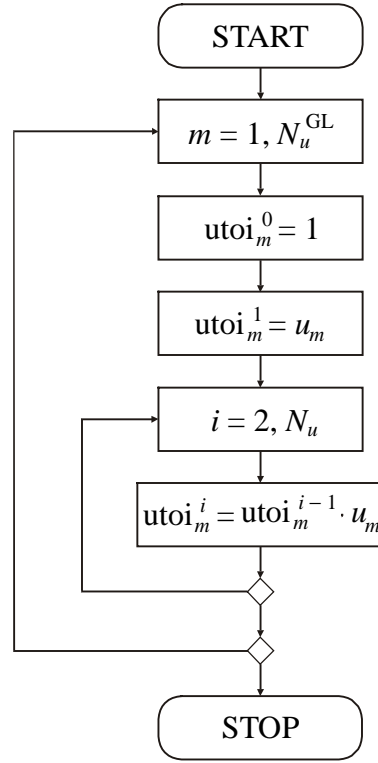
Fig. 4.3. Evaluation of the polynomial function u^i and generation of the corresponding lookup table.

Finally, we remark that both volume integral types, stiffness and mass, can be complex or real depending, respectively, on medium parameters μ_r and ε_r, or rather on the type of the medium occupying the element under consideration. In most cases, however, μ_r is a real function, whereas $\varepsilon_r = \varepsilon_r' - j\sigma/\omega\varepsilon_0$ is real for lossless and complex for lossy media. Note that in this typical scenario, matrices $[A^e]$ are frequency independent, whereas matrices $[B^e]$, are frequency independent if the medium is lossless. If medium parameters are constant functions in all elements comprising the mesh, or they are frequency independent, the multifrequency FEM analysis of the same EM problem (which is very often required) can be optimized so that the FEM matrix elements (volume-integrals) are calculated only once, stored in a convenient form, and then used as many times as needed in conjunction with different,

frequency dependent, excitation matrices. This way, the overall analysis time can be significantly reduced, since very expensive volume integrations are performed only once, allowing the rest of the time to be spent only on matrix inversions at different frequencies. The reduction of computational time, however, comes at the price of increasing the load on the computational storage resources, as it will be explained in Section 5.3. The opportunity of optimizing the analysis in this particular fashion does not arise when integral equation numerical techniques (e.g., MoM) are used, due to frequency dependence of matrix elements inherited from the Green's function.

4.5.   Assembly of the global system of equations

Assembly of the global system of equations is done by expanding the local element matrices with zeros, as explained in Section 2.5, and adding them, as shown in (40). Thus obtained, so-called *disconnected system*, results in a sparse FEM matrix with the elemental submatrices on the main diagonal. The system can be formally represented as

$$[K^{\text{dis}}] \cdot \{\alpha^{\text{dis}}\} = \{G_{\text{s}}^{\text{dis}}\}, \tag{92}$$

where the corresponding matrices are given by

$$[K^{\text{dis}}] = \begin{bmatrix} [K^1] & & & \\ & [K^2] & & \\ & & \ddots & \\ & & & [K^{N_{\text{e}}}] \end{bmatrix}, \quad \{\alpha^{\text{dis}}\} = \begin{bmatrix} \{\alpha^1\} \\ \{\alpha^2\} \\ \vdots \\ \{\alpha^{N_{\text{e}}}\} \end{bmatrix}, \quad \{G^{\text{dis}}\} = \begin{bmatrix} \{G_{\text{s}}^1\} \\ \{G_{\text{s}}^2\} \\ \vdots \\ \{G_{\text{s}}^{N_{\text{e}}}\} \end{bmatrix}, \tag{93}$$

and $[K^e] = [A^e] - k_0^2 [B^e]$ ($e = 1,...,N_{\text{e}}$). The dimension of the disconnected system can be found as

$$N_{\text{dis}} = \sum_{e=1}^{N_e} [N_u^e(N_v^e+1)(N_w^e+1) + (N_u^e+1)N_v^e(N_w^e+1) + (N_u^e+1)(N_v^e+1)N_w^e]. \quad (94)$$

Properties of the basis functions in (74)-(75) allow connection of any two elements regardless of the adopted geometrical orders, field-expansion orders, or local orientations. The only requirement that needs to be satisfied is the geometrical compatibility of the joint face, explained in Section 3.5. Shown in Fig. 4.4(a) is an example of an element (e_1) of the first geometrical order ($K^{e_1}=1$, $M^{e_1}=8$) and an element (e_2) of the second geometrical order ($K^{e_2}=2$, $M^{e_2}=27$) that are adjacent in the mesh and share a common face, as shown in Fig. 4.4(b). Moreover, the two elements have different field-approximation orders in all dimensions ($N_u^{e_1}=1$, $N_v^{e_1}=2$, $N_w^{e_1}=2$ and $N_u^{e_2}=7$, $N_v^{e_2}=5$, $N_w^{e_2}=3$).

In our assembly procedure, the geometrical interpolation nodes associated with the two elements that govern the geometry of the common face are ordered in a way that ensures a symmetrical or antisymmetrical variation of the corresponding parametric coordinates, i.e., $\{u,v,\text{or }w\}^{e_1} = \{\pm u,\pm v, \text{or} \pm w\}^{e_2}$ (for the example in Fig. 4.4(a)-(b), $u^{e_1}=-v^{e_2}$ and $w^{e_1}=-w^{e_2}$). The continuity of the tangential field across the common face is enforced by equating the corresponding tangential-field coefficients associated with e_1 and e_2, with additional sign corrections due to different orientations of the elements. The procedure has to be repeated for all faces shared by pairs of elements in the mesh and is formally carried out by assembling the connectivity matrix $[C]$ such that

$$\{\alpha^{\text{dis}}\} = [C] \cdot \{\alpha^{\text{con}}\}, \quad (95)$$

where $\{\alpha^{\text{con}}\}$ and $\{\alpha^{\text{dis}}\}$ represent the unknown coefficient vectors of the connected and disconnected systems, respectively [10]. The analysis of faces is sufficient, as it automatically ensures the field continuity across the edges. The relevant coefficients

and functions governing the tangential field on hexahedron faces can be deduced from (74)-(75). They are shown in Table 4.1, along with the adopted local numeration of faces and corresponding values of fixed local parametric coordinates.
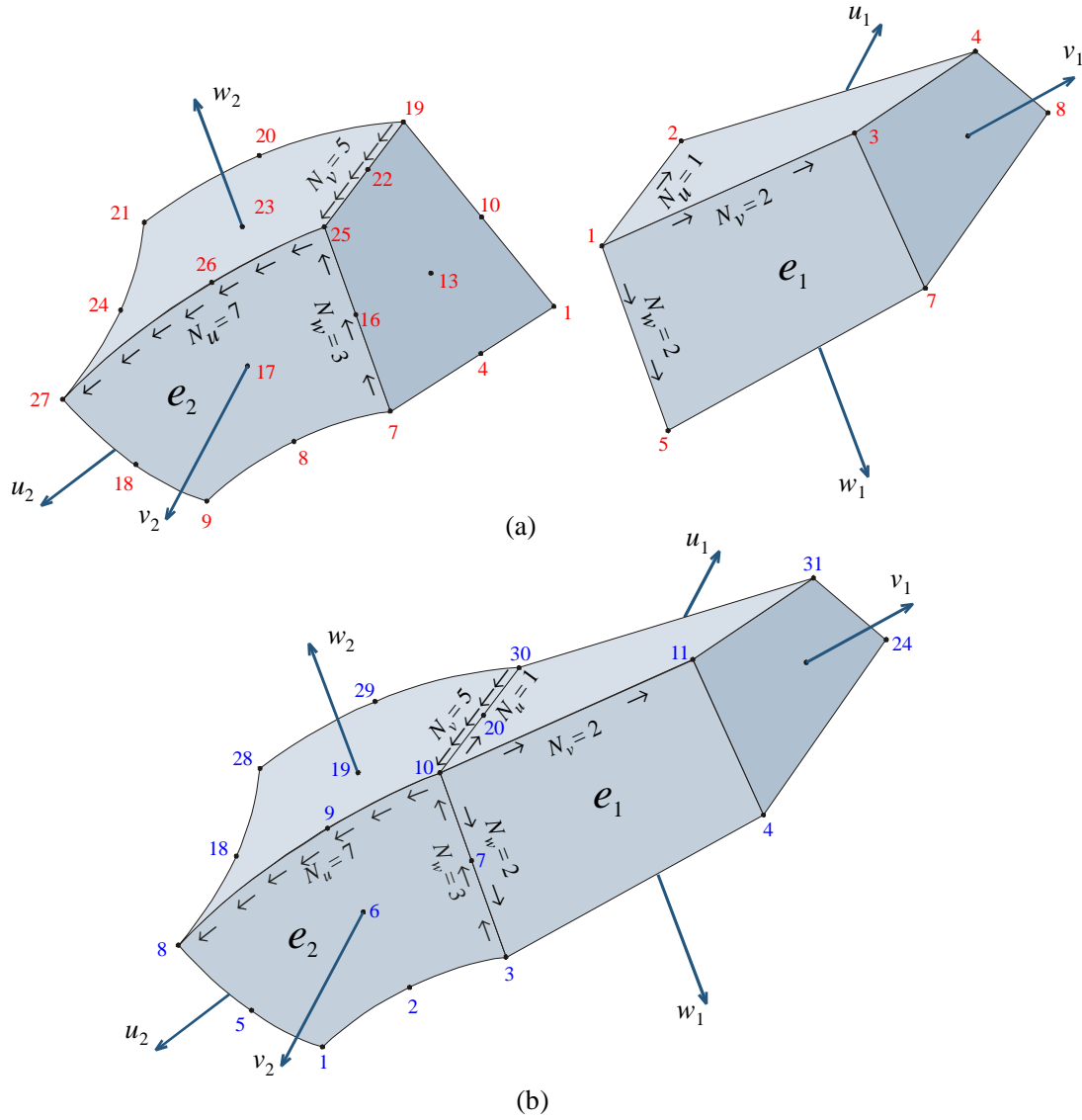
Fig. 4.4. A connection of two elements with different geometrical orders, field approximation orders, and spatial orientations. (a) Individual elements with local node numbering and (b) connected elements with global node numbering.

Note that, unless P_0 or P_1 are involved, the functions in the table are either symmetrical or antisymmetrical. This simplifies the assembly of $[C]$, because the only intervention needed in cases when the local orientations of the corresponding edges do not match is the multiplication of the respective entries by (–1). The rooftop functions P_0 and P_1 are neither symmetrical nor antisymmetrical, so that the simple sign change of the individual entries alone does not solve the problem. However, the rooftop functions satisfy the relationship $P_0(u) = P_1(-u)$, hence the problem can be solved by additionally interchanging the coefficients associated with them, i.e., by interchanging the corresponding rows in $[C]$. The coefficients are matched only up to the lesser of the corresponding field-expansion orders for adjacent elements and are set to zero for the remaining tangential-field basis functions. This order reduction pertains to the common face only and does not influence the expansions throughout the rest of the volumes of the higher order elements. Once matrix $[C]$ has been assembled, the final connected system is generated by substituting (95) into (92) and multiplying the resulting equation by $[C]^T$, which yields

$$[C]^T [K^{\text{dis}}][C]\{\alpha^{\text{con}}\} = [C]^T \{G^{\text{dis}}\}, \tag{96}$$

where the connected system matrix and free-term vector are given by $[K^{\text{con}}] = [C]^T [K^{\text{dis}}][C]$ and $\{G^{\text{con}}\} = [C]^T \{G^{\text{dis}}\}$, respectively. In the actual FEM code, the formalism described by (92)-(96) is not carried out explicitly, because this would require unnecessary large storage space and increase in computational time, but a direct assembly of the connected system is performed instead, which implicitly includes all the above equations and considerations. In our direct assembly procedure, each unknown $\alpha^e_{i_{uvw}ijk}$ (where i_{uvw} takes the values 1, 2 or 3 for α_{uijk}, α_{vijk} or α_{wijk}, respectively) is first assigned a unique disconnected global number i_{dis}. The results of coefficient matching, determined during the topological analysis, are then saved in the form of a N_{dis}-dimensional connectivity vector $\{D\}$, rather then a matrix

[C], in which the element $D_{i_{\text{dis}}}$ is assigned: a next unique positive integer i_{con}, if the currently considered unknown $\alpha_{i_{\text{dis}}}$ does not match any of the previous unknowns [$\alpha_{i_{\text{dis}}} \neq \alpha_{j_{\text{dis}}}$, $(0 < j_{\text{dis}} < i_{\text{dis}})$]; a value $\pm D_{j_{\text{dis}}}$, if $\alpha_{i_{\text{dis}}}$ matches a previously considered unknown [$\alpha_{i_{\text{dis}}} = \pm \alpha_{j_{\text{dis}}}$, $(0 < j_{\text{dis}} < i_{\text{dis}})$]; or zero, if $\alpha_{i_{\text{dis}}} = 0$.

Table 4.1. Coefficients and functions governing the tangential field
at hexahedron faces; for the assembly of the connectivity matrix.

Face number	Fixed coordinate	Coefficient	Function
1	$u = -1$	α_{v0jk}	$\alpha_{v0jk} v^j P_k(w)$
		α_{w0jk}	$\alpha_{w0jk} P_j(v) w^k$
2	$u = +1$	α_{v1jk}	$\alpha_{v1jk} v^j P_k(w)$
		α_{w1jk}	$\alpha_{w1jk} P_j(v) w^k$
3	$v = -1$	α_{ui0k}	$\alpha_{ui0k} u^i P_k(w)$
		α_{wi0k}	$\alpha_{wi0k} P_i(u) w^k$
4	$v = +1$	α_{ui1k}	$\alpha_{ui1k} u^i P_k(w)$
		α_{wi1k}	$\alpha_{wi1k} P_i(u) w^k$
5	$w = -1$	α_{uij0}	$\alpha_{uij0} u^i P_j(v)$
		α_{vij0}	$\alpha_{vij0} P_i(u) v^j$
6	$w = +1$	α_{uij1}	$\alpha_{uij1} u^i P_j(v)$
		α_{vij1}	$\alpha_{vij1} P_i(u) v^j$

Once the connectivity vector $\{D\}$ has been defined, the global connected system is assembled according to the algorithm shown in Fig. 4.5. Note that, due to symmetry involved (as explained in Section 2.5), only the upper triangular parts of matrices [A^{con}] and [B^{con}] are assembled. The resulting connected system (assuming the lower symmetric triangular parts are added)

$$[K^{\text{con}}]\{\alpha^{\text{con}}\} = \{G_{\text{S}}^{\text{con}}\}, \qquad [K^{\text{con}}] = [A^{\text{con}}] - k_0^2[B^{\text{con}}] \tag{97}$$

has the dimension N^{con}, which is determined by the highest positive integer in the vector $\{D\}$, and it can be shown that it is equivalent to the system formally obtained in (96).
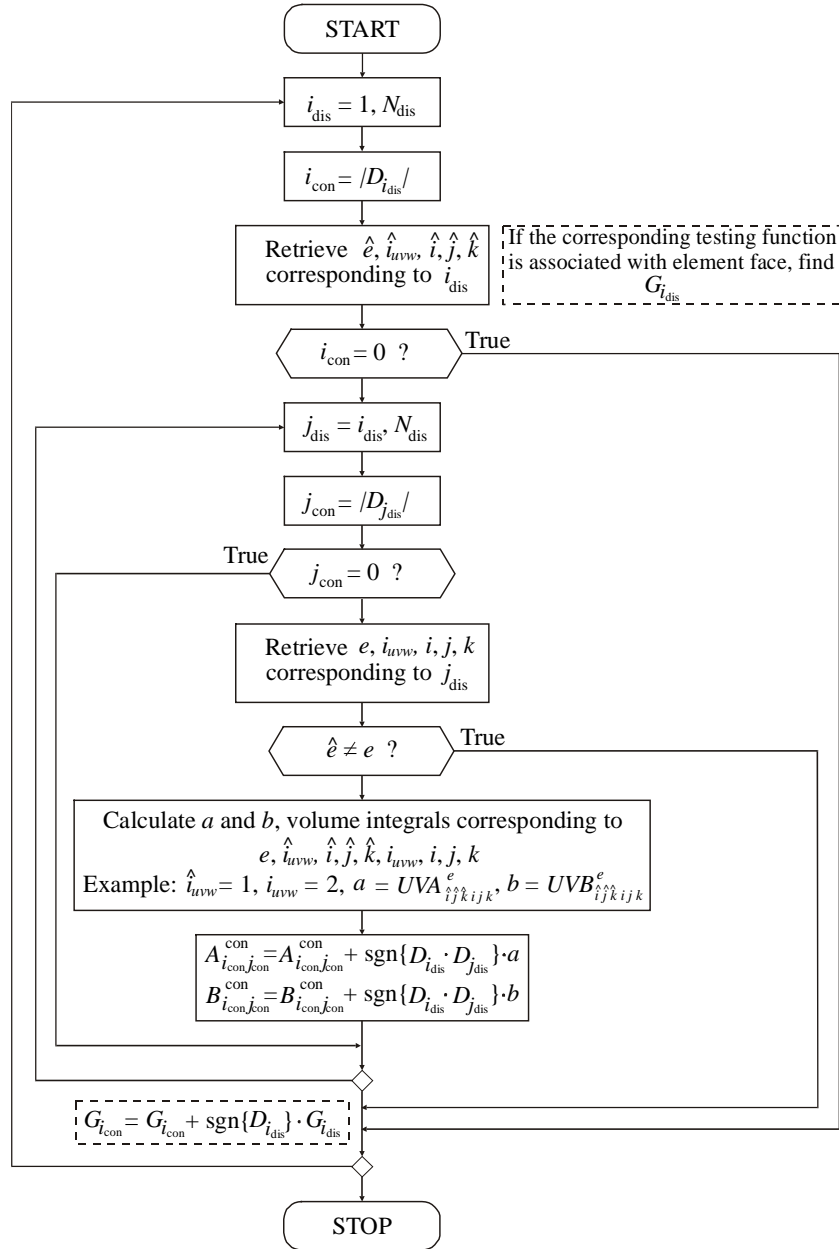
Fig. 4.5. Assembly of the connected system.

In the algorithm shown in Fig. 4.5, the operations regarding the assembly of the right-hand side vector $\{G_\text{S}^\text{con}\}$ are outlined with the broken line for the reason explained next. Due to continuity of tangential component of the magnetic field intensity vector, $\boldsymbol{n} \times \boldsymbol{H}$, in (78) across the interface between any two finite elements in the connected FEM model, the right-hand side terms $\{G_\text{S}^\text{con}\}$ in (97) for the connected model (after the virtual summations shown in the algorithm have been applied) contain the surface-integral over the overall boundary surface of the entire FEM domain, and not over the internal boundary surfaces between the individual hexahedra in the model. In other words, the terms in $\{G_\text{S}^\text{con}\}$ associated with the interface between two adjacent elements in the FEM mesh can be a priori set to zero, thus implicitly satisfying condition (9) in the distributional sense defined by the weighted integral (97). The (remaining) tangential component of $\boldsymbol{H}$ over the boundary surface of the entire FEM domain is determined by the boundary conditions imposed at the surface. This provides a foundation for a numerical interface between the FEM domain and the remaining space for modeling of unbounded problems (e.g., antennas and scatterers), i.e., for implementing mesh-termination schemes based on absorbing boundary conditions [56], artificial absorbers [57], and integral equations [61-69], all leading to different versions of hybrid FEM methodologies.

We finally conclude that in the assembled connected system, both (tangential-type) natural boundary conditions, given by (7) and (9), are satisfied. The first condition (continuity of tangential electric field) is satisfied explicitly, by equating the corresponding coefficients governing the tangential components of electric field at element interfaces, whereas the second (continuity of tangential magnetic field) is satisfied implicitly and in a distributional sense, by zeroing out the corresponding terms in $\{G_\text{S}^\text{con}\}$. Hence, the only thing remaining, before the system can be solved, is to explicitly enforce the essential (Dirichlet type) boundary conditions. This is done by assigning each degree of freedom located on the Dirichlet boundary the value of the

corresponding Dirichlet condition (e.g., for the PEC boundary, by setting the coefficients associated with the tangential electric field at the boundary to zero). Generally, however, the assigned values may be different for different parts of the boundary, and the conditions may be provided as a linear combination, as well. The most frequently used methods for imposing the essential boundary conditions are the method of the *dominant diagonal term*, the method of the *constant term over the diagonal*, and the method of *elimination of equations* [11]. The last method consists of restructuring the system by eliminating rows and columns corresponding to the degrees of freedom that should be enforced through the essential boundary conditions. This method has the advantage over the first two, since it reduces the number of unknowns and the overall system dimension, hence it was the method of choice for our final FEM matrix assembly procedure. To optimize the method even more, and contrary to the generally adopted procedure where the enforcement of the essential conditions follows the assembly of the global connected matrix, in our procedure the essential boundary conditions are technically imposed before the system is assembled. For instance, in the case of PEC boundary, the corresponding degrees of freedom are annihilated by setting to zero the additional entries in vector $\{D\}$, prenumerating the remaining entries and then proceeding with the algorithm shown in Fig. 4.5, as it will be shown in more detail in Sections 5.2 and 5.3. This way, the basis functions associated with the unknown coefficients affected by the enforcement of essential boundary conditions are not used as test functions, thus simplifying and accelerating the system assembly process.

4.6.   Conclusion

The set of hierarchical polynomial curl-conforming vector basis functions of arbitrary orders has been proposed in this Chapter, and implemented for curved hexahedral elements, described in Chapter 3, to obtain the novel, highly flexible, volume finite elements. The mathematical development of the proposed finite elements has been

presented and numerical components of the new finite element technique have been described. This includes implementation of hierarchical polynomial vector basis functions for higher order modeling of fields within the generalized curvilinear hexahedral elements, Galerkin testing procedure for discretizing the double-curl electric-field vector wave equation, and numerical procedures for evaluation of the resulting volume-integrals. A connection technique has been proposed for elements with arbitrary geometrical orders, field-expansion orders, and local orientations leading to the efficient assembly of the higher order connectivity matrix and generation of the final FEM matrix.

The new elements enable excellent curvature modeling (e.g., a sphere is practically perfectly modeled by a single curved hexahedral finite element) and excellent field-distribution modeling (e.g., 10th-order polynomial field-approximation in the three parametric coordinates in a hexahedral finite element). This enables using as large as $2\lambda \times 2\lambda \times 2\lambda$ curved hexahedra as building blocks for modeling of the electromagnetic structure (which is 20 times the traditional low-order modeling discretization limit of $\lambda/10$ in each dimension). Element orders in the model, however, can also be low, so that the lower-order modeling approach is actually included in the higher order modeling. Most importantly, because the proposed basis functions are hierarchical, a whole spectrum of element sizes (from a very small fraction of λ to 2λ), geometrical orders (from 1 to 4), and field-approximation orders (from 1 to 10) can be used at the same time in a single simulation model of a complex structure, making this method essentially a combined, low-to-high, order method. Additionally, the technique provides a whole range of element shapes (e.g., brick-like, slab-like, and rod-like planar hexahedra, as well as spherically-shaped, cylindrically-shaped, and elliptically-shaped curved hexahedra, and also other "irregular" and/or curved hexahedral shapes) to be used in a simulation model as well.

In Chapter 6, the new finite elements are used to obtain the FEM solutions to closed- and open-region EM problems.

5. EXAMPLES OF CLOSED-REGION AND OPEN-REGION EM ANALYSIS BY NEW FINITE ELEMENT METHOD

5.1. Introduction

In this Chapter, we utilize the developed higher order curved hexahedral finite elements to build the tools for the computational analysis of closed- and open-region EM problems. These tools will then be used to evaluate the performance of the new finite elements and to obtain the numerical results shown in Chapter 6.

FEM is the method of choice for numerical analysis and simulation of EM phenomena occurring in closed-domains, i.e., EM cavities, due to existence of simple boundary conditions that naturally limit the presence of fields to a finite domain and thus provide the means for exact simple mesh-termination, in this case. Hence, the focus of this thesis will be the analysis of closed-region problems, which will also be used to evaluate the performance of the new finite elements.

Analysis of open-region EM problems (e.g., antennas and scatterers), not being natural to FEM, is presented in this Chapter for two reasons only: as a starting point in providing a foundation for a numerical interface between the FEM domain and the remaining space for modeling of unbounded problems, i.e., for implementing mesh-termination schemes based on absorbing boundary conditions [54-60], artificial absorbers [57], and integral equations [61-69], all leading to different versions of hybrid FEM methodologies, and as a concrete example of open-region analysis by

FEM via implementation of absorbing boundary conditions in the new FEM technique.

5.2. Analysis of closed-region problems; eigenvalue analysis

From the theoretical point of view, analysis of closed-region problems is particularly interesting for assessing the performance of the FEM method, since the accuracy of the solution is not affected by the accuracy of the boundary conditions imposed on the domain boundaries, which, in this case, are exact. The same fact is one of the reasons that makes FEM the method of choice in analysis of arbitrarily shaped cavities, when the analytical eigenvalue analysis cannot be performed and numerical techniques must be used. In practice, on the other hand, analysis of closed cavity problems is very important for the design and control of many devices like particle accelerators, microwave filters, microwave ovens, optical fibers, etc [30].

In analysis of metallic cavities, boundary conditions require the tangential component of the electric field intensity vector, E, to vanish near the cavity walls, which is the simplest mesh-termination technique. This essential boundary condition is easily enforced by a priori setting to zero the coefficients associated with the tangential E on the sides (generalized quadrilateral surfaces) of elements adjacent to cavity walls,

$$\begin{cases} \alpha_{v0jk} = \alpha_{w0jk} = 0, & u = -1 \\ \alpha_{v1jk} = \alpha_{w1jk} = 0, & u = 1 \\ \alpha_{ui0k} = \alpha_{wi0k} = 0, & v = -1 \\ \alpha_{ui1k} = \alpha_{wi1k} = 0, & v = 1 \\ \alpha_{uij0} = \alpha_{vij0} = 0, & w = -1 \\ \alpha_{uij1} = \alpha_{vij1} = 0, & w = -1 \end{cases}. \tag{98}$$

We note that elementary surfaces on the sides of elements are given by

$$
\mathrm{d}S = \begin{cases}
-\boldsymbol{a}''_u \,\mathrm{d}v\mathrm{d}w, & u=-1 \ (\text{Face 1})\\
\boldsymbol{a}''_u \,\mathrm{d}v\mathrm{d}w, & u=+1 \ (\text{Face 2})\\
-\boldsymbol{a}''_v \,\mathrm{d}w\mathrm{d}u, & v=-1 \ (\text{Face 3})\\
\boldsymbol{a}''_v \,\mathrm{d}w\mathrm{d}u, & v=+1 \ (\text{Face 4})\\
-\boldsymbol{a}''_w \,\mathrm{d}u\mathrm{d}v, & w=-1 \ (\text{Face 5})\\
\boldsymbol{a}''_w \,\mathrm{d}u\mathrm{d}v, & w=+1 \ (\text{Face 6})
\end{cases}
\tag{99}
$$

and that (78) for the connected model can be rewritten to read

$$
G_{\mathrm{s}\hat{i}\hat{j}\hat{k}} = -\mathrm{j}k_0\eta_0 \oint_S \mathrm{d}S \times \boldsymbol{f}_{\hat{i}\hat{j}\hat{k}} \cdot \boldsymbol{H} \ .
\tag{100}
$$

Upon incorporating equations (99), (74)-(75), and (51) into (100), we conclude that $G_{\mathrm{s}\hat{i}\hat{j}\hat{k}}$ is nonzero only in those linear equations in the system (rows of the system matrix) that correspond to the unknown coefficients (columns of the system matrix) already set to zero in (98). Those linear equations can, therefore, be eliminated from the system (prior to system assembly, as explained in the previous Section), which leads to a system with $\{G_{\mathrm{s}}\} = 0$ and the following generalized eigenvalue problem:

$$
[A]\{\alpha\} = k_0^2[B]\{\alpha\},
\tag{101}
$$

where k_0^2 are the eigenvalues and corresponding $\{\alpha\}$ are the eigenvectors of the system. This system is solved for all eigenvalues, using a standard eigenvalue solver. Alternatively, if the modal field distributions are needed, the system is also solved for the eigenvectors $\{\alpha\}$ (being actually the unknown coefficients of the connected system). The original coefficients of the disconnected system are then found from (95), and substituted back into expansion (73), written for all elements in the mesh, to obtain the unknown total electric field anywhere in the cavity.

5.3.   Analysis of open-region problems; scattering analysis

5.3.1.   Absorbing boundary conditions

Contrary to numerical approaches that deal with sources of the fields (currents and charges) as the unknowns (e.g., MoM), FEM deals with the differential form of Maxwell's field equations which, as a consequence, involves a discretization of the complete region where the EM fields exist. In closed-region problems, the fields are naturally bounded by perfectly conducting walls, whereas in the open-region problems (e.g., antenna and scattering problems) the natural boundary does not exist, the fields occupy an infinite region thus making the discretization by FEM, in the classical sense, numerically impossible. However, FEM can be modified in different ways to enable treating open-region problems. This topic is one of the major problems in FEM; its scope is extremely broad and very widely investigated, hence it will not be discussed in more detail and only a concise classification of the methods, developed for analysis of open-region problems in FEM, is given in Table 5.1.[12]

In our FEM method, the Absorbing Boundary Conditions (ABCs) [54-60] are used as a convenient technique for the infinite domain truncation. The technique imposes approximate local conditions across the faces of elements associated with the FEM domain outer boundary, thus simulating the zero-reflection conditions of the open space and enabling the effective mesh-termination, while preserving the simplicity of FEM method and sparsity of the final system [which is not the case with (exact) integral techniques]. A general form of ABCs, given in [54], is next shortly described and implemented for the newly developed finite elements.

---

[12] Comprehensive classification of the methods can be found in [11].

Table 5.1. Classification of the methods dealing with open-region problems in FEM

Artificial shielding	Picture-frame methods	Perfectly matched layer (PML)

- Infinite elements
- Recursive condensation
- Infinitesimal scaling
	Local boundary conditions
	  - Absorbing Boundary Conditions (ABCs)
	  - Numerical ABCs (NABCs)
	
	Non-local (integral) boundary conditions
	  - Hybrid Finite Element – Boundary Integral method (FE-BI method)
	  - Eigenfunction expansion (Unimoment method)
	  - Other hybrid methods (e.g., FEM-MoM)	

In free space, exterior to the scatterer (or radiator) structure, the scattered (or radiated) field, E^{sc}, satisfies the homogeneous vector wave equation (double-curl equation)

$$\nabla \times \nabla \times E^{sc} - k_0^2 E^{sc} = 0, \tag{102}$$

obtained from (15) by substituting $\varepsilon_r = \mu_r = 1$ [13] and the Sommerfeld radiation condition at infinity [9]. Such a field can be represented by the infinite series [55]

$$E^{sc}(r) = \frac{e^{-jk_0 r}}{r} \sum_{n=0}^{\infty} \frac{A_n(\theta, \phi)}{r^n}, \tag{103}$$

(r, θ, ϕ) being the spherical coordinates. The differential operator

$$\mathcal{L}_m(u) = i_r \times \nabla \times u - \left(jk_0 + \frac{m}{r} \right) u, \qquad (m = 0, 1, 2, \ldots) \tag{104}$$

is introduced, and it can be shown that

---

[13] A similar equation holds for any homogeneous exterior region, if medium parameters are substituted by the corresponding constant ε_r and μ_r, and k_0 is substituted by $k = k_0 (\varepsilon_r \mu_r)^{1/2}$.

$$\mathcal{L}_m \left(\frac{A_{n_t}(\theta,\phi)}{r^{n+1}} e^{-jk_0 r} \right) = (n-m) e^{-jk_0 r} \frac{A_{n_t}(\theta,\phi)}{r^{n+2}}, \qquad (m \geq 0,\ n \geq 0), \qquad (105)$$

and

$$\mathcal{L}_m \left[\nabla_t \left(\frac{A_{n_r}(\theta,\phi)}{r^{n+1}} e^{-jk_0 r} \right) \right] = (n+1-m) \nabla_t \left(e^{-jk_0 r} \frac{A_{n_r}(\theta,\phi)}{r^{n+2}} \right), (m \geq 0,\ n \geq 0),$$

$$(106)$$

where subscripts t and r, respectively, denote the transverse (to radial direction) and radial parts of the associated vector and $\boldsymbol{i}_r$ is the radial ort. In both cases $\mathcal{L}_m$ has the effect of multiplying the given expression with $1/r$ while leaving the angular dependence unchanged. With this in mind, the new operator $\mathcal{B}_m$ ($m = 1,2,3,\dots$) is defined as

$$\mathcal{B}_m = (\mathcal{L}_{m-1})^m (\boldsymbol{u}_t) + s(\mathcal{L}_m)^{m-1} (\nabla_t u_r), \qquad (107)$$

where s stands for an arbitrary number. From (105)-(107) it can be shown that

$$\mathcal{B}_m \left(\frac{A_n(\theta,\phi)}{r^{n+1}} \right) = (n+1-m)(n+2-m) \cdot \ldots \cdot (n-1)n\, e^{-jk_0 r} \frac{A_{n_t}(\theta,\phi)}{r^{n+1+m}} +$$

$$+ s(n+1-m)(n+2-m) \cdot \ldots \cdot (n-2)(n-1)\nabla_t \left(e^{-jk_0 r} \frac{A_{n_r}(\theta,\phi)}{r^{n+m}} \right).$$

$$(108)$$

The right-hand side of (108) vanishes for all n ($n \leq m-1$) which means that $\mathcal{B}_m$ annihilates the first m terms in (103) leaving only the terms with $n > m-1$ (which are proportional to $1/r^{n+m+1}$) hence we can conclude that

$$\mathcal{B}_m(\boldsymbol{E}^{sc}) = O(1/r^{2m+1}), \qquad (109)$$

and that the statement

$$\mathcal{B}_m(\boldsymbol{E}^{\mathrm{sc}}) = 0, \tag{110}$$

represents an approximate boundary condition applicable to a spherical surface of radius r, which includes all radiation sources.

Typically, first- or second-order ABCs are utilized in actual FEM implementations since higher order conditions are mathematically complicated and numerically cumbersome. It can be shown that the first-order condition, $\mathcal{B}_1(\boldsymbol{E}^{\mathrm{sc}}) = 0$, reduces to

$$\boldsymbol{i}_r \times \nabla \times \boldsymbol{E}^{\mathrm{sc}} = \mathrm{j}k_0 \boldsymbol{E}_t^{\mathrm{sc}}, \qquad s = 1, \tag{111}$$

and that the second-order condition, $\mathcal{B}_2(\boldsymbol{E}^{\mathrm{sc}}) = 0$, reduces to

$$\boldsymbol{i}_r \times \nabla \times \boldsymbol{E}^{\mathrm{sc}} = \mathrm{j}k_0 \boldsymbol{E}_t^{\mathrm{sc}} + \frac{r}{2(\mathrm{j}k_0 r + 1)} \{\nabla \times [\boldsymbol{i}_r (\nabla \times \boldsymbol{E}^{\mathrm{sc}})_r + \nabla_t (\nabla \cdot \boldsymbol{E}_t^{\mathrm{sc}})]\}, \quad s = 2. \tag{112}$$

The s-number values, $s = 1$ and $s = 2$, for the first- and second-order condition, respectively, are chosen to simplify the final expressions for the ABCs (by annihilating certain terms) and to produce symmetric final systems, whereas the optimum choice (that minimizes the reflection coefficient at the ABC surface) would be $s = 1/2$ [9].

5.3.2. FEM solution of a scattering problem using absorbing boundary conditions

Implementation of ABCs for the new finite elements will be demonstrated on the example of a 3-D scattering problem illustrated in Fig. 5.1, where an EM wave, generated outside of the shown domain and described by the known incident electric field vector $\boldsymbol{E}^{\mathrm{inc}}$, impinges on a body (scatterer) inducing currents and charges,

which in turn produce the unknown scattered field, described by the scattered electric field vector $\boldsymbol{E}^{\mathrm{sc}}$. To solve the problem for the unknown $\boldsymbol{E}^{\mathrm{sc}}$, or alternatively for the unknown total field

$$\boldsymbol{E} = \boldsymbol{E}^{\mathrm{inc}} + \boldsymbol{E}^{\mathrm{sc}}, \tag{113}$$

(both occupying an unbounded and infinitely large volume) using FEM, a fictitious spherical surface S, completely enclosing the scatterer, is introduced to truncate the domain of interest from the rest of the (infinite) space, thus reducing the problem to one discussed and discretized by finite elements in Chapter 2. To obtain unique solution, however, a boundary condition that makes the fictitious surface as transparent as possible for the outgoing waves has to be imposed on S, and to achieve this, the ABCs described in Section 5.3.1 are used.
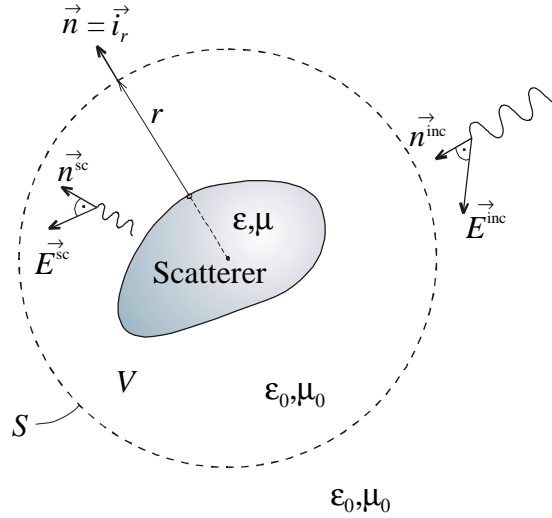
Fig. 5.1. Illustration of a 3-D scattering problem.

Both first- and second-order conditions given by (111) and (112), respectively, can be formally written as [60]

$$i_r \times \nabla \times \boldsymbol{E}^{\text{sc}} + P(\boldsymbol{E}^{\text{sc}}) = 0, \tag{114}$$

where

$$P(\boldsymbol{E}^{\text{sc}}) = -\text{j}k_0 \boldsymbol{E}_t^{\text{sc}} \tag{115}$$

for the first- and

$$P(\boldsymbol{E}^{\text{sc}}) = -\text{j}k_0 \boldsymbol{E}_t^{\text{sc}} - \frac{r}{2(\text{j}k_0 r + 1)} \{\nabla \times [i_r (\nabla \times \boldsymbol{E}^{\text{sc}})_r + \nabla_t (\nabla \cdot \boldsymbol{E}_t^{\text{sc}})]\} \tag{116}$$

for the second-order condition. Consider the weighted residual (30) for the whole domain V enclosed by S

$$\int_V \mu_r^{-1} (\nabla \times \boldsymbol{w}) \cdot (\nabla \times \boldsymbol{E}) \, \text{d}V - k_0^2 \int_V \varepsilon_r \boldsymbol{w} \cdot \boldsymbol{E} \, \text{d}V - \oint_S \mu_r^{-1} \boldsymbol{w} \times (\nabla \times \boldsymbol{E}) \cdot \text{d}\boldsymbol{S} = 0, \tag{117}$$

$\boldsymbol{E}$ being the total electric field given by (113). After rearranging the terms of the mixed-product in the surface-integral, and taking advantage of the fact that S is spherical and resides in free space ($\mu_r = 1$), it can be shown that

$$\oint_S \mu_r^{-1} \boldsymbol{w} \times (\nabla \times \boldsymbol{E}) \cdot \text{d}\boldsymbol{S} = -\oint_S (\boldsymbol{n} \times \nabla \times \boldsymbol{E}) \cdot \boldsymbol{w} \, \text{d}S = -\oint_S \boldsymbol{w} \cdot (i_r \times \nabla \times \boldsymbol{E}) \, \text{d}S, \tag{118}$$

where $\text{d}\boldsymbol{S} = \boldsymbol{n} \, \text{d}S$ and $i_r = \boldsymbol{n}$ on the spherical surface S, and (117) can be rewritten as

$$\int_V \mu_r^{-1} (\nabla \times \boldsymbol{w}) \cdot (\nabla \times \boldsymbol{E}) \, \text{d}V - k_0^2 \int_V \varepsilon_r \boldsymbol{w} \cdot \boldsymbol{E} \, \text{d}V + \oint_S \boldsymbol{w} \cdot (i_r \times \nabla \times \boldsymbol{E}) \, \text{d}S = 0. \tag{119}$$

Using (113) and (114), we can conclude that

$$i_r \times \nabla \times \boldsymbol{E} = i_r \times \nabla \times \boldsymbol{E}^{\text{inc}} - P(\boldsymbol{E} - \boldsymbol{E}^{\text{inc}}) \tag{120}$$

which can be rewritten as

$$i_r \times \nabla \times E = U^{\text{inc}} - P(E) \tag{121}$$

where U^{inc} represents the group of the known terms defined by

$$U^{\text{inc}} = i_r \times \nabla \times E^{\text{inc}} + P(E^{\text{inc}}). \tag{122}$$

Finally, the total-field "weak" formulation with imposed ABC is obtained by substituting (121) into (119) which yields

$$\int_V \mu_r^{-1}(\nabla \times w) \cdot (\nabla \times E)\, dV - k_0^2 \int_V \varepsilon_r w \cdot E\, dV - \oint_S w \cdot P(E)\, dS = -\oint_S w \cdot U^{\text{inc}}\, dS. \tag{123}$$

Alternatively, theoretically equivalent but numerically different, scattered-field "weak" formulation [58,60] could have been used.

Substituting the second-order ABC (116), applied to E instead of E^{sc}, into the surface-integral term on the left-hand side of (123), we obtain

$$-\oint_S w \cdot P(E)\, dS = T_1 + T_2 + T_3, \tag{124}$$

where

$$T_1 = jk_0 \oint_S w \cdot E_t\, dS, \tag{125}$$

$$T_2 = \oint_S \frac{r}{2(jk_0 r + 1)} w \cdot [\nabla \times [i_r (\nabla \times E)_r]]\, dS, \qquad \text{and} \tag{126}$$

$$T_3 = \oint_S \frac{r}{2(jk_0 r + 1)} w \cdot \nabla_t (\nabla \cdot E_t)\, dS, \tag{127}$$

The term T_1 is the only one associated with the first-order ABC and it can be evaluated in its present form. The remaining two terms, however, associated with the second-order ABC, need to be somewhat simplified first. Invoking the vector identity

$\nabla \cdot (\boldsymbol{A} \times \boldsymbol{B}) = \boldsymbol{B} \cdot (\nabla \times \boldsymbol{A}) - \boldsymbol{A} \cdot (\nabla \times \boldsymbol{B})$, where $\boldsymbol{A} = \boldsymbol{i}_r (\nabla \times \boldsymbol{E})_r$ and $\boldsymbol{B} = \boldsymbol{w}$, and the surface-divergence theorem, the second term can be reduced to

$$T_2 = \oint_S \frac{r}{2(\mathrm{j}k_0 r + 1)} (\nabla \times \boldsymbol{w})_r \cdot (\nabla \times \boldsymbol{E})_r \, \mathrm{d}S \,. \tag{128}$$

Similarly, invoking the identity $\nabla \cdot (V\boldsymbol{B}_t) = \nabla_t V \cdot \boldsymbol{B} + V \nabla \cdot \boldsymbol{B}_t$, where $V = \nabla \cdot \boldsymbol{E}_t$ and $\boldsymbol{B} = \boldsymbol{w}$, and the same theorem, the third term becomes

$$T_3 = -\oint_S \frac{r}{2(\mathrm{j}k_0 r + 1)} (\nabla \cdot \boldsymbol{w}_t)(\nabla \cdot \boldsymbol{E}_t) \, \mathrm{d}S \,. \tag{129}$$

Substituting expansion (73) into expressions for T_1, T_2 and T_3, and having in mind that in the Galerkin testing procedure testing functions $\boldsymbol{w}$ take the form of the basis functions $\boldsymbol{f}$ used for the unknown function expansion, we conclude that T_1 and T_2 can be readily evaluated by integrating the expressions involving the proposed basis functions and their curls, given by (74) and (85), respectively. Integral T_3, on the other hand, requires evaluation of divergences of the basis functions. For the curved finite elements proposed here, this cannot be done analytically and numerical differentiation would have to be employed. Numerical differentiation, however, is generally avoided due to the cumbersome procedures involved and possible significant loss of accuracy. Hence, we conclude that the new higher order generalized hexahedral finite elements are not suitable for the enforcement of the second-order ABC, and proceed to the implementation of the first-order condition only. Note that for the first-order simple vector elements with constant geometrical parameters (e.g., bricks, tetrahedra and triangular prisms), basis functions are divergence-free, thus enabling easy implementation of the second-order ABC, since the term T_3 vanishes.

Substituting (124)-(125) into (123) (first-order ABC only) and applying the discretization by FEM, described in Chapter 4, the following system is obtained

$$[K]\{\alpha\} = \{G_s\}, \qquad [K] = [A] - k_0^2[B] + jk_0[S], \qquad (130)$$

where matrices $[A]$, $[B]$ and vector $\{\alpha\}$ are assembled from their elemental forms given by (81)-(83) and (84), respectively, whereas $[S]$ and $\{G_s\}$ are assembled from matrices $[S^e]$ and vectors $\{G_s^e\}$ defined, respectively, by

$$[S^e] = \begin{bmatrix} [UUS^e] & [UVS^e] & [UWS^e] \\ [VUS^e] & [VVS^e] & [VWS^e] \\ [WUS^e] & [WVS^e] & [WWS^e] \end{bmatrix}, \qquad (131)$$

$$\{G_s^e\} = \begin{bmatrix} \{UG_{s\hat{i}\hat{j}\hat{k}}^e\} \\ \{VG_{s\hat{i}\hat{j}\hat{k}}^e\} \\ \{WG_{s\hat{i}\hat{j}\hat{k}}^e\} \end{bmatrix}, \qquad (132)$$

and the elements of the corresponding submatrices and subvectors have the form

$$UUS_{\hat{i}\hat{j}\hat{k}ijk}^e = \int\limits_{S^e} \boldsymbol{f}_{u\hat{i}\hat{j}\hat{k}_t}^e \cdot \boldsymbol{f}_{uijk_t}^e \, \mathrm{d}S ,$$

$$UVS_{\hat{i}\hat{j}\hat{k}ijk}^e = \int\limits_{S^e} \boldsymbol{f}_{u\hat{i}\hat{j}\hat{k}_t}^e \cdot \boldsymbol{f}_{vijk_t}^e \, \mathrm{d}S , \qquad (133)$$

$$UG_{s\hat{i}\hat{j}\hat{k}}^e = -\int\limits_{S^e} \boldsymbol{f}_{u\hat{i}\hat{j}\hat{k}_t}^e \cdot \boldsymbol{U}^{\mathrm{inc}} \, \mathrm{d}S ,$$

$$VG_{s\hat{i}\hat{j}\hat{k}}^e = -\int\limits_{S^e} \boldsymbol{f}_{v\hat{i}\hat{j}\hat{k}_t}^e \cdot \boldsymbol{U}^{\mathrm{inc}} \, \mathrm{d}S ,$$

$$WG_{s\hat{i}\hat{j}\hat{k}}^e = -\int\limits_{S^e} \boldsymbol{f}_{w\hat{i}\hat{j}\hat{k}_t}^e \cdot \boldsymbol{U}^{\mathrm{inc}} \, \mathrm{d}S , \qquad (134)$$

with analogous expressions for the elements of other submatrices of $[S^e]$. The domain of the surface-integrals, S^e, consists of all faces of the e-th hexahedron associated with the fictitious spherical boundary S,

$$S^e = \bigcup_{\substack{i=1 \\ S_p^e \subset S}}^{6} S_p^e, \tag{135}$$

S_p^e being the p-th face of the e-th generalized hexahedron in the mesh. Finally, we remark that in the process of obtaining expressions (133)-(134), the identity $\mathbf{A} \cdot \mathbf{B}_t = \mathbf{A}_t \cdot \mathbf{B}_t$ was invoked.

5.3.3. Evaluation of the surface-integrals and global matrix filling

Integration across the faces of a hexahedron (generalized quadrilateral surfaces) is performed similarly to volume-integration described in Section 4.4, namely it is done across the faces of a parent cube element (see Fig. 3.3.), in the $u - v - w$ domain, as

$$\int_{S_1^e} f(v,w)\, \mathrm{d}S = \int\int_{v\,w} f(v,w)\,|\boldsymbol{J}_{su}(v,w)|\,\mathrm{d}v\mathrm{d}w, \qquad u = -1 \ \text{and} \ -1 \le v, w \le 1,$$

$$\tag{136}$$

for the first face, and analogously for the remaining five faces, where expressions for the surface-Jacobians, $\boldsymbol{J}_s$, for all six faces can be deduced from (56) and (99). The integration is carried out using the Gauss-Legendre twofold integration formula in $N_v^{\mathrm{GL}} \times N_w^{\mathrm{GL}}$ points, i.e.,

$$\int_{v=-1}^{1}\int_{w=-1}^{1} q(-1,v,w)\,\mathrm{d}v\mathrm{d}w = \sum_{n=1}^{N_v^{\mathrm{GL}}} W_n^v \sum_{l=1}^{N_w^{\mathrm{GL}}} W_l^w\, q(-1,v_n,w_l) \tag{137}$$

$q(-1,v,w)$ being an arbitrary scalar function, and v_n and w_l, and W_n^v and W_l^w being, respectively, the integration points and corresponding weighting coefficients defined on a -1 to 1 interval. The analogous expressions are obtained for the remaining five faces.

Consider, for example, element $UVS^e_{\hat{i}\hat{j}\hat{k}ijk}$ integrated across the fifth face ($p = 5$, $w = -1$). It is evaluated as follows:

$$UVS^e_{\hat{i}\hat{j}\hat{k}ijk} = \int_{S_5} \boldsymbol{f}_{u\hat{i}\hat{j}\hat{k}_t} \cdot \boldsymbol{f}_{vijk_t} \, \mathrm{d}S = \int_{S_5} P_{u\hat{i}\hat{j}\hat{k}} P_{vijk} \, \boldsymbol{a}^r_{u_t} \cdot \boldsymbol{a}^r_{v_t} \, \mathrm{d}S , \qquad w = -1, \qquad (138)$$

where the superscript e has been dropped in order to simplify the expressions. Transversal (to radial direction) components of the reciprocal unitary vectors are tangential to spherical surface S, which itself is (approximately) conformal with the hexahedron face S_5. Hence, using the identity $\boldsymbol{A}_t \cdot \boldsymbol{B}_t = (\boldsymbol{n} \times \boldsymbol{A}) \cdot (\boldsymbol{n} \times \boldsymbol{B})$, $\boldsymbol{n}$ being the outward unit normal on S_5 (and S), substituting $\boldsymbol{A} = \boldsymbol{a}^r_u$, $\boldsymbol{B} = \boldsymbol{a}^r_v$ and $\boldsymbol{n} = -\boldsymbol{a}''_w / |\boldsymbol{a}''_w|$ on S_5, which can be deduced from (99), and applying the formula analogous to that given by (136), we get

$$UVS^e_{\hat{i}\hat{j}\hat{k}ijk} = \int_{u=-1}^{1} \int_{v=-1}^{1} P_{u\hat{i}\hat{j}\hat{k}} P_{vijk} \, \frac{-\boldsymbol{a}''_w \times \boldsymbol{a}''_u}{J} \cdot \frac{-\boldsymbol{a}''_w \times \boldsymbol{a}''_v}{J} \, \frac{|\boldsymbol{a}''_w|}{|\boldsymbol{a}''_w|^2} \, \mathrm{d}u \mathrm{d}v , \quad w = -1 .$$
$$(139)$$

From (53)-(55) we can conclude that

$$\frac{-\boldsymbol{a}''_w \times \boldsymbol{a}''_u}{J} = -\boldsymbol{a}_v , \qquad \frac{-\boldsymbol{a}''_w \times \boldsymbol{a}''_v}{J} = \boldsymbol{a}_u , \qquad (140)$$

thus substituting (140) into (139) and applying the summation analogous to one given by (137), we obtain

$$UVS^e_{\hat{i}\hat{j}\hat{k}ijk} = - \int_{u=-1}^{1} \int_{v=-1}^{1} P_{u\hat{i}\hat{j}\hat{k}} P_{vijk} \, \boldsymbol{a}_v \cdot \boldsymbol{a}_u \, \frac{1}{|\boldsymbol{a}''_w|} \, \mathrm{d}u \mathrm{d}v =$$
$$= \sum_{m=1}^{N^{\mathrm{GL}}_u} W^u_m \sum_{n=1}^{N^{\mathrm{GL}}_v} W^v_n \left[P_{u\hat{i}\hat{j}\hat{k}} P_{vijk} \, (a_{v_x} a_{u_x} + a_{v_y} a_{u_y} + a_{v_z} a_{u_z}) \cdot \right.$$
$$\left. \cdot (a''^2_{w_x} + a''^2_{w_y} + a''^2_{w_z})^{-1/2} \right]_{u_m, v_n, w=-1} . \qquad (141)$$

All other elements of matrix $[S^e]$ are evaluated in analogous fashion. Note that in the surface-integrals in $[S^e]$, only tangential (to fictitious surface S and hexahedral faces S_p^e associated with it) components of the basis functions appear in the integrand, thus for the certain face-basis function combinations the integral vanishes. This happens when a basis function has a normal component on the given hexahedral face only, which is a priori known from (54), (74) and (99), hence the corresponding integrals need not be evaluated explicitly. Instead, the process can be optimized by explicitly evaluating only the non-zero surface-integrals according to Table 5.2. Due to symmetry involved, only the upper triangular elements of $[S^e]$ are shown in the table.

Table 5.2. Evaluation table for the surface-integrals appearing in $[S^e]$.

Local face number → Integral type ↓	1	2	3	4	5	6
UUS^e	0	0	*evaluate*	*evaluate*	*evaluate*	*evaluate*
UVS^e	0	0	0	0	*evaluate*	*evaluate*
UWS^e	0	0	*evaluate*	*evaluate*	0	0
VVS^e	*evaluate*	*evaluate*	0	0	*evaluate*	*evaluate*
VWS^e	*evaluate*	*evaluate*	0	0	0	0
WWS^e	*evaluate*	*evaluate*	*evaluate*	*evaluate*	0	0

In order to evaluate the excitation-vector integrals (134), consider a plane-wave excitation given by

$$\mathbf{E}^{\text{inc}} = \mathbf{E}_0 \, e^{-jk_0 \mathbf{r} \cdot \mathbf{n}_{\text{inc}}} , \tag{142}$$

$\mathbf{r} = \mathbf{r}(u,v,w)$ being the radius-vector of the point under consideration, $\mathbf{n}_{\text{inc}}$ being the ort in the incoming direction of the incident wave propagation defined by

$$\mathbf{n}^{\text{inc}}(\theta^{\text{inc}}, \phi^{\text{inc}}) = -\sin(\theta^{\text{inc}})\cos(\phi^{\text{inc}})\,\mathbf{i}_x - \sin(\theta^{\text{inc}})\sin(\phi^{\text{inc}})\,\mathbf{i}_y - \cos(\theta^{\text{inc}})\,\mathbf{i}_z , \tag{143}$$

θ^{inc} and ϕ^{inc} being the usual coordinates in the (r, θ, ϕ) spherical system, and $\boldsymbol{E}_0$ being the electric field vector of the incident wave at the origin, usually defined as

$$\boldsymbol{E}_0 = E_\theta \, \boldsymbol{i}_\theta^{\text{inc}} + E_\phi \, \boldsymbol{i}_\phi^{\text{inc}}, \tag{144}$$

where

$$
\begin{aligned}
\boldsymbol{i}_\theta^{\text{inc}} &= \cos(\theta^{\text{inc}})\cos(\phi^{\text{inc}})\,\boldsymbol{i}_x + \cos(\theta^{\text{inc}})\sin(\phi^{\text{inc}})\,\boldsymbol{i}_y - \sin(\theta^{\text{inc}})\,\boldsymbol{i}_z, \\
\boldsymbol{i}_\phi^{\text{inc}} &= -\sin(\phi^{\text{inc}})\,\boldsymbol{i}_x + \cos(\phi^{\text{inc}})\,\boldsymbol{i}_y,
\end{aligned}
\tag{145}
$$

as shown in Fig. 5.2.
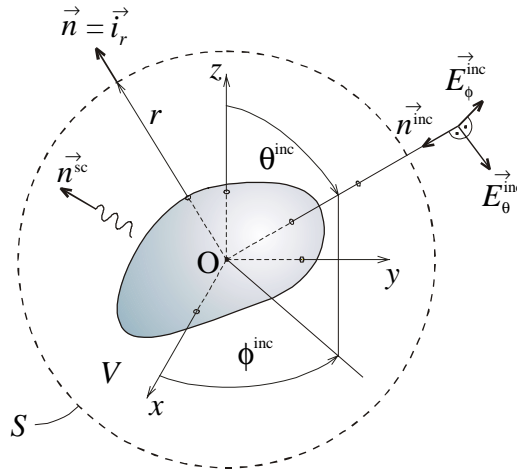
Fig. 5.2. Details of the plane-wave excitation in the scattering problem.

From (115) and (122) we conclude that

$$\boldsymbol{U}^{\text{inc}} = \boldsymbol{i}_r \times \nabla \times \boldsymbol{E}^{\text{inc}} - \mathrm{j}k_0 \boldsymbol{E}_t^{\text{inc}}. \tag{146}$$

Substituting (146) into (134) we get

$$UG^e_{s\hat{i}\hat{j}\hat{k}} = - \int_{S^e} f^e_{u\hat{i}\hat{j}\hat{k}_t} \cdot [i_r \times \nabla \times E^{\text{inc}} - jk_0 E^{\text{inc}}_t] \, dS \,, \tag{147}$$

which, using the fact that $i_r = n$ on the spherical surface S, the identity $A_t \cdot B_t = (n \times A) \cdot (n \times B)$ and letting $A = f^e_u$ and $B = E^{\text{inc}}$, and rearranging the terms of the mixed-product in the integrand, can be rewritten as

$$UG^e_{s\hat{i}\hat{j}\hat{k}} = \int_{S^e} (n \times f^e_{u\hat{i}\hat{j}\hat{k}}) \cdot (\nabla \times E^{\text{inc}} + jk_0 n \times E^{\text{inc}}) \, dS \,, \tag{148}$$

Substituting (144) into (142) and the obtained result into (148), and applying the procedure analogous to one described for elements of the $[S^e]$ matrix, for the integral across S_5 ($p = 5$, $w = -1$) we get

$$UG^e_{s\hat{i}\hat{j}\hat{k}} = \sum_{m=1}^{N^{\text{GL}}_u} W^u_m \sum_{n=1}^{N^{\text{GL}}_v} W^v_n \, \cdot$$

$$\cdot \left[P_{u\hat{i}\hat{j}\hat{k}} \, e^{-jk_0 r \cdot n^{\text{inc}}} [E_\theta (i^{\text{inc}}_\phi - \frac{a''_w}{|a''_w|} \times i^{\text{inc}}_\theta) + E_\phi (-i^{\text{inc}}_\theta - \frac{a''_w}{|a''_w|} \times i^{\text{inc}}_\phi)] \cdot (-a_v) \right]_{u_m, v_n, w=-1}$$

$$\tag{149}$$

where $\nabla \times E^{\text{inc}}$ was found to be

$$\nabla \times E^{\text{inc}} = jk_0 (E_\theta \, i^{\text{inc}}_\phi - E_\phi \, i^{\text{inc}}_\theta) \, e^{-jk_0 r \cdot n^{\text{inc}}} \,. \tag{150}$$

Analogous expressions hold for all other elements of vector $\{G^e_{\text{S}}\}$. In excitation-vector integrals (134), basis functions appear only as testing functions, hence the evaluation table is simplified, as shown in Table 5.3.

Table 5.3. Evaluation table for the surface-integrals appearing in $\{G_s^e\}$.

Local face number → Integral type ↓	1	2	3	4	5	6
UG_s^e	0	0	*evaluate*	*evaluate*	*evaluate*	*evaluate*
VG_s^e	*evaluate*	*evaluate*	0	0	*evaluate*	*evaluate*
WG_s^e	*evaluate*	*evaluate*	*evaluate*	*evaluate*	0	0

Finally, we remark that the assembly of the final (connected) system (130), for the scattering problem, is also performed according to the algorithm shown in Fig. 4.5, where the elements of [*S*]-matrix are computed in the same loop with the elements of matrices [*A*] and [*B*], whereas the elements of the excitation vector {*G*} are computed in the steps outlined by the broken line. Naturally, both [*S*]-matrix and {*G*}-vector elements are computed only if the corresponding element and face are associated with fictitious surface *S*, and if the corresponding entries in Table 5.2 and Table 5.3, respectively, are not zero. Once the system is assembled, it is solved for the unknown coefficients {α} (being actually the coefficients of the connected system). The original coefficients of the disconnected system are easily found from (95), and substituted back into expansion (73), written for all elements in the mesh, to obtain the unknown total electric field anywhere within *V* (and on *S*). If needed, equation (113) can be used to obtain $\boldsymbol{E}^{\text{sc}}$.

5.3.4. Calculating far-field scattering pattern from the near-field FEM solution

In order to obtain a far-field scattering pattern (generally required in scattering analysis) from the near-field FEM solution, we employ a convenient representation of the Kirchhoff's integral formula whose derivation and implementation are described next.

Consider first a scalar field $\psi(\boldsymbol{r})$ satisfying the scalar Helmholtz wave equation

$$(\Delta + k_0^2)\psi(\boldsymbol{r}) = 0 \tag{151}$$

inside a domain V bounded by a closed surface S. A Green's function $G(\boldsymbol{r}, \boldsymbol{r}')$ defined by

$$(\Delta + k_0^2)G(\boldsymbol{r}, \boldsymbol{r}') = -\delta(\boldsymbol{r} - \boldsymbol{r}'), \tag{152}$$

δ being the Dirac delta function, is introduced next and the second Green's identity

$$\int\limits_V (\phi\Delta\psi - \psi\Delta\phi)\,\mathrm{d}V = \oint\limits_S \left[\phi\,\boldsymbol{n}\cdot\nabla\psi - \psi\,\boldsymbol{n}\cdot\nabla\phi\right]\mathrm{d}S, \tag{153}$$

$\boldsymbol{n}$ being the outward unit normal to S, is employed letting the scalar fields $\phi = G$ and $\psi = \psi$, which, making the use of (151), (152) and the properties of Dirac delta function, yields

$$\psi(\boldsymbol{r}) = \oint\limits_S [\psi(\boldsymbol{r}')\,\boldsymbol{n}'\cdot\nabla'G(\boldsymbol{r}, \boldsymbol{r}') - G(\boldsymbol{r}, \boldsymbol{r}')\,\boldsymbol{n}'\cdot\nabla'\psi(\boldsymbol{r}')]\,\mathrm{d}S', \tag{154}$$

provided that $\boldsymbol{r}$ resides inside V (otherwise the left-hand side vanishes) and $\boldsymbol{n}'$ being the inward unit normal to S. Considering ψ to be, one by one, three rectangular components of $\boldsymbol{E}$, all of them independently satisfying (151), applying (154) for each component, multiplying the result with the associated rectangular ort and adding all three results together, yields

$$\boldsymbol{E}(\boldsymbol{r}) = \oint\limits_S \{\boldsymbol{E}(\boldsymbol{r}')[\boldsymbol{n}'\cdot\nabla'G(\boldsymbol{r}, \boldsymbol{r}')] - G(\boldsymbol{r}, \boldsymbol{r}')\,(\boldsymbol{n}'\cdot\nabla')\boldsymbol{E}(\boldsymbol{r}')\}\,\mathrm{d}S'. \tag{155}$$

In order to make thus obtained expression more convenient for the implementation, some additional integral theorems of vector calculus need to be applied. The theorems, however, require the integrands to be well-behaved functions, which is not

the case in (155) due to singularity of G at $r' = r$. To avoid the singularity, an infinitesimally small surface S' is introduced around the point $r' = r$ thus excluding it from V, which makes the left-hand side of (155) vanish, whereas the evaluation of the right-hand side integral over S', in the limit as it shrinks to zero around $r' = r$, gives $-E(r)$ [74]. With this in mind, we rewrite (155) as

$$0 = \oint_S \{2E(r')[n' \cdot \nabla' G(r,r')] - n' \cdot \nabla'[G(r,r')E(r')]\} \, dS' \tag{156}$$

and apply the divergence theorem to the second integral term, which yields

$$0 = \oint_S 2E(r')[n' \cdot \nabla' G(r,r')] \, dS' + \int_V \Delta'[G(r,r')E(r')] \, dV'. \tag{157}$$

Utilizing the vector identity $\Delta A = \nabla(\nabla \cdot A) - \nabla \times \nabla \times A$, with letting $A = GE$, as well as the divergence and curl theorems [73], the volume integral in (157) can be transformed back into a surface integral, yielding

$$0 = \oint_S \{2E(r')[n' \cdot \nabla' G(r,r')] \, dS' - n'[\nabla' \cdot [G(r,r')E(r')]] +$$
$$+ n' \times [\nabla' \times [G(r,r')E(r')]]\} \, dS', \tag{158}$$

which, after carrying out the differentiation of the product GE, employing Maxwell's equation (5) for the homogeneous medium, and letting S' shrink to zero (or in other words making $r' = r$ part of V again), becomes

$$E(r) = \oint_S \{n' \times [\nabla' \times E(r')] G(r,r') + [n' \times E(r')] \times \nabla' G(r,r') +$$
$$+ [n' \cdot E(r')] \nabla' G(r,r')\} \, dS'. \tag{159}$$

To apply (159) to the general scattering problem shown in Fig. 5.1, we construct S so that

$$S = S_1 \bigcup S_2, \tag{160}$$

as shown in Fig. 5.3, where S_1 coincides with S from Fig. 5.1 and S_2 extends to infinity, and we choose a suitable free-space Green's function

$$G(\boldsymbol{r},\boldsymbol{r}') = \frac{1}{4\pi}\frac{\mathrm{e}^{-jk_0|\boldsymbol{r}-\boldsymbol{r}'|}}{|\boldsymbol{r}-\boldsymbol{r}'|}. \tag{161}$$

Substituting (160) and (161) back into (159), it can be shown that the contribution of the integral over S_2 vanishes when S_2 extends to infinity, if the field in region II (see Fig. 5.3) is considered as a scattered field, thus yielding [74]

$$\boldsymbol{E}^{\mathrm{sc}}(\boldsymbol{r}) = \oint_{S_1} \{\boldsymbol{n}'\times[\nabla'\times\boldsymbol{E}^{\mathrm{sc}}(\boldsymbol{r}')]\,G(\boldsymbol{r},\boldsymbol{r}') + [\boldsymbol{n}'\times\boldsymbol{E}^{\mathrm{sc}}(\boldsymbol{r}')]\times\nabla'G(\boldsymbol{r},\boldsymbol{r}') +$$
$$+[\boldsymbol{n}'\cdot\boldsymbol{E}^{\mathrm{sc}}(\boldsymbol{r}')]\,\nabla'G(\boldsymbol{r},\boldsymbol{r}')\}\,\mathrm{d}S', \tag{162}$$

also known as the *vector Kirchhoff integral relation*, which expresses a scattered field in any point in region II as an integral of the scattered fields over finite S_1 completely enclosing the scatterer (all sources of the scattered field). The scattered field on the right-hand side of the Kirchhoff's formula can be replaced by the total field $\boldsymbol{E}$, defined by (113), without affecting the validity of the formula since

$$\oint_{S_1} \{\boldsymbol{n}'\times[\nabla'\times\boldsymbol{E}^{\mathrm{inc}}(\boldsymbol{r}')]\,G(\boldsymbol{r},\boldsymbol{r}') + [\boldsymbol{n}'\times\boldsymbol{E}^{\mathrm{inc}}(\boldsymbol{r}')]\times\nabla'G(\boldsymbol{r},\boldsymbol{r}') +$$
$$+[\boldsymbol{n}'\cdot\boldsymbol{E}^{\mathrm{inc}}(\boldsymbol{r}')]\,\nabla'G(\boldsymbol{r},\boldsymbol{r}')\}\,\mathrm{d}S' = 0, \tag{163}$$

(with $\boldsymbol{r}$ in region II) which is a mathematical statement of the fact that the unperturbed incident field does not produce any scattered field [9].

Far-field scattering pattern in the direction of $\boldsymbol{i}_r$, being the ort of $\boldsymbol{r}$, can be obtained from (162) by letting $|\boldsymbol{r}|\gg|\boldsymbol{r}'|$ and using the fact that (in the far-field zone) $\boldsymbol{E}^{\mathrm{sc}}$ is transverse to $\boldsymbol{r}$, which, respectively, gives

$$G(\boldsymbol{r},\boldsymbol{r}') \rightarrow \frac{1}{4\pi}\frac{\mathrm{e}^{-\mathrm{j}k_0 r}}{r}\mathrm{e}^{-\mathrm{j}k_0 \boldsymbol{i}_r \cdot \boldsymbol{r}'} \qquad \text{and}$$

$$\nabla' G(\boldsymbol{r},\boldsymbol{r}') \rightarrow \mathrm{j}k_0 G\,\boldsymbol{i}_r\,, \tag{164}$$

and makes the third term in (162) vanish, finally yielding

$$\boldsymbol{E}^{\mathrm{sc}}(\boldsymbol{r}) = \frac{\mathrm{e}^{-\mathrm{j}k_0 r}}{4\pi r}\oint\limits_{S_1}\{\boldsymbol{n}'\times[\nabla'\times\boldsymbol{E}(\boldsymbol{r}')]+\mathrm{j}k_0[\boldsymbol{n}'\times\boldsymbol{E}(\boldsymbol{r}')]\times\boldsymbol{i}_r\}\,\mathrm{e}^{\mathrm{j}k_0 \boldsymbol{i}_r \cdot \boldsymbol{r}'}\,\mathrm{d}S'\,, \tag{165}$$

where $r = |\boldsymbol{r}|$, and the total field, being the actual solution of our FEM problem, was used in the surface-integral instead of the scattered field.
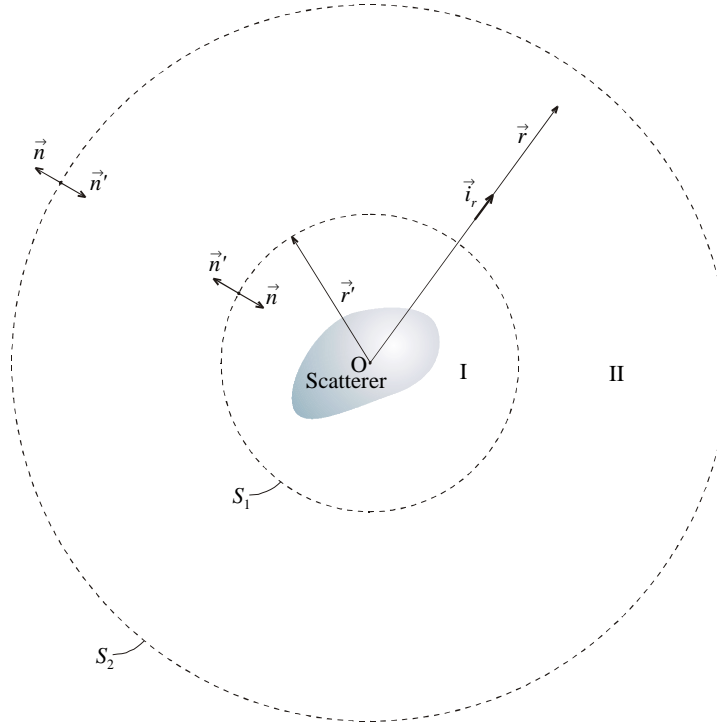
Fig. 5.3. Application of the vector Kirchhoff integral relation (162) in calculation of the scattered field external to S_1; S_1 completely encloses the scatterer (all sources of the scattered field) and coincides with S from Fig. 5.1, whereas S_2 extends to infinity. Note that region II in the figure, with the inner and outer unit normals ($\boldsymbol{n}'$ and $\boldsymbol{n}$, respectively) on its bounding surfaces correspond, respectively, to domain V and the unit normals used in (153)-(159).

Substituting FEM solution $\boldsymbol{E}(\boldsymbol{r}') = \boldsymbol{E}(u, v, w)$, obtained by means explained in Section 5.3.3 and given in the form of expansion (73) written for all elements in the mesh, into (165), the formula can be rewritten as the sum of surface integrals (across all faces of hexahedral elements associated with the fictitious spherical boundary S_1) where $\boldsymbol{E}(\boldsymbol{r}')$ is replaced with the corresponding vector basis functions, $\boldsymbol{f}_u$, $\boldsymbol{f}_v$ and $\boldsymbol{f}_w$, denoted as the far-field vector integrals $\boldsymbol{UFF}$, $\boldsymbol{VFF}$ and $\boldsymbol{WFF}$, respectively, multiplied by the corresponding expansion coefficients. In other words, we can write

$$
\boldsymbol{E}^{\mathrm{sc}}(\boldsymbol{r}) = \frac{\mathrm{e}^{-\mathrm{j}k_0 r}}{4\pi r} \cdot
$$

$$
\cdot \sum_{\substack{e, S_p^e \\ \text{associated with} \\ \text{spherical boundary}}} \left[\sum_{i=0}^{N_u^e-1} \sum_{j=0}^{N_v^e} \sum_{k=0}^{N_w^e} \alpha_{uijk}^e \boldsymbol{UFF}_{ijk}^e + \sum_{i=0}^{N_u^e} \sum_{j=0}^{N_v^e-1} \sum_{k=0}^{N_w^e} \alpha_{vijk}^e \boldsymbol{VFF}_{ijk}^e + \right.
$$

$$
\left. + \sum_{i=0}^{N_u^e} \sum_{j=0}^{N_v^e} \sum_{k=0}^{N_w^e-1} \alpha_{wijk}^e \boldsymbol{WFF}_{ijk}^e \right],
$$

$$(166)$$

where, applying numerical integration technique described in Section 5.3.3, we find the expression for $\boldsymbol{UFF}_{ijk}^e$, integrated (for example) across S_5 ($p=5$, $w=-1$), to be

$$
\boldsymbol{UFF}_{ijk}^e = \oint_{S_5} \{\boldsymbol{n}' \times [\nabla' \times \boldsymbol{f}_{uijk}] + \mathrm{j}k_0 [\boldsymbol{n}' \times \boldsymbol{f}_{uijk}] \times \boldsymbol{i}_r\} \, \mathrm{e}^{\mathrm{j}k_0 \boldsymbol{i}_r \cdot \boldsymbol{r}'} \, \mathrm{d}S' =
$$

$$
= \sum_{m=1}^{N_u^{\mathrm{GL}}} W_m^u \sum_{n=1}^{N_v^{\mathrm{GL}}} W_n^v \, \mathrm{e}^{\mathrm{j}k_0 \boldsymbol{i}_r \cdot \boldsymbol{r}'} \left[-\mathrm{j}k_0 P_{uijk} \boldsymbol{a}_v \times \boldsymbol{i}_r - \right.
$$

$$
\left. - \frac{1}{J} \boldsymbol{a}_w'' \times (P_{ui\dot{j}k} \boldsymbol{a}_v - P_{ui\dot{j}k} \boldsymbol{a}_w) \right]_{u_m, v_n, w=-1}.
$$

$$(167)$$

Analogous expressions hold for all remaining vector integrals.

5.4.   Conclusion

The implementation of the new finite elements in computational analysis of both closed- and open-region EM problems has been demonstrated in this Chapter using, respectively, an example of EM cavity-mode analysis and analysis of a generalized scattering problem. Comprehensive and detailed descriptions of techniques, algorithms and procedures leading to the effective evaluation of the involved integrals and to the successful assembly of the global FEM system have been given in both examples.

Discretization of closed-region EM problems by means of the new finite elements, described in Section 5.2, enables simple and extremely accurate analysis of metallic cavities, which will be demonstrated through numerous canonical examples given in Section 6.3.

Strictly speaking, the Galerkin-type FEM solution of the generalized scattering problem with implementation of the ABCs, described in Section 5.3, holds for a spherical absorbing surface. However, the results will also be valid, but somewhat less accurate, for any nonspherical smooth surface, which could conform more closely to the shape of the scatterer. Usually, the implementation of the conformal absorbing surface deteriorates the accuracy of the solution only slightly, while significantly increasing the efficiency of the method, since the resulting FE domain is smaller and requires less elements and unknowns for discretization [9]. Alternatively, ABCs, derived for the absorbing surface with two principal radii of curvature [59,75], that provide higher accuracy when conformal absorbing surface is employed, can be used. This, however, is not the main topic of discussion in the thesis, hence only a simple spherical absorbing boundary has been employed in our FEM solutions of the examples given in Section 6.4.

The example of the generalized scattering problem has revealed a minor shortcoming of the new curved finite elements; it has been shown that they are

inconvenient for implementation of the second-order ABC, which is generally the ABC of choice in FEM modeling since it provides considerably better accuracy (than the first-order condition) without imposing significant additional computational difficulties. This conclusion, however, is not considered discouraging, since as mentioned earlier, the analysis of open-region EM problems by FEM can be done using a number of other different mesh-termination techniques (e.g., NABCs, FE-BI, FEM-MoM and PML). The implementation of alternative mesh-termination techniques will be one of the main topics of the author's future research, but cannot be addressed in more detail in this thesis due to their extremely broad scope. The implementation of the ABCs, as a mesh-termination technique, and the described application of the Kirchhoff's integral formula represent an excellent starting point in providing a numerical basis for the coupling of fields in the truncated FEM domain and the remaining space, and especially for implementing exact mesh-termination schemes based on hybrid FEM-MoM methodologies [22,65-69].

The developed computational tools for analysis of closed- and open-region problems, described in this Chapter, will next be used to analyze a number of canonical EM problems involving arbitrarily shaped metallic cavities and scatterers. The results of the performed analyses are presented in Chapter 6, where they are also compared with the results obtained analytically and/or numerically using different FEM techniques.

6. NUMERICAL RESULTS

6.1. Introduction

In this Chapter, we present the numerical results obtained in the FEM analysis of various open- and closed-region EM problems using the developed higher order curved hexahedral finite elements. Our results are compared with the analytical (where applicable) and/or alternative numerical solutions for the purpose of evaluation of the performance of the new finite elements, the efficiency of the developed FEM tools, and convergence properties of the new higher order hierarchical vector basis functions.

The results of the preliminary analysis of a 1-D scattering problem will be presented in Section 6.2. These results are obtained on a 120 MHz AMD 486 DX PC with 32 MB RAM, running Microsoft Windows 95. The results of the 3-D analysis of arbitrarily shaped cavities and scatterers will be shown in Section 6.3 and Section 6.4, respectively, and they are obtained on a 800 MHz Intel Pentium III PC (IBM ThinkPad T21) with 512 MB RAM, running Microsoft Windows 2000 Professional.

6.2. Preliminary results; plane wave scattering from a metal-backed dielectric slab

The results given in this Section demonstrate the most important conclusions obtained during the author's preliminary research, where the 1-D version of the higher order

basis functions adopted here was implemented in the FEM method in order to evaluate the efficiency, accuracy, and convergence of proposed basis functions as applied to FE modeling. A simple Galerkin-type FE routine for 1-D analysis of wave propagation through layered media was utilized [20-22].

Consider an electrically thick continuously inhomogeneous dielectric slab, shown in Fig. 6.1, with parameters $\varepsilon_r = 4 + (2 - j0.1)(1 - z/L)^2$ and $\mu_r = 2 - j0.1$, and thickness $L = 20\lambda$, backed by a perfectly conducting plane at $z = 0$, where λ is the averaged wavelength in dielectric [9].
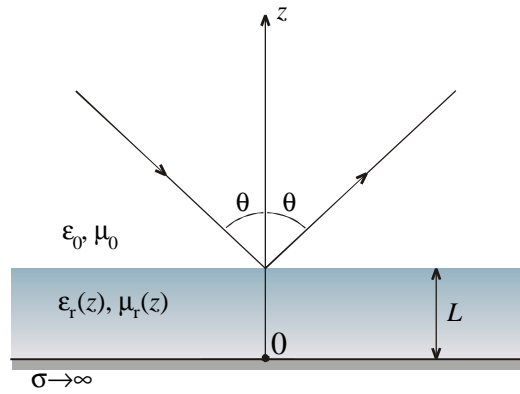
Fig. 6.1. Plane wave reflection from a metal-backed dielectric slab.

If the slab is illuminated from a vacuum, by a plane wave incident at different angles with respect to the z-axis, the problem can be solved "analytically" by dividing the slab into many thin layers and approximating the relative permittivity and permeability with constants within each layer [9]. This solution will serve as a reference for result comparison.

In Fig. 6.2 and Fig. 6.3, calculated reflection coefficient magnitude, $|R|$, is presented as a function of the angle of incidence, θ. The figures show E_z-polarization and H_z- polarization cases, respectively. Four sets of FE results, with element field-expansion orders ranging from 3 to 6, are presented in the figures and

compared with the "analytical" solution. Structure was uniformly divided into 20 elements for FE calculation. As shown, the FE solution approaches the "analytical" solution as the polynomial order (and number of unknowns) increases. It can also be noted that the agreement between the finite element solution and the "analytical" one becomes better for a larger angle of incidence. This can be explained by the fact that for large θ, propagation constant becomes small, which corresponds to a large periodicity of the field variation.
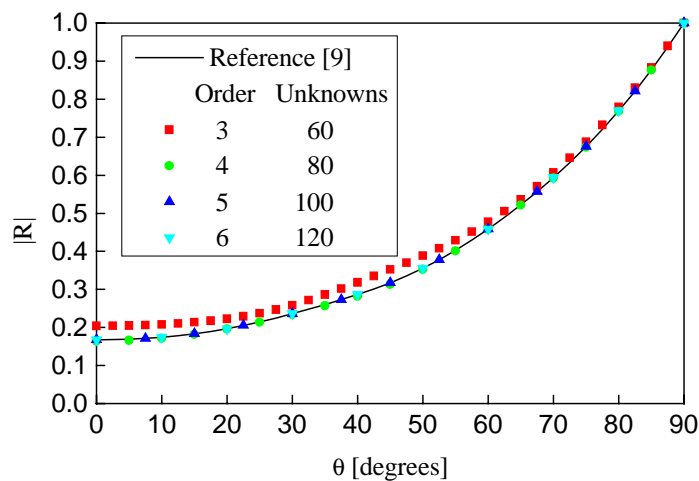
Fig. 6.2. Reflection coefficient of a metal-backed dielectric slab; E_z - polarization case.
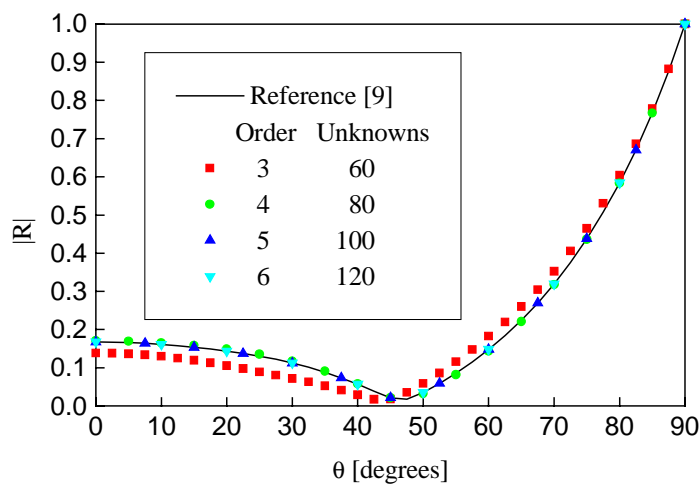
Fig. 6.3. Reflection coefficient of a metal-backed dielectric slab; H_z - polarization case.

In the next example, the slab is illuminated from a vacuum by a plane wave with parallel polarization incident at an angle of 70° with respect to the z-axis. FE results for the reflection coefficient magnitude are, again, compared with the "analytical" solution for a multi-layer approximation of the slab.

Fig. 6.4 shows the FE computational time, T, as a function of the relative error of the reflection coefficient, δ, for the small-domain FE analysis (the polynomial order is $N_u = 1$ and the number of elements, N_e, varies from 30 to 500) and the large-domain FE analysis ($N_e = 10$ and N_u varies from 3 to 8). We observe excellent accuracy and convergence properties of proposed basis functions, and their high efficiency with regards to the relative computational time. The figure demonstrates great numerical advantages of the large-domain FEs over the small-domain FEs.
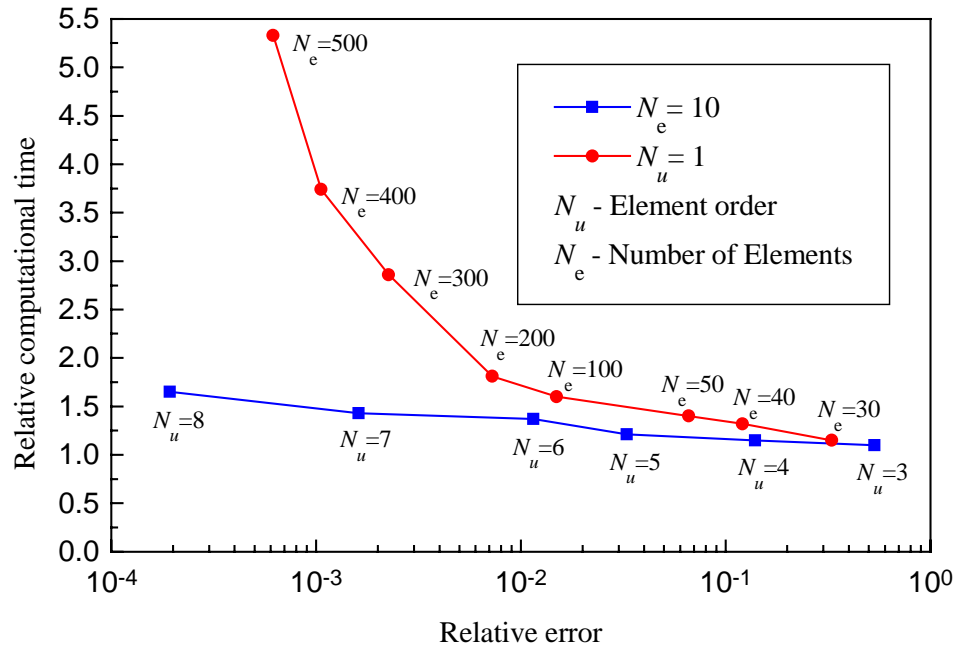
Fig. 6.4. Efficiency analysis: large-domain vs. small-domain FEs.

For the same problem, Fig. 6.5 shows the memory requirements for storage of the complex non-zero matrix elements (in double precision) and the vector of the

unknown coefficients in FE computation. Again, superiority of the large-domain FEs over the small-domain FEs is observed.
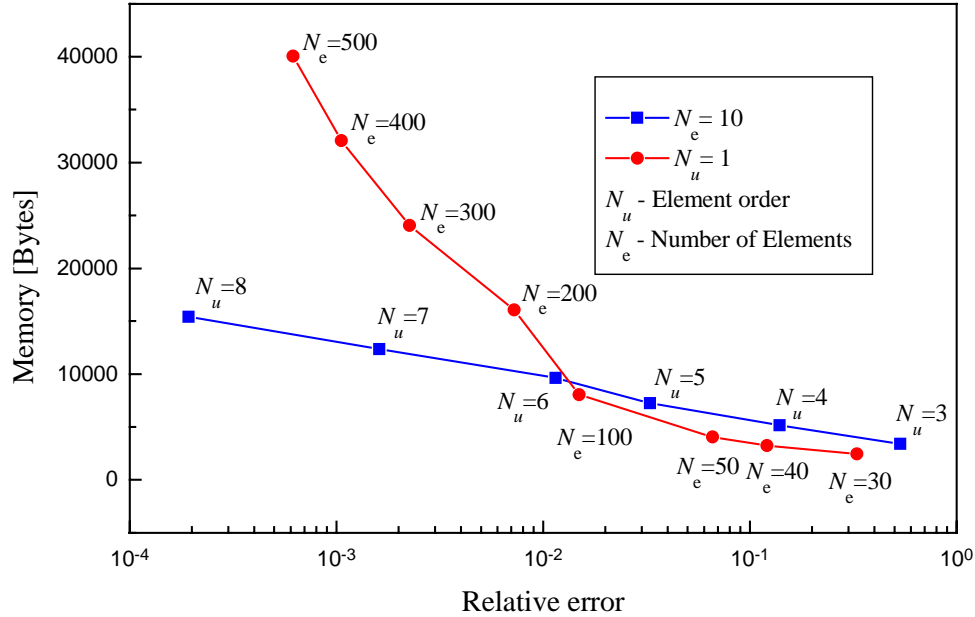
Fig. 6.5. Memory requirements: large-domain vs. small-domain FEs.

Of course, the elements cannot be arbitrarily large, i.e., very large structures have to be subdivided into a number of (large) elements. In other words, for a given (small) number of elements, it is not possible to achieve arbitrarily high accuracy by increasing the polynomial order only. Shown in Fig. 6.6 is a family of curves representing T against δ, where each curve corresponds to a fixed M and variations in T and δ are consequences of the increase of N_u. It can be observed from the figure that the increase of N_u beyond a certain value does not yield improved accuracy, that is, N_e has to be increased as well, simultaneously. The envelope line in the figure determines optimal N_e, for any given accuracy and minimal T.

Based on this, and some other numerical experiments, we have adopted 2λ to be the optimal dimension of finite elements and the general limit in the FE procedure

beyond which the structure is subdivided into smaller, but still large-domain, optimal elements (note that the corresponding small-domain limit is 0.1λ) [22].
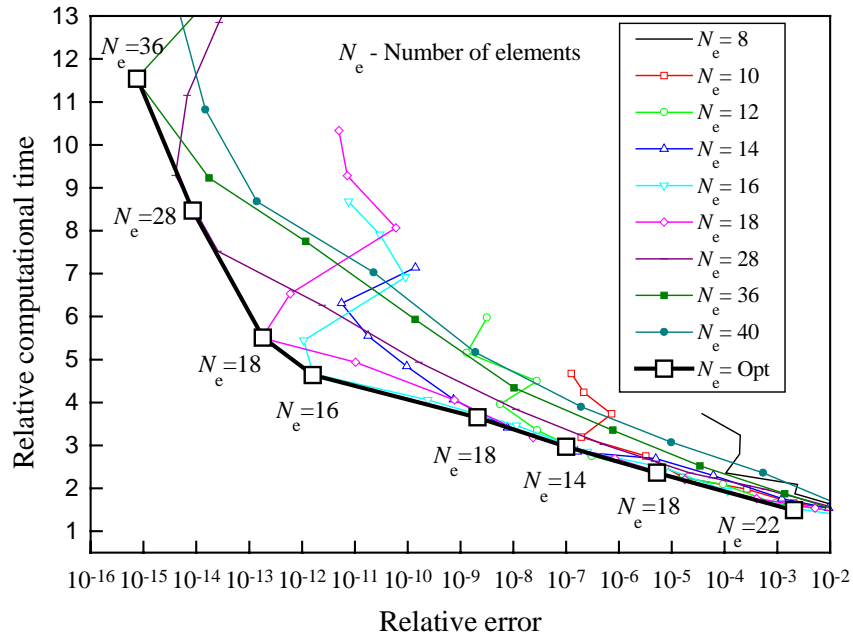
Fig. 6.6. Efficiency analysis: optimally large FEs.

6.3. Results of closed-region problem analyses; computation of cavity resonances

As the first example, consider a rectangular air-filled metallic cavity with dimensions 1 cm × 0.5 cm × 0.75 cm. Shown in Table 6.1, are the eigenvalues (resonant mode wave numbers, k_0) computed analytically, numerically using low-order node-based FEM with tetrahedral mashing and linear field expansion with 230 unknowns [9], and numerically using higher order vector FEM. In higher order vector approach, the cavity was modeled using only one trilinear hexahedral element (which in this case

reduces to a brick) and 108 unknowns ($N_u = N_v = N_w = 4$). As seen, the node-based FEM solution is corrupted with spurious modes, whereas in the vector FEM solution spurious modes vanish. Further more, although the higher order approach uses significantly less unknowns then the low-order approach (108 as compared to 230), the agreement of the higher order solution with the analytical solution is excellent for the first three modes, whereas the low-order solution gives an error of the order of 1%.

Table 6.1. Computed k_0 for the eigenvalue analysis of a rectangular cavity (1 cm × 0.5 cm × 0.75 cm); comparison of a higher order single-element vector FEM and a referent scalar FEM solution.

Mode	Exact k_0 [cm^{-1}]	Computed k_0 [cm^{-1}]	
		Scalar tetrahedra [9] 230 Unknowns	Higher order vector FEM 108 Unknowns
TE$_{101}$	5.236	5.318	5.236
	Spurious	5.759	
	Spurious	6.255	
	Spurious	6.804	
TM$_{110}$	7.025	7.067	7.025
	Spurious	7.305	
TE$_{011}$	7.551	7.389	7.551
TE$_{201}$	7.551	7.640	7.717

Shown in Table 6.2(a) are the percentage errors of the resonant mode wave numbers, k_0, computed by the higher order FEM and those obtained by low-order FEM techniques using small triangular prisms [29], bricks [30], and tetrahedra [30], respectively, as basic elements, as well as the technique using a linear tangential/quadratic normal (LT/QN) field representation on tetrahedra [42]. In the higher order FEM approach, the cavity is modeled by a single trilinear hexahedral element (which in this case reduces to a brick) and only 29 unknowns ($N_u = 4$, $N_v = 2$, $N_w = 3$). Note that this is literally an entire-domain FEM model (an entire computational domain is represented by a single finite element). It can be observed

that, for the same level of accuracy, solutions obtained by means of the higher order FEM require significantly fewer unknowns as compared to the solutions obtained by the other four methods (29 compared to 382, 270, 260, and 204, respectively). Table 6.2(b) shows a very good convergence of the higher order FEM with increasing the field-expansion polynomial orders to $N_u = N_v = N_w = 5$ and $N_u = N_v = N_w = 7$, which corresponds to a *p*-refinement of the model, the respective total numbers of unknowns being 240 and 756.

Table 6.2. Error of k_0 for the eigenvalue analysis of a rectangular cavity (1 cm × 0.5 cm × 0.75 cm): (a) comparison of a higher order single-element FEM and four reference FEM solutions; (b) convergence of the higher order single-element FEM with increasing the field-expansion polynomial orders.

Mode	k_0 [cm^{-1}] (Exact)	|Error| [%]				
		Prisms [29] 382 Unknowns	Bricks [30] 270 Unknowns	Tetrahedra [30] 260 Unknowns	LT/QN [42] 204 Unknowns	Higher order 29 Unknowns
TE$_{101}$	5.236	0.73	1.36	0.44	0.54	0.42
TM$_{110}$	7.025	2.32	2.23	0.70	0.57	0.53
TE$_{011}$	7.551	0.53	2.58	1.00	0.18	0.66
TE$_{201}$	7.551	0.64	3.13	0.56	1.89	2.38
TM$_{111}$	8.179	0.22	2.09	2.29	0.56	0.56
TE$_{111}$	8.179		2.09	0.70	1.57	0.56
TM$_{210}$	8.886		2.98	3.53	0.84	1.91
TE$_{102}$	8.947		5.38	1.70	0.49	2.76

(a)

Mode	k_0 [cm^{-1}] (Exact)	|Error| [%] Higher order FEM		
		29 Unknowns	240 Unknowns	756 Unknowns
TE$_{101}$	5.236	0.42	0.74×10^{-3}	0.17×10^{-6}
TM$_{110}$	7.025	0.53	0.74×10^{-3}	0.17×10^{-6}
TE$_{011}$	7.551	0.66	0.74×10^{-3}	0.17×10^{-6}
TE$_{201}$	7.551	2.38	0.20×10^{-1}	0.49×10^{-4}
TM$_{111}$	8.179	0.56	0.74×10^{-3}	0.17×10^{-6}
TE$_{111}$	8.179	0.56	0.74×10^{-3}	0.17×10^{-6}
TM$_{210}$	8.886	1.91	0.15×10^{-1}	0.35×10^{-4}
TE$_{102}$	8.947	2.76	0.26×10^{-1}	0.62×10^{-4}

(b)

The next example is a cubical air-filled metallic cavity 0.5 cm on a side. Fig. 6.2 shows a plot of the percentage error in calculating k_0 of the dominant degenerate eigenmodes against the number of unknowns, for the low-order FEM models with small rectangular bricks [30] and small tetrahedra [30], and three higher order models. In the first higher order solution, the cavity is represented by a single (entire-domain) trilinear hexahedron with the field-expansion polynomial orders being varied from $N_u = N_v = N_w = 2$ to $N_u = N_v = N_w = 7$ (p-refinement). The other two higher order solutions, using 8-element and 27-element uniform meshes, are shown to indicate the model behavior when the number of elements is increased as well, which corresponds to an h-refinement of the model. We observe great superiority of higher order FEM solutions over low-order ones. We also note that finer higher order meshes result in a worse accuracy to number-of-unknowns ratio as compared to coarser meshes in this example. Generally, optimal modeling is achieved by keeping the elements as large as possible – of course, within certain limits. Based on many numerical experiments, we have adopted 2λ to be the maximal dimension of finite elements and the general limit in the FEM procedure beyond which the structure is subdivided into smaller, but still large-domain, optimal elements (note that the corresponding low-order FEM limit is 0.1λ). The same limit holds for higher order MoM modeling [4-7].

Somewhat more complex cavities are analyzed next. First, consider a half-filled 1 cm × 0.1 cm × 1 cm rectangular metallic cavity with a dielectric filling of relative permittivity $\varepsilon_r = 2$ extending from $z = 0.5$ cm to $z = 1$ cm (Fig. 6.8). Percentage errors in computation of k_0 for the first six modes are shown in Table 6.3. The results obtained by the higher order FEM using two trilinear hexahedral finite elements, as indicated in Fig. 6.8, are compared against a low-order tetrahedral-mesh FEM solution [30]. The number of unknowns in the higher order model is kept by roughly an order of magnitude smaller than that with the low-order model, and excellent accuracy is achieved. The exact numbers of unknowns and field-approximation polynomial orders used in both higher order hexahedra for different modes are also given in Table 6.3.
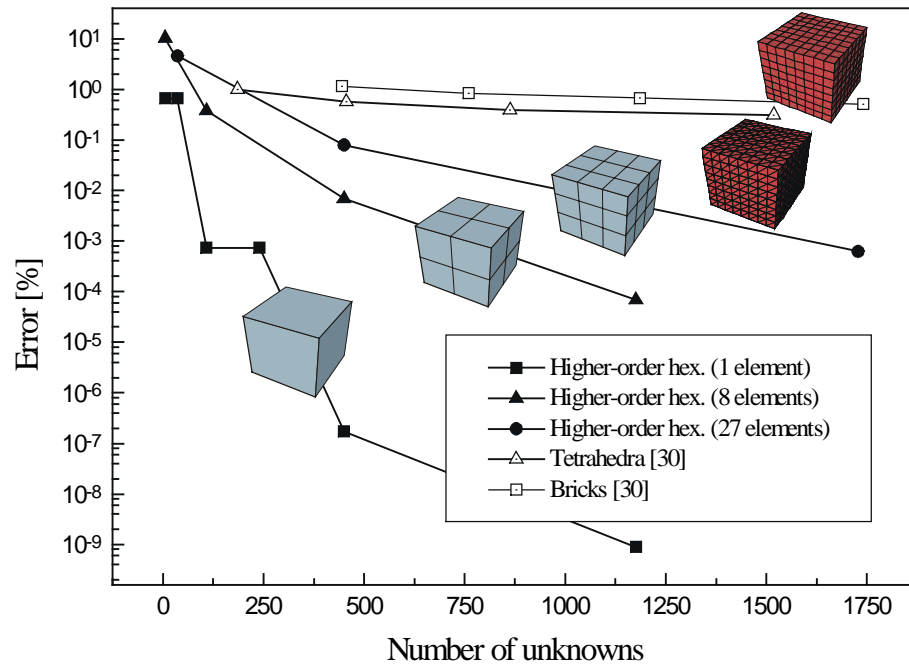
Fig. 6.7. Percentage error in calculating k_0 of the dominant degenerate eigenmodes of a cubical air-filled metallic cavity 0.5 cm on a side against the number of unknowns, for three higher order FEM models (with 1, 8, and 27 hexahedra) and two low-order FEM models (with small tetrahedra and bricks). Small-element meshes shown in the figure do not reflect the actual meshes used in the corresponding examples.
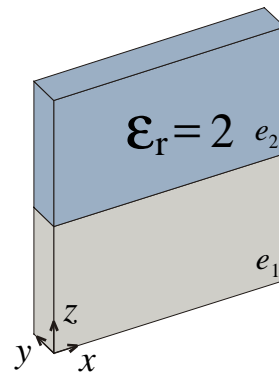
Fig. 6.8. A half-filled 1 cm × 0.1 cm × 1 cm rectangular cavity, modeled by two trilinear hexahedral finite elements.

Table 6.3. Percentage error of k_0 for the cavity in Fig. 6.8: a higher order two-element solution and a low-order tetrahedral-mesh solution.

Mode	Exact k_0 [cm^{-1}]	|Error| [%]		Numerical parameters of the higher order model	
		Tetrahedra [30] 192 Unknowns	Higher order 20-25 Unknowns	Exact Number of Unknowns	Orders N_u-N_v-N_w
TEz$_{101}$	3.538	0.11	0.004	21	4-1-4
TEz$_{201}$	5.445	0.10	0.04	20	5-1-3
TEz$_{102}$	5.935	0.32	1.07	21	4-1-4
TEz$_{301}$	7.503	0.04	0.2	25	6-1-3
TEz$_{203}$	7.633	0.97	0.9	25	6-1-3
TEz$_{103}$	8.096	0.50	0.58	21	4-1-4

Next, consider an empty rectangular cavity with a metallic ridge, shown in Fig. 6.9. Table 6.4 shows the computed results for the free-space wave numbers, k_0, of the cavity (there is no exact analytical solution to this problem). Two higher order solutions are presented with the cavity modeled by 3 and 5 trilinear hexahedra, shown in Fig. 6.10(a) and (b), and the resulting total numbers of unknowns 68 and 81, respectively. The adopted field-approximation polynomial orders in individual directions are indicated in the figures. Shown in Table 6.4 are also the results obtained by two low-order tetrahedral-mesh FEM models [30], with 267 and 671 unknowns, respectively. A good agreement between the higher order and low-order FEM results is observed, the reduction of the number of unknowns with the higher order FEM being again by up to an order of magnitude when compared to the low-order FEM. We note also a very effective 3-element hexahedral FEM modeling of this nonstandard shape in the mesh in Fig. 6.10(a). However, the 5-element model in Fig. 6.10(b) provides better accuracy at predicting the fields in the vicinity of the ridge and better overall accuracy of the results.
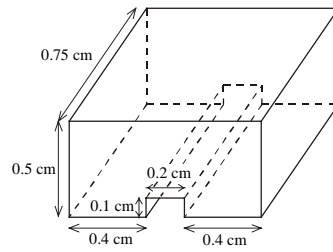
Fig. 6.9. An air-filled rectangular cavity with a metallic ridge.

Table 6.4. Computed k_0 for the cavity in Fig. 6.9: two higher order hexahedral-mesh solutions [models in Fig. 6.10(a) and (b)] and two low-order tetrahedral-mesh solutions.

	Calculated k_0 [cm^{-1}]			
	Tetrahedra [30]		Higher order FEM	
Mode No.	267	671	68	81
	Unknowns	Unknowns	Unknowns	Unknowns
1	4.941	4.999	5.083	5.088
2	7.284	7.354	7.572	7.471
3	7.691	7.832	8.207	7.903
4	7.855	7.942	8.479	7.967
5	8.016	7.959	8.743	8.019
6	8.593	8.650	9.108	9.001
7	8.906	8.916	9.458	9.111
8	9.163	9.103	10.04	9.169
9	9.679	9.757	10.22	10.08
10	9.837	9.927	10.69	10.37
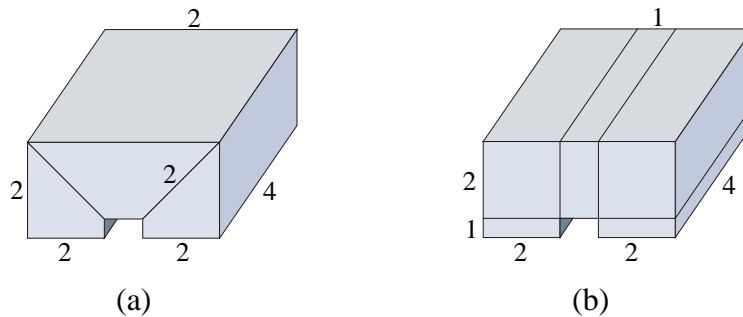
Fig. 6.10. Three-element (a) and five-element (b) higher order FEM hexahedral models of the cavity in Fig.4. The adopted field-approximation polynomial orders in individual directions are also indicated.

As an example of higher order FEM modeling of curved structures, Table 6.5(a) and (b) show the percentage error in calculating k_0 for first several modes of an empty spherical cavity, 1 cm in radius. The sphere is modeled by a single (entire-domain) curved hexahedron of the 2nd ($K = 2$) geometrical order [Table 6.5(a)] and 4th ($K = 4$) geometrical order [Table 6.5(b)], respectively, and field-approximation orders are varied from $N_u = N_v = N_w = 3$ to $N_u = N_v = N_w = 6$ in both solutions (*p*-refinement). For the 4th order geometrical model of a sphere, the control points not belonging to the spherical surface (hexahedron faces) are arranged to define an inscribed half-radius sphere. The results are compared with a low-order tetrahedral mesh FEM model [30]. We observe that the 2nd order geometrical approximation [Table 6.5(a)] with only 108 unknowns (64% less than with the low-order model) yields very good results for the first 8 modes. The *p*-refinement improves the results for all modes, whereas an inherent geometrical error is always present. A considerable increase in accuracy for all modes is observed when the curved hexahedron of the 4th geometrical order is used [Table 6.5(b)]. Note that here as low as only 36 unknowns suffice for the analysis of lower modes.

Shown in Fig. 6.11 is the comparison of the convergence of the results for the dominant mode k_0 of a spherical cavity, with increasing the number of unknowns for the two higher order models with a single curved hexahedron (field-expansion orders are varied from 3 to 7 in all directions) and a low-order tetrahedral-mesh solution [33]. The figure demonstrates great numerical advantages of the higher order FEM over the low-order FEM in this case, the number of unknowns for 1% accuracy with the low-order model (1840) being 17 times that (108) with both higher order models. We again observe a significant additional improvement in accuracy as a result of using geometrical modeling of the 4th order instead of the 2nd order geometrical modeling. In other words, it is impossible to *p*-refine the higher order model with the 2nd geometrical order below about 1% error in calculating k_0 due to the inherent geometrical error of the model, whereas the *p*-refinement in the model with the 4th geometrical order brings the analysis error quickly down to a fraction of a percent.

Table 6.5. Error of k_0 comparison for the eigenvalue analysis of an air-filled spherical cavity, 1 cm in radius: higher order single-element FEM modeling with 2nd order geometrical approximation (a) and 4th order geometrical approximation (b), and a low-order tetrahedral-mesh fem solution.

		|Error| [%]			
		Tetrahedra [30]	Higher order FEM with 2nd order geometry			
Unknowns		300	36	108	240	450
Mode	Exact k_0 [cm^{-1}]					
TM$_{010}$	2.744	2.04	4.60	1.00	0.94	0.91
TM$_{111,even}$		2.11	4.60	1.00	0.94	0.91
TM$_{111,odd}$		2.44	4.60	1.00	0.94	0.91
TM$_{021}$	3.870	2.02	6.85	1.39	0.89	0.85
TM$_{121,even}$		2.99	6.85	1.39	0.89	0.85
TM$_{121,odd}$		3.20	6.85	4.47	0.89	0.85
TM$_{221,even}$		4.34	15.57	4.47	1.39	1.09
TM$_{221,odd}$		4.59	15.57	4.47	1.39	1.09
TE$_{011}$	4.493	1.33	11.38	7.30	1.19	1.09
TE$_{111,even}$		0.47	11.38	7.30	1.19	1.09
TE$_{111,odd}$		1.25	11.38	7.30	1.19	1.09

(a)

| | | |Error| [%] | | | |
|---|---|---|---|---|---|---|
| | | Tetrahedra [30] | Higher order FEM with 4th order geometry | | | |
| Unknowns | | 300 | 36 | 108 | 240 | 450 |
| Mode | Exact k_0 [cm^{-1}] | | | | | |
| TM$_{010}$ | 2.744 | 2.04 | 2.79 | 0.78 | 0.10 | 0.25 |
| TM$_{111,even}$ | | 2.11 | 2.79 | 0.78 | 0.10 | 0.25 |
| TM$_{111,odd}$ | | 2.44 | 2.79 | 0.78 | 0.10 | 0.25 |
| TM$_{021}$ | 3.870 | 2.02 | 3.40 | 0.088 | 0.0067 | 0.02 |
| TM$_{121,even}$ | | 2.99 | 3.40 | 0.088 | 0.0067 | 0.02 |
| TM$_{121,odd}$ | | 3.20 | 3.40 | 0.44 | 0.0067 | 0.02 |
| TM$_{221,even}$ | | 4.34 | 7.84 | 0.44 | 0.093 | 0.23 |
| TM$_{221,odd}$ | | 4.59 | 7.84 | 0.44 | 0.093 | 0.23 |
| TE$_{011}$ | 4.493 | 1.33 | 4.21 | 3.79 | 1.08 | 0.28 |
| TE$_{111,even}$ | | 0.47 | 4.21 | 3.79 | 1.08 | 0.28 |
| TE$_{111,odd}$ | | 1.25 | 4.21 | 3.79 | 1.08 | 0.28 |

(b)
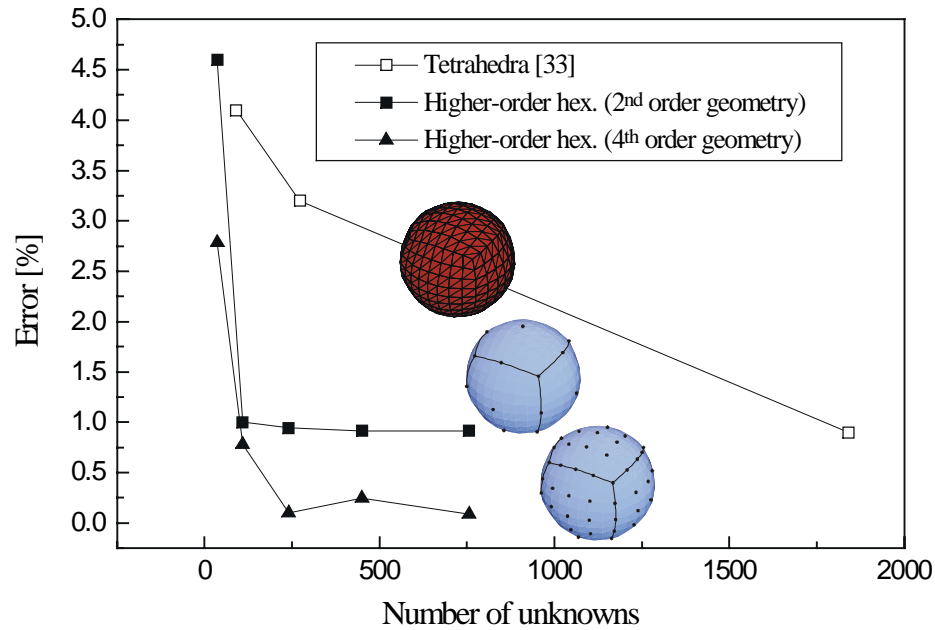
Fig. 6.11. Comparison of two higher order FEM solutions (single-element models of the 2nd and 4th geometrical orders) and a low-order tetrahedral-mesh solution, for the dominant mode k_0 of a spherical cavity, 1 m in radius, against the number of unknowns. Tetrahedral mesh shown in the figure does not reflect the actual mesh used in the corresponding example.

We notice a non-monotonic (oscillating) error decrease in the low-error region with the 4th order geometrical model in Fig. 6.11 [see also Table 6.5(b)]. This oscillation falls in the error margin for the particular mode and the particular numerical discretization of field equations in this example. However, the average error for all eleven calculated modes in Table 6.5(b) that corresponds to the points for the 4th order model in Fig. 6.11 is 4.3%, 1.4%, 0.34%, 0.19%, and 0.15%, respectively, as shown (by the second curve) in Fig. 6.12. Note that this (or similar) average error, which indeed decreases monotonically when using p-refinement, is actually relevant for "dialing" accuracy, i.e., for determining minimal field expansion orders needed for the specified level of desired accuracy or acceptable uncertainty of the results, in practical implementations. Also shown in Fig. 6.12 are the same average errors obtained using the 2nd order geometrical model (the first curve), and the

4th order geometrical model with the inner control points defining an inscribed cube having the length of the spatial diagonal equal to the sphere's radius (the third curve). In addition to all curves being monotonically decreasing when *p*-refinement is applied, from the figure we verify the superiority of the 4th order geometrical models (as compared to the 2nd order model) and the importance of the meshing considerations regarding the higher order elements, discussed in Section 3.4 (see Fig. 3.7). Note that the 4th order geometrical model with the inner points on a cube, having less distorted coordinate lines throughout its volume and thus being able to represent the fields more accurately, yields by an order of magnitude smaller average error in the low-error region than the model with the inner points placed on a sphere.
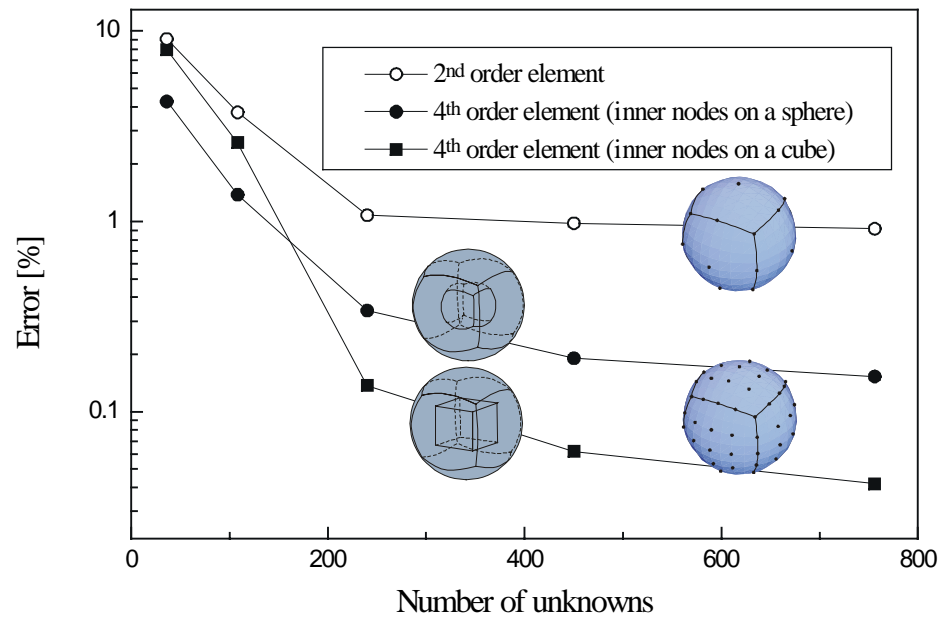
Fig. 6.12. Comparison of three higher order single-element FEM solutions; average errors for the first eleven modes, k_0, of a spherical cavity against the number of unknowns.

To further investigate numerical properties of different higher order models of a sphere, we show in Fig. 6.13 the comparison of the results in calculating the dominant mode k_0 for a spherical cavity, modeled by 1, 8, and 27 triquadratic ($K = 2$) hexahedral

elements, with the field-approximation polynomial orders being varied from 2 to 6, from 1 to 4, and from 1 to 3, respectively, in all directions. The models with 8 and 27 elements correspond to the combined *hp*-refinement of the solution. We observe the following: for obtaining a 1%-accuracy solution, the single-element model is optimal (in terms of the required number of unknowns); 0.5% accuracy, however, cannot be achieved by a single-element model (of the 2nd geometrical order) and *p*-refinement alone, but *h*-refinement (8-element model) has to be employed as well, finally, if 0.1% accuracy is desired, further *hp*-refinement, with 27-element model, is needed. On the other hand, we also note that approximately 0.1% accuracy can be achieved using as little as 240 unknowns with a single-element model of the 4th geometrical order (see Fig. 6.11), whereas more than 1728 unknowns and at least 27 elements are necessary for getting the same level of accuracy if elements of the 2nd geometrical order (triquadratic hexahedra) are used (Fig. 6.13).
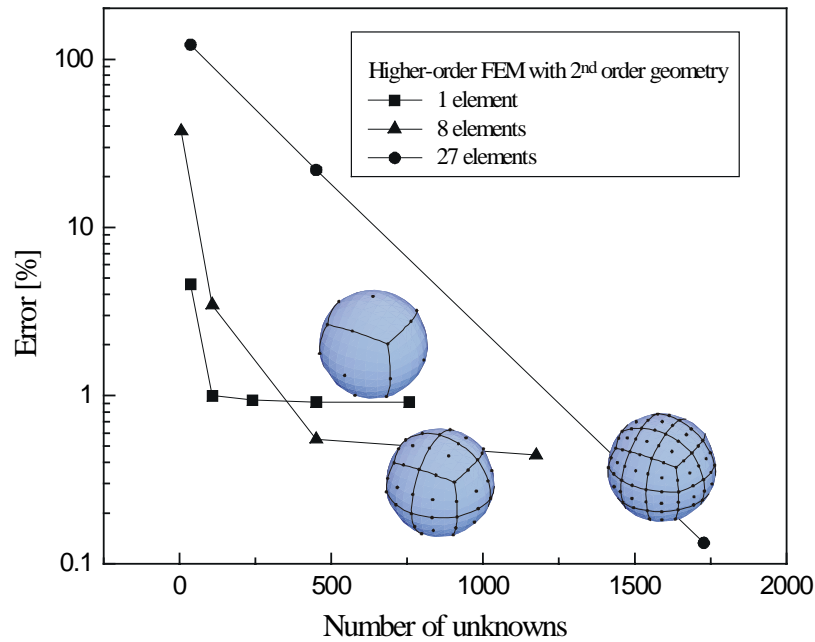

Fig. 6.13. Percentage error in higher order FEM computation of the dominant mode k_0 for a spherical cavity, modeled by 1, 8, and 27 triquadratic ($K = 2$) hexahedral elements, with the field-approximation polynomial orders ranging from 2 to 6, from 1 to 4, and from 1 to 3, respectively, in all three parametric coordinates within individual elements.

Shown in Fig. 6.14 are the *E*-field distributions for the first nine modes of the air-filled spherical cavity, at the central horizontal cross-section (see, for instance, Fig. 3.7). The field distributions in the figure are reconstructed using the eigenvectors obtained from the higher order FEM solution of the eigenvalue problem modeled by a single 2nd order hexahedron with $N_u = N_v = N_w = 3$. The maximal field intensities in the given cross section are normalized to one. Note that all modal field distributions are indeed divergence-free. Some of the mode patterns are also identical, only rotated $90°$ in space from each other (e.g., the first three modes and the second three modes), which is in agreement with the analytical solutions given in [71]. Additionally, the modal patterns for the three lowest modes obtained by higher order FEM are in excellent agreement with the analytically obtained patterns for the dominant modes of the spherical cavity, shown in [71].

Finally, we investigate the condition numbers of the global matrices resulting from higher order FEM eigenvalue analysis of the rectangular cavity of normalized dimensions $1 \times 0.5 \times 0.75$. Shown in Table 6.6 are the condition numbers of global [*B*]-matrix, from the generalized eigenvalue problem given by (101), which are used as indicators of the matrix condition numbers that the proposed higher order hexahedral TVFEs lead to[14], and they are compared with the same indicators obtained using five different tetrahedral TVFEs published in [47]. A 130-element tetrahedral mesh was used in the five FEM solutions shown for comparison, whereas 1-4 and 6 hexahedral elements were used (see Fig. 6.15), respectively, in the hexahedral FEM solution. As seen from the table, all tetrahedral TVFEs are of the order 1.5 (which, according to the adopted mixed-order element nomenclature [47], corresponds to the LT/QN elements), except for the Whitney elements, being of the order 0.5 [which correspond to the constant tangential/linear normal (CT/LN) elements]. Hence, to make the comparison fair, the field-expansion with $N_u = N_v = N_w = 2$, being the

---

[14] Note that the [*A*]-matrix in the generalized eigenvalue problem is singular.

LT/QN expansion, was chosen for the hexahedral elements. The condition numbers are calculated as the ratio of the maximum to the minimum eigenvalue.
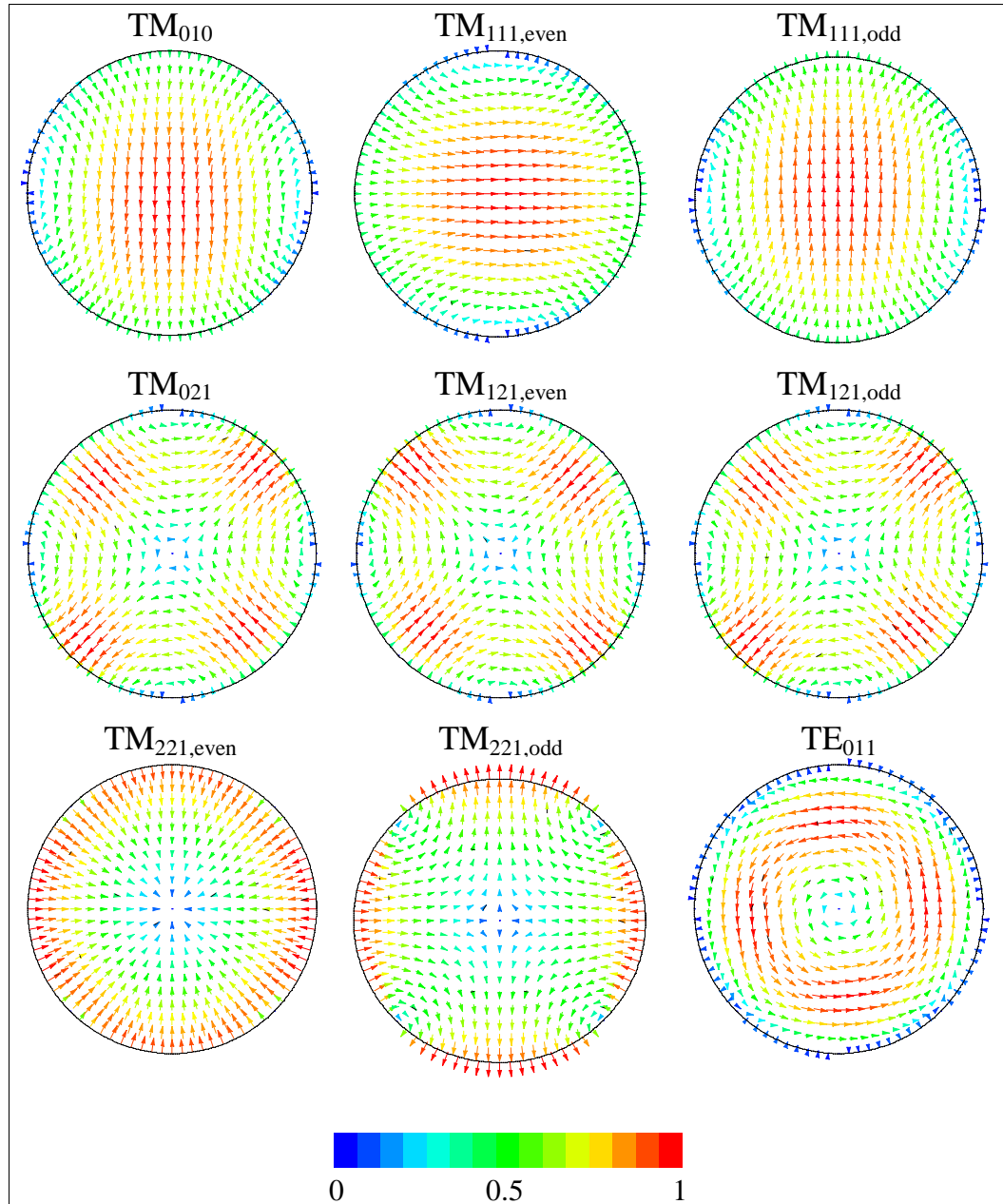

Fig. 6.14. *E*-field modal distributions for the lowest nine modes of the air-filled spherical cavity, at the central horizontal cross-section ($w = 0$).

We can conclude from the table that the condition number for the hexahedral elements rises quickly as the number of elements is increased, thus verifying the inherent down-point of the underlying higher order hierarchical scheme. However, having in mind that, for instance, the 4-element hexahedral FEM solution yields lower error in calculating k_0 for the dominant mode then the tetrahedral Whitney-element FEM solution [30] (0.38% as compared to 0.44%, respectively), the corresponding hexahedral TVFEs condition number, 882, compares well to the condition numbers obtained using the alternative four higher order tetrahedral TVFEs (given in the table), for which the accuracy of the solution was not available for comparison.

Table 6.6. Condition numbers for the global matrices resulting from FEM analysis of the rectangular cavity of normalized dimensions $1 \times 0.5 \times 0.75$; comparison of the higher order hexahedral TVFEs and five different tetrahedral TVFEs from [47].

TVFE		Type	Element order	Condition number
Whitney	[76]	/	0.5	8
Peterson	[42]	Interpolatory	1.5	2173
Graglia	[37]	Interpolatory	1.5	684
Andersen	[46]	Hierarchical	1.5	1834
Webb	[39]	Hierarchical	1.5	4238
	1-element			12
	2-elements			116
Hexahedral	3-elements	Hierarchical	$N_u = N_v = N_w = 2$	213
	4-elements			882
	6-elements			2575

To investigate this matter further, shown in Fig. 6.15 are the condition numbers for the same problem obtained using new hexahedral finite elements with field-expansion orders ranging from $N_u = N_v = N_w = 2$ to $N_u = N_v = N_w = 5$ and different meshes with 1-4 and 6 elements in the FEM model. As seen from the figure, the condition number indeed rises very quickly as the field-expansion order is increased.

This conclusion implies the necessity of exercising additional care (e.g., employing the orthogonalization [48] and/or utilizing specifically designed solvers [49]) if iterative techniques are to be employed in solving of the large sparse FEM systems arising in the analysis of complex real-world EM problems.
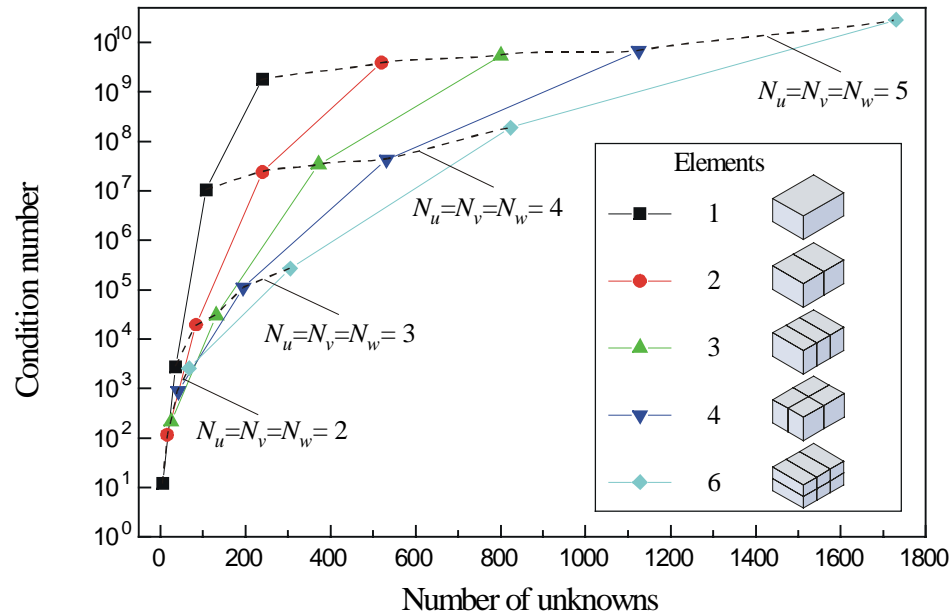
Fig. 6.15. Condition numbers against the number of unknowns for the FEM analysis of the rectangular ($1 \times 0.5 \times 0.75$) cavity using higher order hexahedral finite elements and different meshes.

6.4. Results of open-region problem analyses; characterization of scatterers

A quantity often used to characterize a scatterer in the 3-D case is the radar cross-section (RCS) defined by

$$\sigma = \lim_{r \to \infty} 4\pi r^2 \frac{|\boldsymbol{E}^{\mathrm{sc}}(r)|^2}{|\boldsymbol{E}^{\mathrm{inc}}(r)|^2}, \tag{168}$$

E^{inc} being the electric field of the incident plane wave. In this Section, we present several numerical examples in computation of the RCS for different scatterers using the new FEM method and the technique described in Section 5.3.

As the first example, consider a square-plate metallic scatterer 0.3λ on the side. Shown in Fig. 6.16 is the FEM model of the scatterer comprised of only 12 hexahedral elements, 10 of which are of the 2nd geometrical order (to conform to the introduced fictitious absorbing spherical boundary 0.6λ in radius), and the remaining 2 are of the 1st geometrical order (the brick-like elements situated on the top and on the bottom of the plate). The 1st order ABC is imposed on the spherical surface.
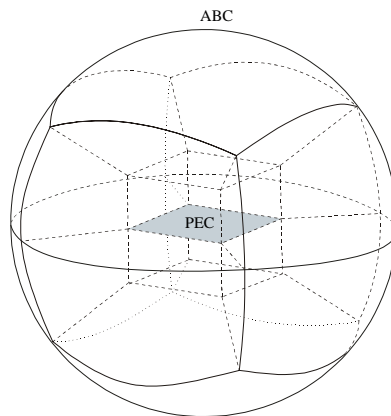
Fig. 6.16. The 12-element higher order hexahedral FEM mesh for computation of the RCS from a square-plate metallic scatterer 0.3λ on the side; the model is comprised of 10 curved ($K = 2$) and 2 brick-like trilinear ($K = 2$) hexahedra.

Fig. 6.17 shows the normalized RCS computed by the higher order FEM (for the azimuth of incidence, $\phi = 0$, and the range of different elevations of the incident wave, θ), and compares the results to those obtained by the low-order tetrahedral FEM solution [60]. The figure shows the computed backscatter RCS for both E_θ and E_ϕ incident polarizations. In the higher order FEM solution, the field-expansion order used in all 12 elements was $N_u = N_v = N_w = 5$, resulting in the total of 4720 unknowns, whereas approximately ten times as many unknowns were employed in the low-order

FEM solution. The 1ˢᵗ order ABC was imposed to terminate the meshes in both approaches. As seen from the figure, a good agreement between the two solutions can be observed in the high-field region, whereas the more significant discrepancy in the low-field region suggests the necessity of utilizing better geometrical approximations in the higher order FEM model. Note also that the higher order solution yields higher RCSs, which implies that, the better ABC or an alternative (more accurate) termination technique (e.g., FEM-MoM or different hybrid approach) could improve the accuracy of the method.
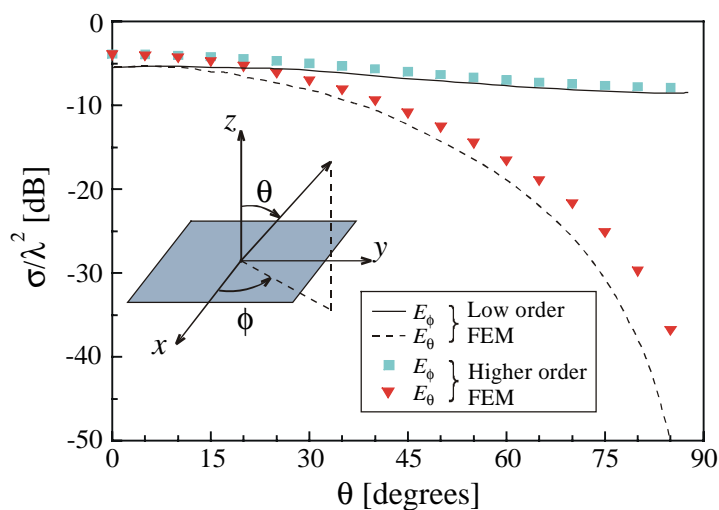
Fig. 6.17. Backscatter RCS of a $0.3\lambda \times 0.3\lambda$ thin metallic plate for two cases of incident polarizations; comparison of the higher order FEM solution and the low-order FEM solution [60].

The convergence of the higher order FEM method in this example is illustrated in Fig. 6.18, which shows the computed RCS for the E_θ polarization of the incident wave, using the same geometrical model shown in Fig. 6.16 and different field expansion orders, ranging from $N = 2$ to $N = 5$ ($N = N_u = N_v = N_w$). We can conclude from the figure that the higher order FEM solution indeed approaches, quickly and steadily, the low-order solution (used as a reference in Fig. 6.17) from "above" as the number of unknowns is increased in the process of p-refinement.
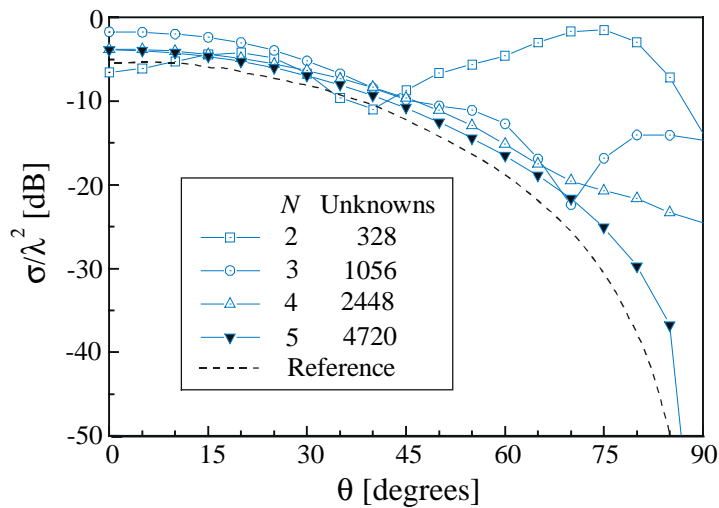
Fig. 6.18. Backscatter RCS of a $0.3\lambda \times 0.3\lambda$ thin metallic plate computed by the higher order FEM for the E_θ incidence; convergence of the method with increasing the number of unknowns via *p*-refinement.

Next consider the scattering from a metallic cube of side-length *a*. Shown in Fig. 6.19 is the hexahedral mesh comprised of 6 identical elements with 2nd order in geometry, used for analysis by the higher order FEM, the radius of the fictitious absorbing spherical boundary on which the 1st order ABC is enforced being $r = 2a$. Fig. 6.20 shows the backscatter RCS of the cube, at normal incidence, as a function of the normalized edge length, computed by the higher order FEM and compares the results to the low-order FEM solution [60]. The field-expansion order employed in the higher order model was $N_u = N_v = N_w = 6$ in all 6 hexahedral elements, yielding a total of 3900 unknowns in the final system, whereas in the low-order tetrahedral model as many as 33000 unknowns were used for the discretization of the computational domain at the higher end of the spectrum. A conformal (cubical) mesh termination boundary with the 2nd order ABC was used in the low-order FEM model. The boundary was placed 0.15λ away from the edge of the cube. As seen from the figure, in the low-frequency region the results obtained by the higher order FEM compare reasonably well to the FEM results obtained in [60], whereas a pronounced

discrepancy arises in the higher frequency region. Note, however, that both conformal frequency-adaptive boundary and an improved boundary condition were used in the low-order FEM model, and that the model employed up to an order of magnitude larger number of unknowns than the higher order model.

Fig. 6.19. The 6-element higher order hexahedral FEM mesh for computation of the RCS from a cube; the curved hexahedra are of the 2nd ($K = 2$) geometrical orders.

As the final example consider the scattering from a sphere of radius a. Fig. 6.21 shows the 6-element hexahedral mesh comprised of 2nd order curved hexahedra, used for analysis by the higher order FEM. The 1st order ABC was, again, enforced on the fictitious absorbing spherical boundary having the radius $r = 2a$. Shown in Fig. 6.22 is the backscatter RCS of the sphere, at normal incidence, as a function of the normalized radius, computed by the higher order FEM and compares the results to the analytical solution (MIE's series) [71]. The field-expansion order employed in the FEM model was $N_u = N_v = N_w = 6$ in all curved elements, yielding a total of 3900 unknowns in the final system. As seen from the figure, in the low-frequency region the results obtained by the higher order FEM closely follow the analytical results. In order to obtain more accurate solutions in the higher frequency region, an improved geometrical model (e.g., with 4th geometrical order hexahedra and/or frequency-

adaptive spherical boundary) as well as a better mesh termination technique (as suggested in the first example) should be used.

Fig. 6.20. Backscatter RCS of a metallic cube at normal incidence; comparison of the higher order FEM solution and the low-order FEM solution [60].
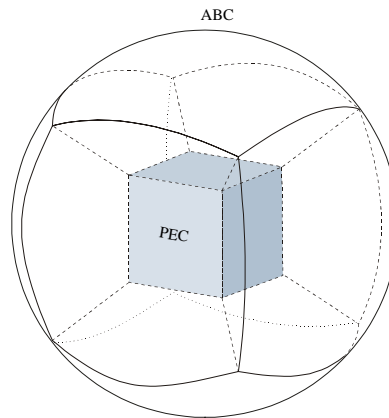

Fig. 6.21. The 6-element higher order hexahedral FEM mesh for computation of the RCS from a sphere; the curved hexahedra are of the 2nd ($K = 2$) geometrical orders.
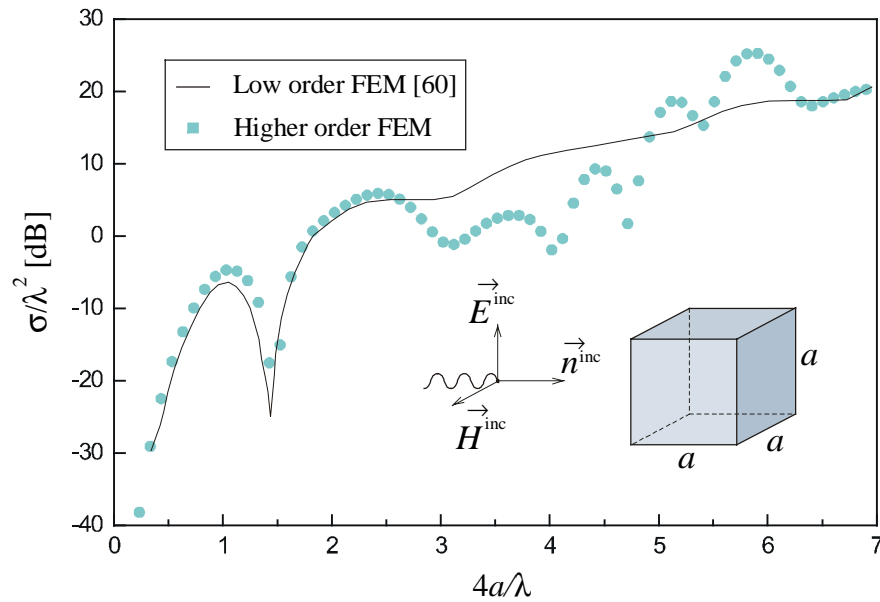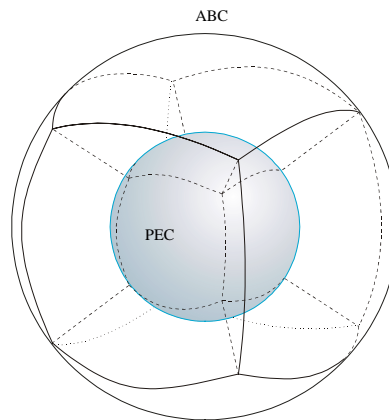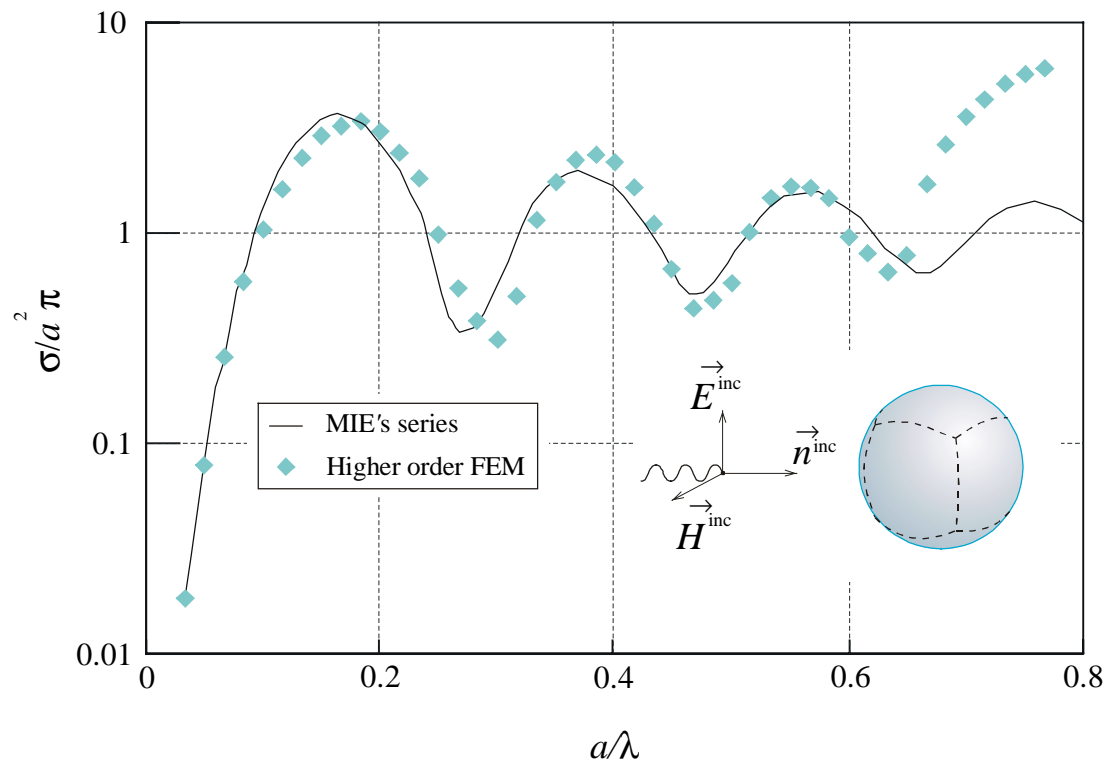
Fig. 6.22. Backscatter RCS of a metallic sphere at normal incidence; comparison of the higher order FEM solution and the analytical solution [71].

7. CONCLUSION

This thesis has presented a novel higher order finite element technique for 3-D electromagnetic modeling and has presented its implementation in eigenvalue analysis of arbitrary 3-D electromagnetic cavities and in analysis of 3-D scatterers. The technique represents a Galerkin-type method employing hierarchical curl-conforming vector basis functions of higher $(1 - 10)$ polynomial orders defined in generalized curved hexahedra of higher $(1 - 4)$ geometrical orders. The elements can be as large as $2\lambda \times 2\lambda \times 2\lambda$ (which is 20 times the traditional low-order modeling discretization limit of $\lambda/10$ in each dimension).

The new technique enables excellent field-distribution modeling; it has been demonstrated that entire rectangular and spherical cavities can be modeled very accurately by a single large hexahedral finite element with polynomial field-approximation basis functions of high orders. The method also enables excellent curvature modeling; it has been demonstrated that a sphere, which is often considered as an example of difficulty with modeling of curvature by many researchers, can be equally efficiently modeled as a cube. The flexibility of the new technique has allowed for a very effective modeling of a cavity with a dielectric loading and a cavity with a metallic ridge by means of only a few large finite elements. All the presented examples in the cavity analyses have shown excellent properties of higher order finite elements in the context of the *p*-refinement of solutions, for models with both flat and curved surfaces. The results obtained by the higher order FEM are compared with the analytical solutions and with the numerical results obtained by different low-order FEM techniques, which utilize electrically small triangular prisms, bricks, and tetrahedra, respectively, as finite elements. It has been observed that the presented

technique offers considerably improved accuracy, as well as significantly faster convergence as the number of unknowns increases. The reduction in the number of unknowns is by an order of magnitude when compared to first-order solutions.

Although the accuracy of the new technique has been impaired by implementation of the simple 1st order ABC in the analysis of scatterers, the validity of the method and excellent convergence properties of the novel higher order basis functions have been verified throughout the given examples.

The higher order large-domain FEM technique, presented in this thesis, indeed represents a novelty in the computational electromagnetics community and, by all means, belongs to the mainstream of the recently conducted research. However, while the low-order small-domain modeling (having been rather extensively investigated in the past few decades) is heavily supported by the solid existing mathematical infrastructure (e.g., commercially available tetrahedral mesh generators, directly applicable absorbing boundary conditions, specially developed matrix pre-conditioners and sparse matrix solvers), the corresponding support and techniques have yet to be developed for the higher order modeling. Hence, the author's main efforts for future research will be in this direction.

REFERENCES

1   T. J. Brazil, "Simulating circuits and devices," *IEEE Microwave Magazine*, Vol. 4, No. 1, March 2003, pp. 42-50.

2   R. F. Harrington, *Field Computation by Moment Methods*, New York: The Macmillan Company, 1968.

3   B. D. Popović and B. M. Kolundžija, *Analysis of metallic antennas and scatterers*, London, U.K.: The Institution of Electrical Engineers, 1994.

4   B. M. Notaroš and B. D. Popović, "General entire-domain method for analysis of dielectric scatterers," *IEE Proceedings - Microwaves, Antennas and Propagation*, Vol. 143, (6), December 1996, pp. 498-504.

5   B. M. Notaroš and B. D. Popović, "General entire-domain Galerkin method for analysis of wire antennas in the presence of dielectric bodies," *IEE Proceedings - Microwaves, Antennas and Propagation*, February 1998, Vol. 145, (1), pp. 13-18.

6   B. M. Notaroš and B. D. Popović, "Large-domain integral-equation method for analysis of general 3D electromagnetic structures," *IEE Proceedings - Microwaves, Antennas and Propagation*, Vol. 145, (6), December 1998, pp. 491-495.

7   B. M. Notaroš, B. D. Popović, J. Peeters Weem, R. A. Brown, and Z. Popović, "Efficient large-domain MoM solution to electrically large practical EM problems," *IEEE Transactions on Microwave Theory and Techniques*, January 2001, Vol. 49, (1), pp. 151-159.

8   B. M. Kolundžija and V. V. Petrović, "Comparison of MoM/SIE, MoM/VIE and FEM Based on Topological Analysis of Two Canonical Problems," *IEEE AP-S International Symposium*, Atlanta, June 1998.

9   J. M. Jin, *The finite element method in Electromagnetics*, New York: Wiley, 1993.

10   P. P. Silvester and R. L. Ferrari, *Finite elements for electrical engineers*, Cambridge, U.K.: Cambridge University Press, 1996.

11   M. Salazar-Palma, T. P. Sarkar, L. E. Garcia-Castillo, T. Roy, and A. Djordjević, *Iterative and self-adaptive finite elements in electromagnetic modeling*, Boston: Artech House, 1998.

12   J. L. Volakis, A. Chatterjee, and L. C. Kempel, *Finite Element Method for Electromagnetics*, New York: IEEE Press, 1998.

13   X. Yuan, D. R. Lynch, and K. Paulsen, "Importance of normal field continuity in inhomogeneous scattering calculations," *IEEE Transactions on Microwave Theory and Techniques*, Vol. 39, No. 4, April 1991, pp. 638-642.

14   J. C. Nedelec, "Mixed finite elements in R^3," *Numerische Mathematik*, Vol. 35, 1980, pp. 315-341.

15   J. C. Nedelec, "A new family of mixed finite elements in R^3," *Numerische Mathematik*, Vol. 50, 1986, pp. 57-81.

16   A. Bossavit, "A rationale for 'edge-elements' in 3-D fields computations," *IEEE Transactions on Magnetics*, Vol. 24, January 1988, pp. 74-79.

17   A. Bossavit, "Whitney forms: a class of finite elements for three-dimensional computations in electromagnetism," *IEEE Proceedings*, Vol. 135, Pt. A, No. 8, November 1988, pp. 493-500.

18   J. P. Webb, "Edge elements and what they can do for you," *IEEE Transactions on Magnetics*, Vol. 29, No. 2, March 1993, pp. 1460-1465.

19   A. F. Peterson and D. R. Wilton, "Vector finite element formulation for scattering from two-dimensional heterogeneous bodies," *IEEE Transactions on Antennas and Propagation*, Vol. AP-42, March 1994, pp. 357-365.

20   M. M. Ilić, B. D. Popović, and V. V. Petrović, "Analysis of efficiency of the finite element method using higher order elements in calculating the reflection coefficients," *XLIII ETRAN Conference*, Zlatibor, Yugoslavia, 1999.

21   M. M. Ilić, "Higher order FEM analysis of electromagnetic fields in inhomogeneous media," M.S. Thesis, Department of Electrical Engineering, University of Belgrade, Yugoslavia, January 2000 (in Serbian language).

22   M. M. Ilić and B. M. Notaroš, "Trilinear hexahedral finite elements with higher order polynomial field expansions for hybrid SIE/FE large-domain electromagnetic modeling," *IEEE Antennas & Propagation International Symposium and USNC/URSI Meeting*, Boston, USA, 2001, pp. III. 192-195.

23   M. M. Ilić and B. M. Notaroš, "Entire-domain and large-domain finite element analysis of 3-D electromagnetic cavities," *Sixth international workshop on finite*

elements for microwave engineering antennas, circuits and devices, Chios, Greece, 2002, Book of abstracts p. 30.

24 M. M. Ilić and B. M. Notaroš, "Computation of 3-D electromagnetic cavity resonances using hexahedral finite elements with hierarchical polynomial basis functions," 2002 *IEEE Antennas and Propagation International Symposium Digest*, June 16-21, 2002, San Antonio, TX, USA, pp. IV. 682-685.

25 M. M. Ilić and B. M. Notaroš, "Higher order hierarchical curved hexahedral vector finite elements for electromagnetic modeling," *IEEE Transactions on Microwave Theory and Techniques*, Vol. 51, No. 3, March 2003, pp.1026-1033.

26 V. V. Petrović and B. D. Popović, "Optimal FEM solutions of one-dimensional EM problems," *International Journal of Numerical Modeling*, 2001, pp. 14:49-68.

27 J. P. Webb, "The finite element method for finding modes of dielectric-loaded cavities," *IEEE Transactions on Microwave Theory and Techniques*, Vol. MTT-33, No. 7, July 1985, pp. 635-639.

28 J. P. Webb, "Efficient generation of divergence-free fields for the finite element analysis of 3-D cavity resonances," *IEEE Transactions on Magnetics*, Vol. 24, No. 1, January 1988, pp. 162-165.

29 T. Ozdemir and J. L. Volakis, "Triangular prisms for edge-based vector finite element analysis of conformal antennas," *IEEE Transactions on Antennas and Propagation*, Vol. 45, No. 5, May 1997, pp. 788-797.

30   A. Chatterjee, J. M. Jin and J. L. Volakis, "Computation of cavity resonances using edge-based finite elements," *IEEE Transactions on Microwave Theory and Techniques*, Vol. 40, No. 11, November 1992, pp. 2106-2108.

31   K. Sakiyama, H. Kotera, and A. Ahagon, "3-D electromagnetic field mode analysis using finite element method by edge element," *IEEE Transactions on Magnetics*, Vol. 26, No. 5, September 1990, pp. 1759-1761.

32   J. S. Wang and N. Ida, "Eigenvalue analysis in anisotropically loaded electromagnetic cavities using "edge" finite lements," *IEEE Transactions on Magnetics*, Vol. 22, No. 2, March 1992, pp. 1438-1441.

33   J. S. Wang and N. Ida, "Eigenvalue analysis in electromagnetic cavities using divergence free finite lements," *IEEE Transactions on Magnetics*, Vol. 27, No. 5, September 1991, pp. 3978- 3981.

34   J. M. Jin and J. L. Volakis, "Electromagnetic scattering by and transmission through a three dimensional slot in a thick conducting plane," *IEEE Transactions on Antennas and Propagation*, Vol. 39, No. 4, April 1991, pp. 543-550.

35   C. W. Crowley, P. P. Silvester, and J. Hurwitz, "Covariant projection elements for 3D vector field problems," *IEEE Transactions on Magnetics*, Vol. 24, No. 1, January 1988, pp. 397-400.

36   J. S. Wang and N. Ida, "Curvilinear and higher order 'edge' finite elements in electromagnetic field computation," *IEEE Transactions on Magnetics*, Vol. 29, No. 2, March 1993, pp. 1491-1493.

37   R. D. Graglia, D. R. Wilton, and A. F. Peterson, "Higher order interpolatory vector bases for computational electromagnetics," *IEEE Transactions on Antennas and Propagation*, Vol. 45, No. 3, March 1997, pp. 329-342.

38   R. D. Graglia, D. R. Wilton, and A. F. Peterson, and I. L. Gheorma, "Higher order interpolatory vector bases on prism elements," *IEEE Transactions on Antennas and Propagation*, Vol. 46, No. 3, March 1998, pp. 442-450.

39   J. P. Webb and B. Forghani, "Hierarchal scalar and vector tetrahedra," *IEEE Transactions on Magnetics*, Vol. 29, No. 2, March 1993, pp. 1495-1498.

40   J. Wang and J. P. Webb, "Hierarchal vector boundary elements and *p*-adaption for 3-D electromagnetic scattering," *IEEE Transactions on Antennas and Propagation*, Vol. 45, No. 12, December 1997, pp. 1869-1879.

41   T. V. Yioultsis and T. D. Tsiboukis, "Development and implementation of second and third order vector finite elements in various 3-D electromagnetic field problems," *IEEE Transactions on Magnetics*, Vol. 33, No. 2, March 1997, pp. 1812-1815.

42   J. S. Savage and A. F. Peterson, "Higher order vector finite elements for tetrahedral cells," *IEEE Transactions on Microwave Theory and Techniques*, Vol. 44, No. 6, June 1996, pp. 874-879.

43   J. F. Lee, D. K. Sun, and Z. J. Csendes, "Tangential vector finite elements for electromagnetic field computation," *IEEE Transactions on Magnetics*, 1991, Vol. 27, pp. 4032-4035

44   L. E. Garcia-Castillo, M. Salazar-Palma, T. K. Sarkar, and R. S. Adve, "Efficient solution of the differential form of Maxwell's equations in

rectangular regions," *IEEE Transactions on Microwave Theory and Techniques*, 1995, Vol. 43, pp. 647-654.

45   T. K. Sarkar, R. S. Adve, L. E. Garcia-Castillo, and M. Salazar-Palma: "Utilization of wavelet concepts in finite elements for an efficient solution of Maxwell's equations," *Radio Science*, Vol. 29, 1994, pp. 965-977.

46   L. S. Andersen and J. L. Volakis, "Development and application of a novel class of hierarchical tangential vector finite elements for electromagnetics," *IEEE Transactions on Antennas and Propagation*, Vol. 47, No. 1, January 1999, pp. 112-120.

47   L. S. Andersen and J. L. Volakis, "Condition numbers for various FEM matrices," *Journal of Electromagnetic Waves and Applications*, Vol. 13, 1999, pp. 1663-1679.

48   J. P. Webb, "Hierarchical vector basis functions of arbitrary order for triangular and tetrahedral finite elements," *IEEE Transactions on Antennas and Propagation*, Vol. 47, No. 8, August 1999, pp. 1244-1253.

49   Z. Huang and J. P. Webb, "Iterative solvers for hierarchical vector finite element analysis of microwave problems," *IEEE Transactions on Magnetics*, Vol. 37, No. 5, September 2001, pp. 3285-3288.

50   D. B. Davidson, "Implementation issues for three-dimensional vector FEM programs," *IEEE Antennas and Propagation Magazine*, Vol. 42, No. 6, December 2000, pp. 100-107.

51   M. Djordjević and B. M. Notaroš, "Three types of higher order MoM basis functions automatically satisfying current continuity conditions," *2002 IEEE*

Antennas and Propagation Society International Symposium Digest, June 16-21, 2002, San Antonio, TX, U.S.A., pp. IV. 610-613.

52   B. M. Notaroš, B. D. Popović, M. Djordjević, and M. M. Ilić, "Hierarchical and interpolatory higher order vector basis functions for finite element method and method of moments," *Sixth International Workshop on Finite Elements for Microwave Engineering, Antennas, Circuits and Devices - Book of Abstracts*, May 30 - June 1, 2002, Chios, Greece, p. 65.

53   E. Jorgensen, J. L. Volakis, P. Meincke, and O. Breinbjerg, "Higher order hierarchical Legendre basis functions for iterative integral equation solvers with curvilinear surface modeling," *2002 IEEE Antennas and Propagation Society International Symposium Digest*, June 16-21, 2002, San Antonio, TX, U.S.A., pp. IV. 618-621.

54   J. P. Webb and V. N. Kanellopoulos, "Absorbing boundary conditions for the finite element solution of the vector wave equation," *Microwave and Optical Technology Letters*, Vol. 2, No. 10, October 1989, pp. 370-372.

55   C. H. Wilcox, "An expansion theorem for electromagnetic fields," *Communications on Pure and Applied Mathematics*, Vol. 9, 1956, pp. 115-132.

56   A. Chatterjee, J. M. Jin, and J. L. Volakis, "A finite element formulation with absorbing boundary conditions for three dimensional scattering," *IEEE Transactions on Antennas and Propagation*, February 1993, Vol. 41, No. 2, pp. 221-226.

57   T. Ozdemir and J. L. Volakis, "A comparative study of an absorbing boundary condition and an artificial absorber for terminating finite element meshes," *Radio Science*, September/October 1994, Vol. 29, No. 5, pp. 1255-1263.

58   J. D'Angelo and I. D. Mayergoyz, "Three dimensional RF scattering by the finite element method," *IEEE Transactions on Magnetics*, Vol. 27, No. 5, September 1991, pp. 3827-3832.

59   A. Chatterjee and J. L. Volakis, "Conformal absorbing boundary conditions for the vector wave equation," *Microwave and Optical Technology Letters*, Vol. 6, 1993, pp. 886-888.

60   A. Chatterjee, J. M. Jin, and J. L. Volakis, "Edge-based finite elements and vector ABCs applied to 3-D Scattering," *IEEE Transactions on Antennas and Propagation*, Vol. 41, No. 2, February 1993, pp. 221-226.

61   J. Gong, J. L. Volakis, A. C. Woo, and H. T. G. Wang, "A hybrid finite element – boundary integral method for the analysis of cavity – backed antennas of arbitrary shape," *IEEE Transactions on Antennas and Propagation*, Vol. 42, No. 9, September 1994, pp. 1233-1242.

62   J. L. Volakis, T. Ozdemir, and J. Gong, "Hybrid finite-element methodologies for antennas and scattering," *IEEE Transactions on Antennas and Propagation*, Vol. 45. No. 3, March 1997, pp. 493-507.

63   X. Q. Sheng, J. M. Jin, J. Song, C. C. Lu, and W. C. Chew, "On the formulation of hybrid finite-element and boundary-integral methods for 3-D scattering," *IEEE Transactions on Antennas and Propagation*, Vol. 46, No. 3, March 1998, pp. 303-311.

64   K. D. Paulsen, D. R. Lynch, and J. W. Strohbehn, "Three-dimensional finite, boundary, and hybrid element solutions of the Maxwell equations for lossy dielectric media," *IEEE Transactions on Microwave Theory and Techniques*, Vol. 36, No. 4, April 1988, pp. 682-693.

65 X. Yuan, "Three-dimensional electromagnetic scattering from inhomogeneous objects by the hybrid moment and finite element method," *IEEE Transactions on Microwave Theory and Techniques*, Vol. 38, No. 8, August 1990, pp. 1053-1058.

66 D. Janković, M. LaBelle, D. C. Chang, J. M. Dunn, and R. C. Booton, "A hybrid method for the solution of scattering from inhomogeneous dielectric cylinders of arbitrary shape," *IEEE Transactions on Antennas and Propagation*, Vol. 42, No. 9, September 1994, pp. 1215-1222.

67 J. C. Cheng, N. I. Dib, and L. P. B. Katehi, "Theoretical modeling of cavity-backed patch antennas using a hybrid technique," *IEEE Transactions on Antennas and Propagation*, Vol. 43, No. 9, September 1995, pp. 1003-1013.

68 D. J. Hoppe, L. V. Epp, and J. F. Lee, "A hybrid symmetric FEM/MOM formulation applied to scattering by inhomogeneous bodies of revolution," *IEEE Transactions on Antennas and Propagation*, Vol. 42, No. 6, June 1994, pp. 798-805.

69 X, Yuan, D. R. Lynch, and J. W. Strohbehn, "Coupling of finite element and moment methods for electromagnetic scattering from inhomogeneous objects," *IEEE Transactions on Antennas and Propagation*, Vol. 38, No. 3, March 1990, pp. 386-393.

70 J. A. Stratton, *Théorie de l'Électromagétisme*, Paris, France: Duond, 1961.

71 R. F. Harrington, *Time Harmonic Electromagnetic Fields*, New York: Mc Graw-Hill, 1961.

72   E. B. Wilson (founded upon the lectures of J. W. Gibbs), *Vector analysis*, New York: Dover Publications Inc., 1960.

73   C. T. Tai, *Generalized vector and dyadic analysis – applied mathematics in field theory*, New York: IEEE Press, 1997.

74   J. D. Jackson, *Classical electrodynamics*, New York: Wiley, January 1999.

75   T. B. A. Senior and J. L. Volakis, *Approximate boundary conditions in electromagnetics*, London, U.K.: The Institution of Electrical Engineers, 1995.

76   H. Whitney, *Geometric integration theory*, Princeton: Princeton University Press, 1957.

VITA

Milan M. Ilić (milanilic@ieee.org) was born in Belgrade, Yugoslavia, in June 1970. He received the Dipl. Ing. and M.S. degrees in Electrical Engineering from the University of Belgrade, Yugoslavia, in 1995 and 2000, respectively. From 1995 to 2000, he was a Research and Teaching Assistant in the School of Electrical Engineering, University of Belgrade, Yugoslavia. From 2000 to 2003, he was in the Ph.D. program at the University of Massachusetts Dartmouth, Massachusetts, USA, and he worked as a Research Assistant. His research interests include computational electromagnetics, antennas, and passive microwave components and circuits.

Selected publications:

1. M. M. Ilić and B. M. Notaroš, "Higher order hierarchical curved hexahedral vector finite elements for electromagnetic modeling," *IEEE Transactions on Microwave Theory and Techniques*, Vol. 51, No. 3, March 2003, pp. 1026-1033.

2. B. M. Notaroš, V. V. Petrović, M. M. Ilić, A. R. Djordjević, B. M. Kolundzija, and M. D. Dragović, *Collection of Examination Questions and Problems in Electromagnetics*, University of Belgrade, Department of Electrical Engineering, Yugoslavia, 1998, ISBN 86-7225-027-3.

3. M. M. Ilić and B. M. Notaroš, "Computation of 3-D electromagnetic cavity resonances using hexahedral finite elements with hierarchical polynomial basis

functions," 2002 *IEEE Antennas and Propagation International Symposium Digest*, June 16-21, 2002, San Antonio, TX, USA, pp. IV. 682-685.

4. M. M. Ilić and B. M. Notaroš, "Entire-domain and large-domain finite element analysis of 3-d electromagnetic cavities," *Sixth International Workshop on Finite Elements for Microwave Engineering Antennas, Circuits and Devices – Book of Abstracts*, May 30 – June 1, Chios, Greece, 2002, p. 30.

5. B. M. Notaroš, B. D. Popović, M. Djordjević, and M. M. Ilić, "Hierarchical and interpolatory higher-order vector basis functions for finite element method and method of moments," *Sixth International Workshop on Finite Elements for Microwave Engineering, Antennas, Circuits and Devices - Book of Abstracts*, May 30 – June 1, 2002, Chios, Greece, p. 65.

6. M. M. Ilić and B. M. Notaroš, "Trilinear hexahedral finite elements with higher-order polynomial field expansions for hybrid SIE/FE large-domain electromagnetic modeling," *2001 IEEE Antennas and Propagation Society International Symposium Digest*, July 8-13, 2001, Boston, MA, USA, vol. III, pp. 192-195.